Titre: Title:	Assessment and Modification of Novel Counter-Rotating Centrifugal Compressor Concept for Transonic Speeds
Auteur: Author:	Mohsen Boroumand
Date:	2022
Type:	Mémoire ou thèse / Dissertation or Thesis
Référence: Citation:	Boroumand, M. (2022). Assessment and Modification of Novel Counter-Rotating Centrifugal Compressor Concept for Transonic Speeds [Ph.D. thesis, Polytechnique Montréal]. PolyPublie. https://publications.polymtl.ca/10461/

POLYTECHNIQUE MONTRÉAL

Affiliée à l'Université de Montréal

Assessment and modification of novel counter-rotating centrifugal compressor concept for transonic speeds

MOHSEN BOROUMAND

Département de génie mécanique

Thèse présentée en vue de l'obtention du diplôme de *Philosophiæ Doctor*

Génie mécanique

Août 2022

POLYTECHNIQUE MONTRÉAL

Affiliée à l'Université de Montréal

Cette thèse intitulée :

Assessment and modification of novel counter-rotating centrifugal compressor concept for transonic speeds

présentée par **Mohsen BOROUMAND**

en vue de l'obtention du diplôme de *Philosophiæ Doctor*

a été dûment acceptée par le jury d'examen constitué de :

Jérôme VETEL, président
Huu Duc VO, membre et directeur de recherche
René KAHAWITA, membre
Jeffrey James DEFOE, membre externe

ACKNOWLEDGEMENTS

First and foremost I am deeply grateful to my supervisor, Professor Huu Duc VO for his invaluable advice, and continuous support throughout my Ph.D. study. His immense knowledge and plentiful experience have constantly encouraged me in my academic research and daily life. It is an honour for me to be his student and take advantage of his knowledge in turbomachinery which will assist me in my career. I would also like to thank the Natural Sciences and Engineering Research Council of Canada (NSERC) Discovery Grant program for funding this research.

Finally, I also would like to express my gratitude to my wife and my children. Without their tremendous understanding and encouragement over the past few years, it would have been impossible for me to complete my study in a new country.

RÉSUMÉ

Cette étude présente la première évaluation aérodynamique réaliste et modification à un nouveau concept de compresseur centrifuge contra-rotatif pour application dans les moteurs d'avion. Ce concept consiste à remplacer le diffuseur dans un compresseur centrifuge aéronautique par un court diffuseur sans aubes et un rotor axial tournant à contre-sens pour doubler l'augmentation de pression totale déjà élevée de l'impulseur. Cet étage de compresseur compact avec un rapport de pression par étage sans précédent permettrait de réduire la consommation de carburant des moteurs d'avion et/ou leur taille, poids et complexité mécanique. Cependant, ce concept n'a été évalué qu'à des vitesses très inférieures à celles dans les moteurs d'avion. Cette recherche a pour objectif d'identifier les problèmes aérodynamiques qui empêcheraient ce concept d'atteindre son plein potentiel en terme de performance et d'évaluer des stratégies de conception pour les résoudre.

Une approche numérique utilisant des simulations numériques de l'écoulement (CFD) de type RANS a été choisie pour permettre une évaluation rapide des changements de design et une analyse détaillée du champ d'écoulement. La méthodologie commence avec la conception d'un compresseur centrifuge conventionnel (CC) de moteurs d'avion pour définir les cibles de design pour le compresseur centrifuge contra-rotatif (CRC) qui doit en doubler l'augmentation de pression totale tout en maintenant (ou améliorant) le rendement polytropique et la stabilité aérodynamique. Le compresseur CRC doit avoir le même impulseur et débit de design et posséder un rotor axial contra-rotatif tournant à la même vitesse que l'impulseur (rapport de vitesses à 100%) avec un écoulement sortant axial. Un premier compresseur CRC est conçu et évalué afin d'identifier les causes de déficit de performance. Des stratégies de conception aérodynamique différentes sont alors évaluées pour produire un design révisé du compresseur CRC. Ce compresseur est alors analysé au point de design et hors-design pour en déterminer la performance et la stabilité aérodynamique (marge contre le décrochage) et les causes de tout déficit restant de performance et de déclenchement du décrochage tournant. De nouvelles stratégies sont alors proposées pour atteindre les cibles.

Les résultats indiquent que le concept de compresseur CRC aux vitesses transsoniques peut probablement atteindre les cibles d'augmentation de pression totale et de rendement si deux contraintes initiales de design peuvent être levées, soient le rapport de vitesses à 100% et

l'écoulement de sortie axial afin de réduire les pertes aérodynamiques excessives dans le rotor axial contra-rotatif. En premier lieu, l'écoulement relatif d'entrée hautement supersonique au rotor axial entraîne des pertes de chocs et des pertes visqueuses dues au décollement de couche limite induit par les chocs. Les remèdes de première ligne les plus efficaces sont la combinaison de réduction de vitesse du rotor axial et le remplacement du diffuseur sans aubes par un diffuseur avec aubes pour diminuer le nombre de Mach relatif de l'écoulement d'entrée en régime bas supersonique, et l'utilisation d'un profil d'aube supersonique optimisé pour réduire la force des chocs via une diffusion de l'écoulement par multiples chocs. Cependant, l'impact hautement négatif des deux premières stratégies sur l'augmentation de pression totale à travers le rotor axial doit être compensé par un écoulement de sortie non-axial pour que ce rotor puisse égaler l'augmentation de pression totale de l'impulseur. Une fois les pertes de chocs et visqueuses réglées, le jeu d'aube du rotor axial doit être diminué à bien en deçà de 1% de la hauteur des aubes pour pouvoir combler le déficit de rendement polytropique. Des améliorations additionnelles incluent l'optimisation des aubes du diffuseur à aubes et du rotor axial afin d'éliminer tout décollement de couche limite, ainsi que le remplacement de l'impulseur par un rotor à écoulement mixte de conception agressive.

Finalement, les résultats hors-design indiquent que les compresseur CRC devraient avoir une meilleure stabilité aérodynamique que les compresseurs CC équivalents, même avec un jeu d'aube relativement grand pour le rotor axial. De plus, le rotor axial contra-rotatif est la source probable de l'initiation du décrochage via une déstabilisation de l'écoulement de jeu.

ABSTRACT

This study presents the first realistic aerodynamic assessment and modification of a novel counter-rotating centrifugal compressor concept for application in aircraft engines. This concept consists of replacing the diffuser in an aero-engine centrifugal compressor with a short vaneless diffuser and a counter-rotating axial rotor to double the already high total pressure rise of the impeller. The resulting compact compressor stage with unprecedented stage pressure ratio can reduce the fuel consumption of aero-engines and/or their length, weight and mechanical complexity. However, this concept had only been evaluated at speeds that are far below that required for real gas turbine engine applications. This research aims to identify the aerodynamic issues that can prevent the concept from achieving its full performance potential at (realistic) transonic speeds and assess design strategies to address them.

A computational approach using CFD simulations is chosen for rapid assessment of design changes and detailed analysis of the flow field. The methodology starts with the design of a representative conventional aero-engine centrifugal (CC) compressor to set the design targets for the counter-rotating (CRC) compressor, which has to double the total pressure rise while having similar (or better) polytropic efficiency and stall margin. The CRC compressor should feature the same impeller and design mass flow with a counter-rotating axial rotor rotating at the same speed as the impeller (100% speed ratio) and producing axial exit flow. A first CRC compressor is designed and assessed to identify the cause of performance shortfalls. Different aerodynamic design strategies are then evaluated to produce a revised design that is analyzed both at design and off-design for performance and aerodynamic stability (stall margin) and for elucidation of the causes of remaining performance shortfalls and of rotating stall inception. New strategies are then proposed to close any performance gaps.

The results indicate that the CRC compressor concept at transonic speeds can likely achieve the total pressure rise and efficiency targets if two original design constraints can be lifted, namely 100% speed ratio and axial outflow, to address excessive aerodynamic losses in the counter-rotating axial rotor. First, the highly supersonic inlet relative flow to the axial rotor leads to shock losses and viscous losses from shock-induced boundary layer separation. The most effective first-line remedies are a combination of axial rotor speed reduction and replacement of the vaneless diffuser by a vaned diffuser to reduce the inlet relative Mach number to low supersonic values,

and an optimized supersonic blade profile to reduce shock strength by flow diffusion through multiple passage shocks. However, the highly negative impact of the first two strategies on total pressure rise across the axial rotor must be compensated by non-axial exit flow for it to match the total pressure rise of the impeller. Once shock and viscous losses are addressed, tip clearance must be reduced to well below 1% of blade span to close the remaining gap in polytropic efficiency. Further improvement strategies include optimizing the blade shape for the vaned diffuser and axial rotor to remove all flow separation, as well as replacing the impeller by an aggressive mixed flow rotor.

Finally, off-design results indicate that high-speed CRC compressors should have better stall margin than equivalent CC compressors even with relatively large axial rotor tip clearance. Moreover, the counter-rotating axial rotor is likely the source of stall inception through tip clearance flow breakdown.

TABLE OF CONTENTS

LIST OF TABLES

LIST OF FIGURES

LIST OF SYMBOLS AND ABBREVIATIONS

Symbols and Variables

c_p	Specific heat at constant pressure
$\dot{m}_c$	Corrected mass flow
P	Pressure
P_{ref}	Reference pressure
PR	Pressure ratio
r	Radius
SM	Stall margin
T	Temperature
U	Rotational speed
C	Velocity in stationary frame
w	Work per unit mass flow
W	velocity in relative frame
y^+	Non-Dimensional first mesh layer height
α	Flow angle in stationary frame
β	Flow angle in relative frame
γ	Specific heat ratio
η	Stage efficiency
ω	Rotational speed

Subscripts

o	Stagnation (total)
x	Axial direction
m	Meridional direction

r	Radial direction
θ	Circumferential direction
poly	Polytropic
rel	Relative frame
ref	Reference
s	Isentropic
tip	Blade tip
tt	Total-to-total

Abbreviations

CC	Conventional compressor
CFD	Computational fluid dynamics
CRC	Counter-rotating compressor
DCA	Double circular arc
GGI	General grid interface
IGV	Inlet guide vane
IMP	Impeller
LE	Leading edge
OGV	Outlet guide vane
PS	Pressure side
RANS	Reynolds-Averaged Navier-Stokes
R2	Second (downstream) rotor
SS	Suction side
SST	Shear stress transport
TE	Trailing edge

LIST OF APPENDICES

CHAPTER 1 INTRODUCTION

1.1 Background

It is well known from basic thermodynamic analysis of an ideal Brayton cycle that the efficiency of a gas turbine engine improves with pressure ratio. The pressure ratio of aircraft gas turbine engines has been increasing over the past few decades to about 45:1, as is the case for the GP7000 turbofan engines [1]. A typical high-speed axial compressor stage consists of a rotor and stator with a pressure ratio of only about 1.5. As a result, given the number of axial stages needed to attain the required pressure ratio, the compressor is by far the longest component in a gas turbine engine, thus adding to engine length, weight and mechanical complexity (parts count). Two technologies currently exist to resolve this issue by increasing the stage pressure ratio.

The first is the centrifugal compressor in which the rotor is replaced by an impeller and the stator by a diffuser. The larger exit radius of the impeller versus its inlet radius results in much higher work done on the air than an axial rotor, such that the pressure ratio per stage can reach 10. However, centrifugal compressors suffer from lower isentropic efficiency (by about 5% compared to an axial stage [2]) due to high flow turning in the diffuser (high aerodynamic losses) and higher stress due to the larger impeller exit radius. As a result, they are mainly used in small gas turbine engines for private jets and smaller regional aircrafts where there can be a trade-off between simplicity and efficiency. Even then, a centrifugal compressor stage is often preceded by a few axial stages to have enough pressure ratio while keeping overall efficiency reasonable. However, the increasing bypass ratio of large turbofan engines to augment propulsive efficiency are reducing their core. As such, centrifugal compressors can eventually be used if their isentropic efficiency improves.

The other existing technology for increased stage pressure ratio is counter-rotation, in which the stator of an axial compressor stage is replaced by a rotor turning in the opposite direction. Unlike a stator, the counter-rotating rotor also does work and can double the work and, in principle, the pressure rise of the stage. While this idea has been explored in several studies over the past decades, it has yet to be implemented in a commercial engine. The main reason is that multiple counter-rotating stages would still be required to achieve the required pressure ratio, leading to the need for both a rotating hub and a rotating shroud, making the mechanical design impractical.

To resolve the drawbacks associated with the above technologies, a novel concept of counter-rotating centrifugal (CRC) compressor had been proposed at Polytechnique Montréal in 2015 and since patented [3]. As illustrated in Figure 1-1, the concept consists of replacing the diffuser in a centrifugal compressor stage by a counter-rotating rotor. It can be shown analytically that if this rotor rotates at the same speed as the impeller and ejects the flow at the same angular momentum as the flow at the impeller inlet, it would do the same amount of work as the impeller. Thus, in an ideal setting, the CRC compressor would double the already high total pressure rise of the impeller. The resulting stage would have such a high total pressure ratio that only a single counter-rotating stage would be required, making its mechanical implementation more feasible. Indeed, as shown in Figure 1-1, the counter-rotating rotor can be driven either by the main shaft through gears or by a separate turbine rotor through an additional spool.

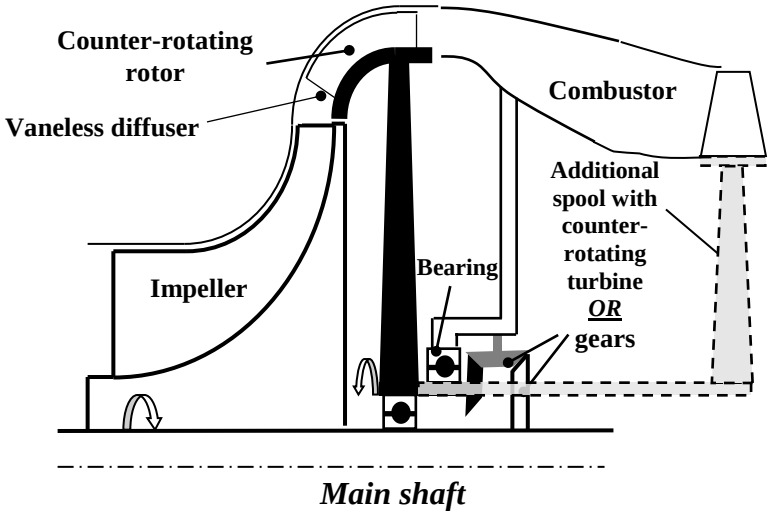

Figure 1-1 Counter-rotating centrifugal (CRC) compressor concept (adapted from reference [4])

The other advantage of the CRC concept is that the required flow turning by the counter-rotating rotor to bring the high-swirl flow exiting the impeller into the axial direction would be significantly smaller than that by a diffuser due to the effect of counter-rotation as shown in Figure 1-2. As a result, there is a potential for reduced aerodynamic losses and instabilities due to boundary layer growth and separation currently associated with a diffuser. This could result in improved compressor efficiency and stall margin (difference in mass flow between design point and point of aerodynamic instability, normalized by the design point mass flow) relative to a conventional centrifugal stage design.

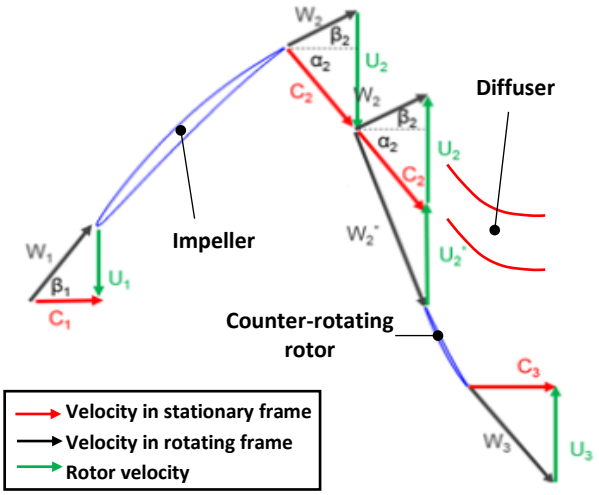

Figure 1-2 Velocity triangles for the CRC versus CC compressors [4]

A first assessment of the CRC compressor concept has recently been carried out at Polytechnique Montréal [5] in which a conventional centrifugal compressor (CC) with low subsonic impeller tip speed and *fishtail* type pipe diffusers and an equivalent CRC compressor with the same impeller, (shown in Figure 1-3) were both designed and simulated using RANS CFD. The results showed that the CRC compressor could potentially deliver twice the pressure rise of the equivalent conventional compressor while being more compact axially and radially. However, the impeller/rotor tip speed (low subsonic) and pressure rise involved are much lower than those of aero-engine compressors whose impeller tip circumferential speeds are transonic.

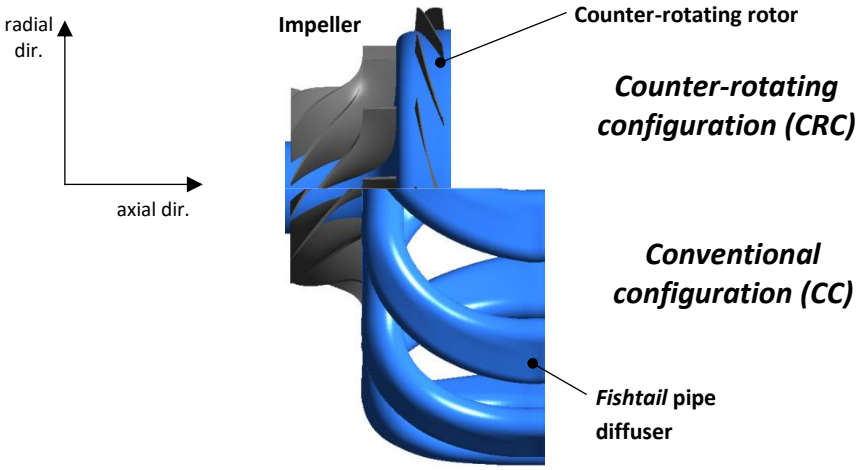

Figure 1-3 Low-speed counter-rotating versus conventional centrifugal compressors (same impeller) [5]

If the CRC compressor concept can be shown to work at high speed (transonic impeller/rotor tip circumferential speed), and given that a conventional centrifugal stage can have a pressure ratio

of up to 10, a single CRC compressor stage with double the pressure rise of its CC equivalent could deliver a pressure ratio of up to 19. This would have two immediate impacts on aero-engine designs. For a small private jet turbofan engine with just a couple of compressor stages, such as the JT15D engine illustrated in Figure 1-4, the replacement of the diffuser with a counter-rotating rotor (red) would markedly increase total pressure ratio and result in a significant reduction in specific fuel consumption (SFC) (estimated at about 14% on the JT15D engine using a thermodynamic model of this engine [6]). For a larger turbofan engine with many compression stages and higher pressure ratio, such as the PW300-class turbofan engine shown in Figure 1-5, the CRC compressor concept would allow the elimination of many (in this case all of the) axial stages, resulting in a simpler, and much shorter engine with reduced diameter and weight.

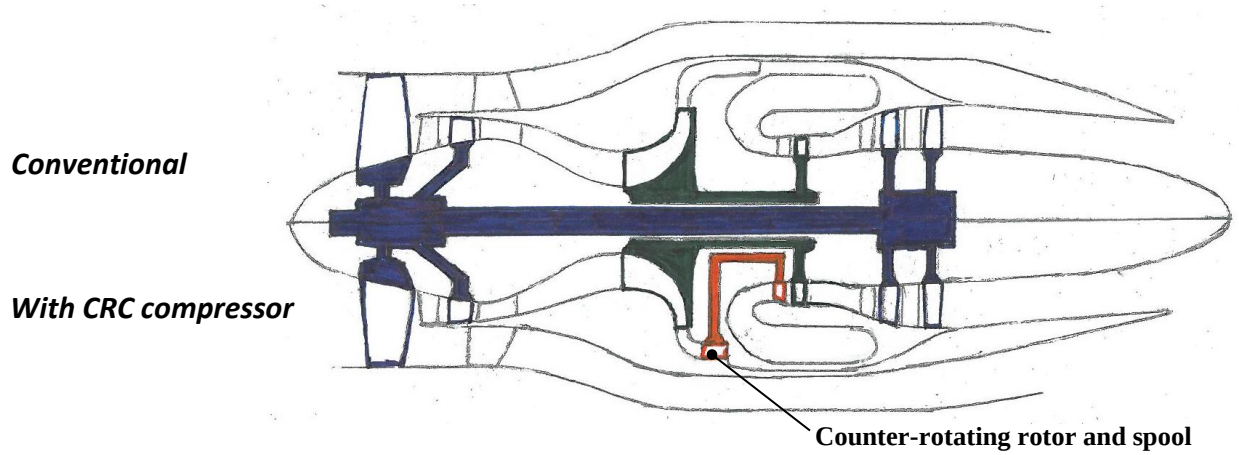

Figure 1-4 Large increase in PR of low-PR engines (e.g. JT15D) for large SFC reduction

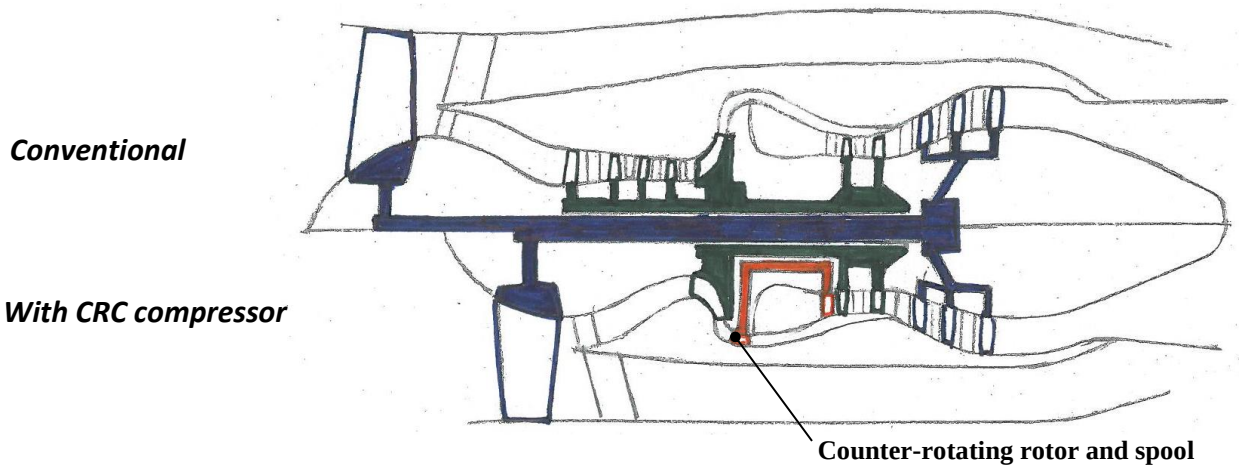

Figure 1-5 Removal of axial compressor stages of higher-PR engines (e.g. PW300 class) for significant size/weight/complexity reduction

1.2 Problematic

The transition from low-speed to high-speed (transonic blade tip speed) compressors like those found in aero-engines is expected to involve a few challenges. While the low-speed validation work on the CRC compressor concept gave promising results, it also showed two potential issues with the new concept that will likely pose challenges at high speed.

First, the span of the blades on the downstream rotor is small due to the difference in radius between the inlet of the impeller inlet and that of the counter-rotating rotor. As such, the size of the tip clearance relative to the blade span for the latter is large, and so is its associated negative effect on performance (lower pressure ratio and efficiency) and stall margin (aerodynamic instability occurring at a higher mass flow) compared to regular axial rotors. This problem can only be exacerbated at high speed since the higher-pressure ratio across the impeller (giving higher density rise) would result in much shorter blades for the downstream rotor.

Second, as shown in Figure 1-2, counter-rotation incurs high inlet relative velocity to the downstream rotor. For a high-speed compressor with transonic rotor tip speed, the flow entering to the counter-rotating rotor is supersonic, resulting in the formation of shocks. If the inlet relative Mach number is high, these shocks can incur very high aerodynamic losses. Moreover, they can interact with the blade boundary layer and cause flow separation even if the downstream rotor has a very low camber (low flow turning). The shocks and boundary layer separation can significantly degrade the efficiency and stall margin of the stage.

The above are examples of serious potential aerodynamic issues that can make the performance and operating envelope of CRC compressor concept unacceptably low at high speed. Hence, such issues must be assessed and addressed for the CRC compressor concept to be applied to aircraft engines.

1.3 Objectives

Based on the potential challenges discussed in section 1.2, the objectives of this project are:

1) Identify aerodynamic issues that can prevent the CRC compressor concept from achieving its desired performance at (realistic) transonic speeds associated with aero-engine

applications, namely double the pressure rise of an equivalent CC compressor with similar or better polytropic efficiency and stall margin

2) Propose and assess strategies to address these issues

1.4 Contributions

This work has two main contributions. First, it provides the first assessment of the counter-rotating centrifugal compressor concept at realistic aero-engine operating conditions. Second, it proposes design modifications to allow the concept to attain the desired performance for aero-engine applications.

1.5 Thesis Organization

This thesis is organized into seven chapters. Following this introduction, Chapter 2 provides a literature review on losses and rotating stall in axial compressor rotors, supersonic axial rotor blade design and counter-rotating fans and compressors. Chapter 3 describes the methodology used to achieve the proposed objectives. Chapter 4 presents a detailed analysis of a first CRC compressor design at design mass flow and identify the sources of design-point performance deficiency. Chapter 5 evaluates design strategies to improve the performance of the CRC compressor design. Chapter 6 evaluates an improved CRC compressor design both at the design point for performance analysis and at off-design for stall margin and cause of stall, as well as proposing other strategies for further design improvements. Finally, Chapter 7 summarizes the main conclusions and proposes future work.

CHAPTER 2 LITERATURE REVIEW

This chapter starts with a literature review on the sources of loss and rotating stall in axial compressor rotors, as well as on supersonic axial compressor rotors, that can be useful for assessment and design improvement of the downstream rotor in a CRC compressor. Subsequently, it provides an overview of previous studies on counter-rotating fans and compressors for a clearer assessment of what has been accomplished in this field.

2.1 Losses in Axial Compressor Rotors

Losses in compressors relate to relative total pressure loss that leads to reduced pressure rise/ratio and efficiency. The losses in an axial compressor can be divided into profile loss, secondary loss, tip leakage loss and shock loss [7].

Profile loss is the loss generated by the boundary layers on the blade surfaces away from the end walls (hub and shroud). It is assumed that flow related to profile loss is two dimensional so that 2-D boundary layer calculations are often used to estimate profile losses.

Secondary loss is associated with the boundary layers passing through a blade passage end walls (without tip clearance). Due to a lower centrifugal force from the lower streamwise velocity of the endwall boundary layer fluid, the latter flows toward the blade suction side and can cause a corner flow separation in the blade passage [8]. This phenomenon reduces compressor performance through increased viscous losses.

Tip leakage loss is associated with the flow through the small gap between the rotor blade tip and the shroud (or the gap between stator tip and the hub for cantilevered stators), often referred to as *tip clearance flow* or *tip leakage flow*. Storer and Cumpsty [9] (1994) showed that the component of the tip clearance flow normal to the blade is driven by the pressure difference between the suction and pressure side of the blade while the streamwise component (parallel to the blade camber) is essentially that of the mainstream flow. These authors also indicated two mechanisms for tip leakage losses. The first is the mixing between the mainstream flow and the tip clearance flow due to difference in their speeds and directions. The second loss mechanism is the reduction in effective flow area in the mainstream direction, called *tip blockage*, due to the velocity deficit in the mainstream direction associated with the shear layer and the tip clearance flow region. This

blockage causes an increase of the relative streamwise velocity component in the mainstream region, altering the velocity triangles to give lower flow turning by the rotor in the stationary frame and thus lower pressure rise. In the tip region, the lower streamwise velocity in the rotor frame leads to high flow incidence and thus more losses for the downstream stator. It is noted that tip clearance flow can interact with the endwall boundary layer and thus affect secondary losses as well.

A decrease in mass flow raises the above first three types of loss. The accompanying decrease in the axial velocity component translates to higher flow incidence and thus, higher flow turning in the blade passage. The resulting higher static pressure gradient in the streamwise direction increases blade and endwall boundary layer thickness leading to higher profile and secondary losses. The larger pressure difference between the pressure and suction side leads to a higher tip clearance flow velocity component perpendicular to the blade camber (and thus mainstream flow), resulting in higher shear and mixing losses and tip blockage between tip clearance flow and mainstream (core) flow. Last but not least, the relative magnitudes of the above three types of loss are also dependent on the blade aspect ratio, and tip clearance size (relative to span and chord).

The last type of loss is shock loss which occurs at supersonic relative velocity, increasing rapidly with rising Mach number. Most publicly available correlations for shock losses go up to a relative inlet Mach number of about 1.6 [7].

2.2 Rotating Stall in Axial Compressor Rotors

Rotating stall is an aerodynamic instability characterized by a cell of velocity deficit (rotating stall cell) that rotates at a fraction of the rotor speed. It is usually accompanied by a drop in the pressure rise and triggers a more devastating aerodynamic instability called *surge* where the mass flow oscillates across the engine causing sudden and catastrophic power reduction and potential component failure. Camp et al. [10] (1997) showed that there are two well-established routes to rotating stall, which are distinguished by the type of initial perturbation in pressure/velocity. The first route, referred to as *modal stall inception*, is characterized by the relatively slow growth (20-40 rotor revolutions) of a long length-scale perturbation (on the order of the annulus circumference) into a fully developed rotating stall cell. This is shown to occur when the slope of

the total-to-static pressure rise coefficient versus mass flow characteristic (*speedline*) of the entire compression system goes from negative to positive. It had been shown theoretically by Moore and Greitzer [11] (1986) that a positive slope of this speedline corresponds to negative damping of naturally-occurring perturbations, which then grow into rotating stall cells. As such, the criterion for modal stall inception is the slope of the total-to-static speedline becoming zero, which occurs as the result of losses increasing as mass flow decreases.

The second route to rotating stall, known as *spike stall inception*, is characterized by a short length-scale perturbation (2-3 blade pitches in circumferential wavelength) near the tip of the rotor, which grows very rapidly (2-5 rotor revolutions) to a fully developed rotating stall. Furthermore, it occurs at a negative slope of the total-to-static speedline (i.e., prior to modal stall inception). Day [12] (1993) inferred from experimental results on an axial compressor stage that there is a critical rotor tip incidence associated with spike stall inception, suggesting that its occurrence is related to boundary layer separation occurring at the tip blade profile. They also showed that increasing tip clearance or reducing rotor tip incidence can cause the transformation of spike to modal stall inception. However, the value of critical tip incidence could vary with blade geometry, negating the generic nature of this criterion.

Based on a computational study of a modern low-speed axial compressor rotor, Vo et al. [13] (2008) proposed two quantitative criteria for predicting spike stall inception in axial compressors. As illustrated in Figure 2-1a, the first criterion is the onset of tip clearance flow spillage at the leading edge into the adjacent blade passage. This phenomenon occurs when the interface between the incoming and tip clearance flow reaches the leading edge on the rotor pressure side at the blade tip span. Separating the lower entropy incoming flow from the higher entropy tip clearance flow, the interface can be detected as a line of high entropy gradient in the entropy contours, as shown in Figure 2-1b. With its position resulting from a balance between the momentums of incoming and tip clearance flows, this interface moves upstream toward the rotor leading edge with decreasing mass flow since the incoming flow momentum decreases while that of the tip leakage flow increases. The second proposed spike stall inception criterion by Vo et al. [13] (2008) is the onset of the axially reversed flow of tip clearance fluid at the trailing edge below the blade tip, causing it to impinge on the adjacent blade's pressure surface and moving upstream due to the pressure gradient, as illustrated in Figure 2-1c. This criterion occurs when the spanwise distribution of mass flow at the trailing edge plane reaches zero at the blade tip, as

illustrated in Figure 2.2d. The leading edge spillage criterion has been widely verified in axial compressors, both computationally and experimentally, for subsonic regime such as by Deppe et al. [14] (2005) as well as for transonic conditions such as in the works of Hah et al. [15] (2006) and Bennington et al. [16] (2007). While some of these works indicate the presence of flow impingement on the adjacent blade's pressure surface, none has quantitatively validated the second criterion by showing zero mass flow at the blade trailing edge tip span.

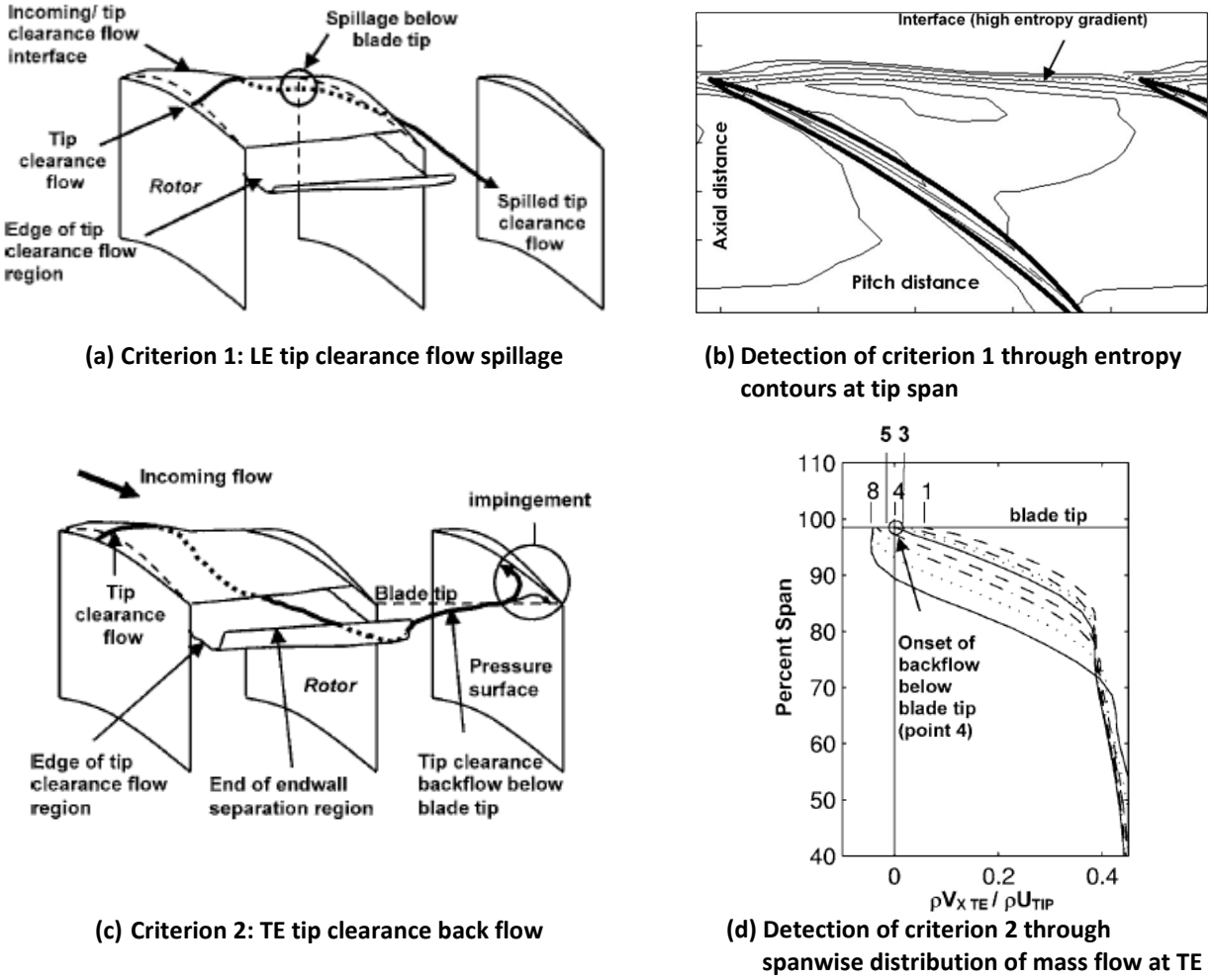

(a) Criterion 1: LE tip clearance flow spillage

(b) Detection of criterion 1 through entropy contours at tip span

(c) Criterion 2: TE tip clearance back flow

(d) Detection of criterion 2 through spanwise distribution of mass flow at TE

Figure 2-1 Criteria for the formation of spike rotating stall disturbances [13]

2.3 Supersonic Axial Compressor Rotors

The first attempts at designing supersonic axial compressors occurred in 1950 when Kantrowitz [17] (1950) investigated the possibility of supersonic axial flow compressors. He showed that the shock pattern, which is usually responsible for losses in this compressor, could be improved by

using the correct blade profiles for the rotor and stator. The author also tested a single-stage supersonic compressor with a pressure ratio of about 1.8 and an efficiency of around 80%.

York et al. [18] (1976) studied the flow conditions at the inlet of a supersonic axial compressor. They showed that when the axial component of the inlet flow is subsonic, a pattern of shock and Mach waves forms at the leading edge of the blade. They propagate inside the blade passage to eventually bring the flow to a subsonic condition.

Gustafson [19] (1976) used experimental data for developing a model for the supersonic flow in a compressor cascade. He simplified the governing equation in supersonic flow and solved them to calculate the cascade performance parameters, such as pressure ratio, and loss coefficient as functions of the inlet Mach number. The result showed good agreement between test data and predictions.

Broichhausen et al. [20] (1982) theoretically and experimentally studied different supersonic rotors including impulse type and shock type rotors. They investigated the structure of the front and passage shock and found that the shocks caused strong pressure loss in the rotors. The impulse type rotor used in this work had a thin and long leading edge and the shock pattern includes only one shock inside the passage.

Freeman and Cumpsty [21] (1989) developed a simple model for supersonic axial compressors with un-camberd blades. Their model was able to predict the losses in the inlet region of the blades and the result agreed well with experimental data. They showed that the loss in supersonic compressors is mainly a function of blade rotational speed and incidence. Figure 2-2 illustrates the supersonic profile and the shock pattern from their study. The supersonic profile has maximum thickness t and stagger angle χ with an inlet flow Mach number M_1 and relative flow angle β_1. A shock occurs at the leading edge and reaches the adjacent blade's suction surface. Finally, another shock or maybe several shocks form inside the passage (not drawn by the authors) and brings the flow to subsonic.

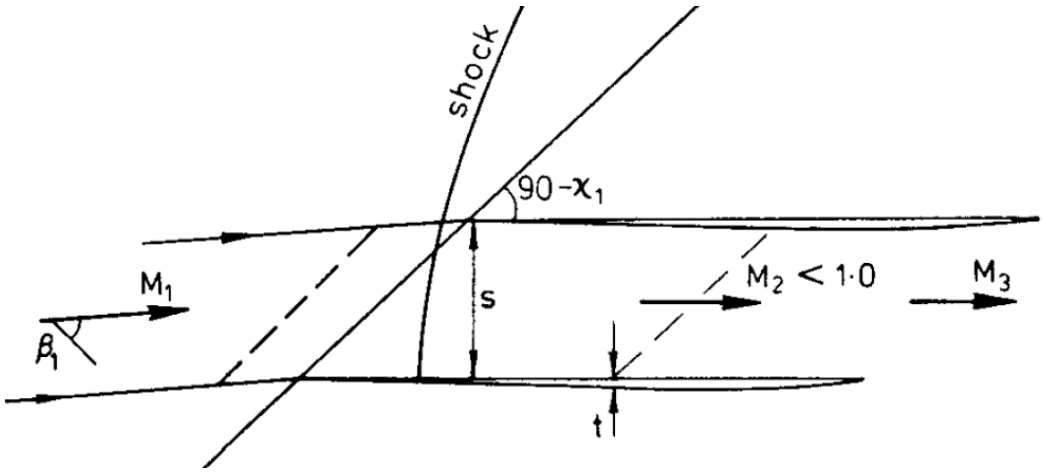

Figure 2-2 Supersonic un-cambered blade profile and shock pattern from Freeman and Cumpsty [21]

Schreiber and Starken [22] (1992) used a cascade to experimentally study the loss mechanism associated with shocks and shock/boundary layer interaction in a supersonic compressor blade passage. Their studied configuration and shock pattern are shown in Figure 2-3. The inlet relative Mach number was 1.5 and the flow turning is only three degrees. The first passage shock (which has a normal section) interacts with the boundary layer and forms a lambda shock. This interaction causes a strong boundary layer separation. The flow downstream of the first oblique shock accelerates from Mach 1.05 to 1.30, and is decelerated to subsonic by a second passage shock.

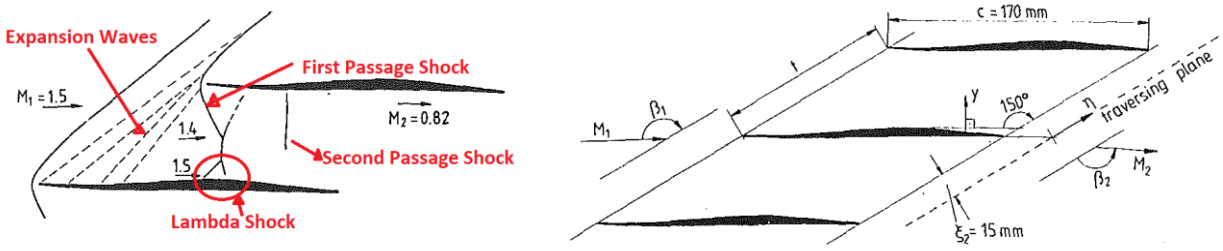

Figure 2-3 Shock wave pattern (left) and cascade geometry (right) of Schreiber and Starken (adapted from reference [22])

Suder [23] (1996) studied the flow field in the NASA Rotor 37 to understand loss and blockage development in supersonic axial compressors. The author found that blockage associated with the endwalls is almost three times that of the blade boundary layers on the core span (defined from 20% to 80% span). When the shock is weak enough to avoid flow separation, the loss in the

compressor is mainly from the shock loss. When the shock strength increases and causes flow separation, the profile loss increases and exceeds the shock loss while the blockage is doubled.

Bloch et al. [24] (1999) developed a shock loss model for the off-design operation of a supersonic compressor cascade when both inlet Mach number and incidence vary. Their result showed that with increased incidence angle, the total loss will increase which is due to the increase in the shock loss. They also showed that the viscous profile loss is almost constant over the operating range of the compressor. However, when the shock interacts with the boundary layer and separation occurs, the viscous loss rapidly increases. They also showed that the shock loss is very sensitive to inlet relative Mach number.

Burguburu et al. [25] (2004) carried out an optimization process for the design of rotor blade profiles for a transonic axial compressor. Their shape parametrization method is illustrated on the left side of Figure 2-4. The camber line and suction side of a reference profile were modified using a Bezier curve of fifth degree. The optimization improved the blade isentropic efficiency by 1.75 percent. The change in the rotor Mach number contours for their rotor design is shown on the right side of Figure 2-4.

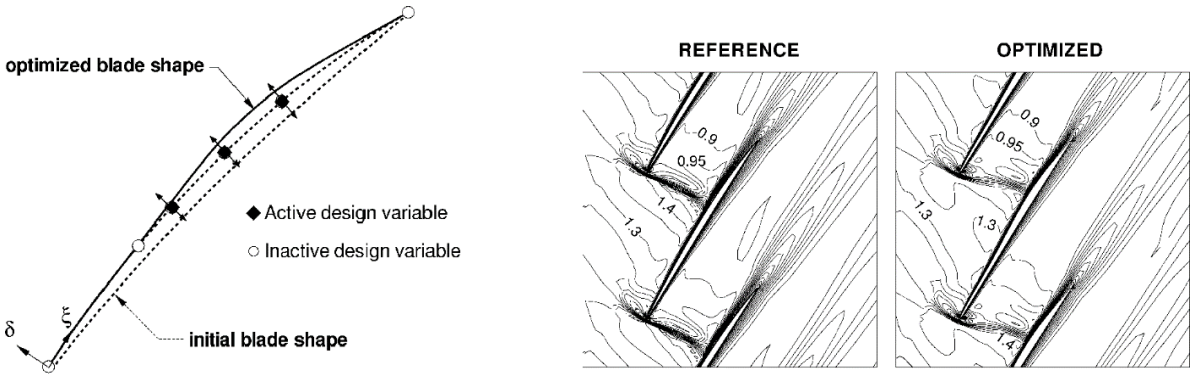

Figure 2-4 Supersonic blade profile optimization parametrization (left) and inlet Mach number contours (right) from Burguburu et al. [25]

Sonoda et al. [26] (2009) used numerical shape optimization algorithms to improve the performance of the DLR-PAV-1.5 supersonic airfoil. The authors used third-order rational B-spline curves for building the new profile as illustrated on the left side of Figure 2-5. They studied the shock and boundary layer interaction to evaluate the loss in supersonic axial compressors. Their optimization reduced the total pressure loss coefficient by 24 percent by

weakening the passage shock. This reduction was due to the weaker passage shock loss. The pattern of the shocks for the optimized design is shown on the right side of Figure 2-5.

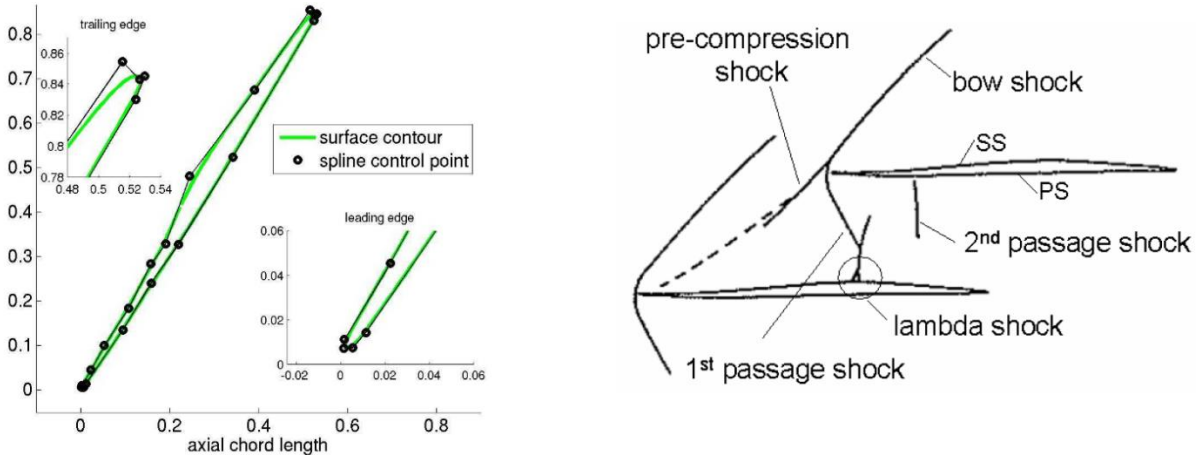

Figure 2-5 Supersonic blade profile parametrization (left) and pattern of the shocks (right) from Sonoda et al. [26]

Lie et al. [27] (2017) tried to reduce the strength of the first and second passage shock to decrease the shock loss in a supersonic axial compressor. They divided the shock pattern in a supersonic axial compressor rotor into four elements as shown in Figure 2-6. The first element is an expansion in the leading edge region of the profile. The second element is the first passage shock which most of the time is an oblique shock. The third element is the interaction of the first passage shock with the boundary layer and the formation of the lambda-type shock. Finally, the last element is the second passage shock around the trailing edge of the profile. They used their model to predict shock losses inside the passage to achieve lower loss with the same static pressure ratio. They found that there is an optimal angle for the first passage shock which, working at this or smaller incidence, leads to the best total pressure recovery coefficient. They redesigned the ARL-SL19 and DLR-PAV-1.5 supersonic cascades and modified their geometries to improve the shock loss by about 29% and 25%, respectively.

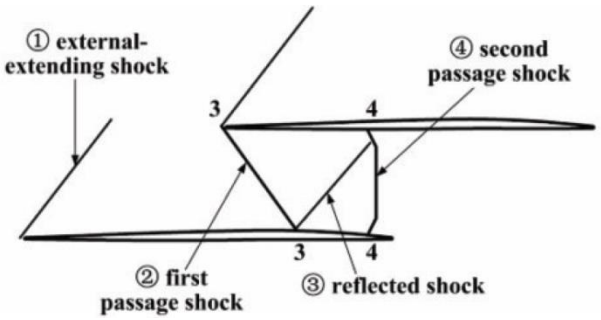

Figure 2-6 Modeled shock pattern in a supersonic axial compressor rotor by Lie et al.[27]

2.4 Counter-Rotating Axial Compressors and Fans

The concept of using counter-rotation to increase the stage pressure ratio has been known for decades but has been limited to axial compressors and fans. As reported by Wennerstrom [28] (1990), the earliest counter-rotating axial compressor was built and tested in the mid-1950s by Curtiss–Wright and illustrated in Figure 2-7. This transonic stage design produced a total pressure ratio of 3.24 with an isentropic efficiency of 73.3%.

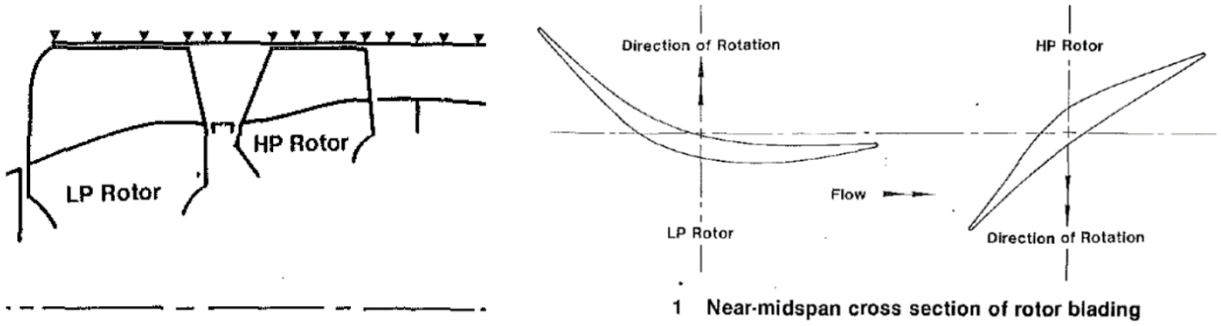

Figure 2-7 Transonic counter-rotating axial compressor stage by Curtiss–Wright [28]

In the 1980s and early 1990s, IIT Delhi carried out more extensive testing on a low-speed axial counter-rotating compressor rig with each rotor having a hub-to-tip ratio of 0.667 and rotational speed up to 2,500 rpm, as reported in references [29] through [31]. The authors found that the speed ratio (rotational speed of downstream rotor to that of the upstream rotor) and the axial gap between the two rotors have a considerable effect on the performance and stall behavior of the stage. For a small axial gap, an increase in speed ratio both improves pressure ratio and delays the stall point of the upstream rotor to a lower mass flow (although it does not affect the stall point of the stage, implying that the downstream rotor is causing rotating stall). On the other hand, for a larger axial gap, an increase in speed ratio also has a (lower) positive impact on the stall point of the upstream rotor but causes the stage to stall earlier.

More recently, Chen et al. [32] (2008) experimentally and numerically studied the performance of a subsonic contra-rotating axial flow compressor at design and off-design conditions for different values of speed ratio. The total pressure ratio, mass flow and rotational speed of the contra-rotating axial compressor were 1.22, 6.4 kg/s and 8000 rpm respectively. The two rotors of the stage are sandwiched between an inlet guide vane and outlet guide vane, both of which are

basically stators. The authors studied different speed ratios and found that the stall margin of the compressor in the contra-rotating arrangement is smaller than the equivalent conventional compressor. They also showed that the speed ratio between the two rotors significantly affects the off-design performance of the stage. By increasing the speed ratio, they reached a higher isentropic efficiency of 87.41% with a small penalty in total pressure ratio and stall margin.

In a later work, Wang et al. [33] (2012) carried out a more detailed investigation into rotating stall on a low-speed counter-rotating axial compressor rig. Static and dynamic pressure measurements with high-response pressure sensors placed at different locations indicated that stall inception starts in the blade tip region of the downstream rotor. They also found that the stall cell is rotating at 35% of the rotor speed.

Recently, Mao and Liu [34] (2016) studied the unsteady flow field in a counter-rotating axial compressor with a total pressure ratio of 1.2. They analyzed the effect of the tip leakage flow and rotating stall on the performance of the stage. They found that the oscillation on the pressure side of the rotor blades is stronger than on the suction side, especially in the region near the tip. Using contours of entropy variation to track the tip leakage vortices in the rotors, they showed that the intensity of vortices in the second rotor is stronger and flow fluctuations at the leading edge of the second rotor causes the stall inception of the counter-rotating axial compressor.

During the past three decades, the concept of counter-rotation has also been studied for fans, which are somewhat like an axial compressor stage except for the lower hub-to-tip ratio with consequently more variation in geometry and flow properties along the span. In the 1990s, Wallscheid et al. [35] (1998) carried out a study on a transonic counter-rotating Propfan at MTU with a speed ratio and total pressure ratio of 0.867 and 1.242 respectively. They investigated experimentally and numerically the aerodynamic impact of the rotors on each other. Their main finding was that the interaction took two forms. First, there is a wake interaction between the rotors in which the wakes from rotor 1 appears to rotor 2 in the latter’s frame of reference as a time-limited flow with positive incidence and with only a moderate velocity defect. Second, the shock waves generated in rotor 2 reflects on the pressure side of rotor 1, along with the interaction of the reflected wave with rotor 2. These interactions affect the flow turning inside the stage and resulted in a flow unsteadiness and total pressure variation from hub to shroud.

Cho et al. [36] (2009) performed numerical and experimental analyses of a counter-rotating axial fan. The authors studied the effect of the hub-to-tip ratio, taper ratio, and solidity of each blade row on the performance of the axial counter-rotating fan and reported the hub-to-tip ratio has the most effect on the efficiency of the counter-rotating axial fan.

Mistry and Pradeep [37] (2012) numerically and experimentally studied the effects of the speed ratio and axial spacing between rotors in a low-speed contra-rotating axial fan. They found the performance and stall margin of the contra-rotating stage were mainly influenced by the two parameters mentioned above.

Wang et al. [38] (2014) experimentally compared the performance and fluctuation in wall pressure downstream of the first rotor for three different low-speed fan stages: a single rotor, a conventional rotor-stator fan stage, and a counter-rotating fan system. The authors found that the counter-rotating system has the best performance in terms of total pressure rise, efficiency, and operating stability but generates higher aerodynamic noise.

Sun et al. [39] (2017) designed a contra-rotating axial-flow fan for mine ventilation applications with a total pressure ratio of 1.02. Their numerical setup was validated with test data. They numerically studied the aerodynamic characteristics of the fan, including the efficiency, shaft power, and total pressure rise for eight different combinations of the rotational speeds of the rotors. Their results indicated that the rotational speed of the first rotor has a greater effect on the performance of the second rotor and of the counter rotating axial fan than the speed of the second rotor. The authors also showed that the stable operating range of the fan increases by using it in variable speed mode where the best rotor speed combination can be chosen according to the customer requirements.

A few studies have been carried out to apply optimization procedures to improve both the aerodynamic and structural designs of counter-rotating fans. Lengyel et al. [40] (2009) performed both aerodynamic and mechanical optimization of a low speed counter-rotating axial fan stage from an existing aircraft engine. The authors used a multi-objective asynchronous algorithm to find the best blade profile for the counter-rotating application by changing the gas path, leading and trailing edge blade angles, and blade sweep. A comparison of the numerically predicted performance map for the optimized design versus the original design indicates that the optimization improves the stall margin and efficiency.

The German Aerospace Center also started a program for the redesign of a shrouded Propfan (Counter Rotating Integrated Shrouded Propfan - CRISP), as reported in references [41] and [42]. Optimization was used to obtain an improvement of 0.13% in isentropic efficiency. A multidisciplinary automated optimization process that combines aerodynamic performance with mechanical behaviour was also studied. In this optimization process, 106 free geometric parameters were used to find the best configuration for the manufacturing of the blades from fiber-reinforced materials.

2.5 Non-Axial Counter Rotating Compressor

As a preliminary assessment of the counter-rotating centrifugal compressor concept, Dejour and Vo [4] (2018) carried out a numerical evaluation with RANS CFD using ANSYS CFX of a low-speed mixed-flow counter-rotating compressor versus its conventional (rotor-stator) equivalent. A mixed-flow compressor is a hybrid design between an axial and a centrifugal compressor stage. Contrary to an axial rotor, a mixed-flow rotor exhibits a large change in the mean flow radius between its inlet and outlet. On the other hand, contrary to a centrifugal compressor, the flow exits the mixed flow rotor axially (rather than radially for an impeller) and enters a stator (rather than a diffuser). As illustrated in Figure 2-8, the two configurations studied in reference [4] share the same mixed-flow rotor (Rotor 1), but the tandem stator in the conventional configuration is replaced in the counter-rotating configuration by an axial rotor (Rotor 2) turning at the same speed as Rotor 1 (7200 rpm) but in the opposite direction.

The predicted pressure rise coefficient and efficiency characteristics in Figure 2-9 indicate that the counter-rotating configuration delivers double the pressure rise as its conventional equivalent at the design (peak-efficiency) point while keeping the same polytropic efficiency and improving stall margin. It is noted that the polytropic efficiency is the equivalent of the isentropic efficiency as the pressure ratio approaches one and is thus a more suitable efficiency parameter to compare compressors of different pressure ratios. Entropy contours at the exit plane of the Rotor 2 (Figure 2-10a) at the peak efficiency point indicate that the tip clearance flow occupies a large portion of the flow passage due to the low blade height and contributes significantly to aerodynamic loss. Moreover, entropy contours at the blade tip of both rotors taken at the stall point (last stable point) indicate that the incoming tip clearance flow interface has reached the leading edge of Rotor 2 on the pressure side , inferring that Rotor 2 is the source of rotating stall for the counter-

rotating mixed-flow compressor according to the first criterion from Vo et al. [13]. In this case, the tip circumferential speeds of the rotors are less than Mach 0.24, making all compressibility effects negligible and shocks absent.

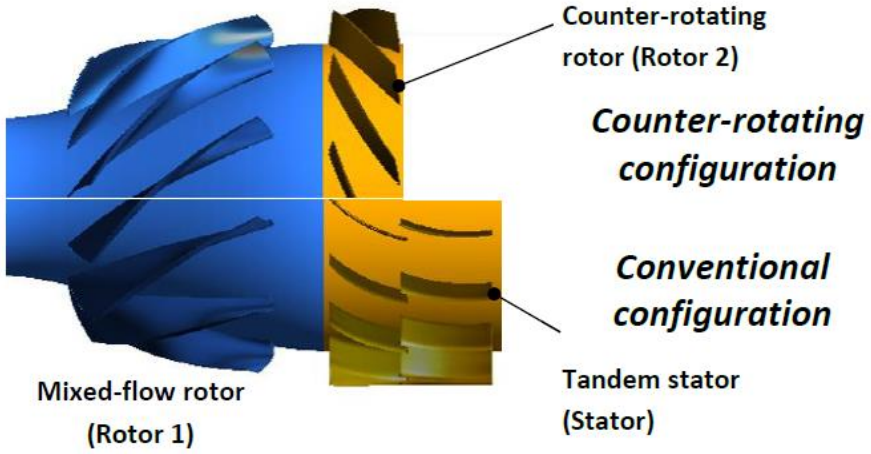

Figure 2-8 Low-speed counter-rotating versus conventional mixed-flow compressors from Dejour and Vo [4]

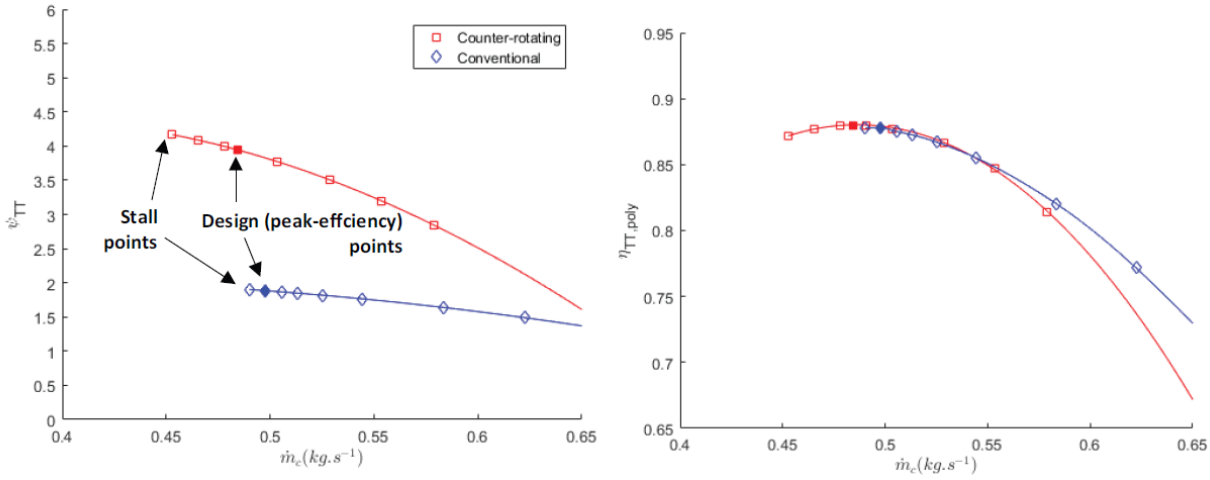

Figure 2-9 Pressure rise coefficient (left) and polytropic efficiency (right) versus corrected mass flow for low-speed counter-rotating versus conventional mixed-flow compressors [4]

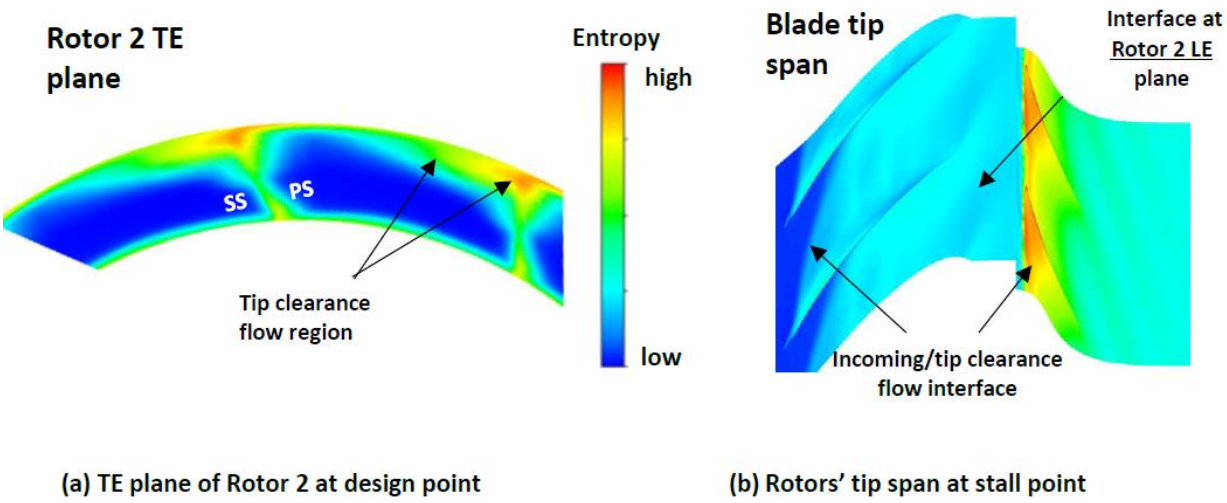

Figure 2-10 Entropy contours for low-speed counter-rotating mixed-flow compressors (adapted from reference [4])

Subsequently, a similar assessment was repeated to compare a low-speed centrifugal counter-rotating compressor with its conventional equivalent [5]. As illustrated in Figure 1-3, the two compressor configurations share the same impeller whose circumferential tip speed is Mach 0.24, while the counter-rotating rotor turns at the same rotational speed as the impeller (7350 rpm) for a tip circumferential velocity of Mach 0.3. Contrasting Figure 1-3 with Figure 2-8, one can observe that the blade height of the downstream rotor in relation to that of the upstream rotor/impeller exit is much smaller in the case of the counter-rotating centrifugal compressor due to the change in mean radius between the exit of the impeller and the inlet of the downstream rotor.

Figure 2-11 shows the pressure rise coefficient and efficiency characteristics for the counter-rotating centrifugal (CRC) compressor versus the equivalent conventional centrifugal (CC) compressor obtained from CFD simulations in ANSYS CFX. The result shows that the CRC configuration provides almost double the total pressure rise of the CC configuration with a better stall margin (larger difference in mass flow between design and stall points). However, contrary to the mixed-flow counter-rotating compressors (Figure 2-9), the centrifugal counter-rotating compressor incurs a significant (5%) penalty in polytropic efficiency from its conventional equivalent. Although it has yet to be confirmed, the cause is likely related to the short blade of the downstream rotor leading to high tip clearance losses. Moreover, the stall mechanism seems to be different than in the case of the counter-rotating mixed flow compressor. Indeed, the

entropy contours at the blade tip in the downstream rotor in Figure 2-12a indicate that the interface has already moved ahead of the leading edge plane at the stall point, contrary to that seen in the mixed flow counter-rotating compressor (Figure 2-10b). At the same time, Figure 2-12b indicates the presence of a large region of axially negative shear stress on the downstream rotor suction side at the stall point due to boundary layer separation, which may be the source of the stall, rather than that proposed by Vo et al. [13].

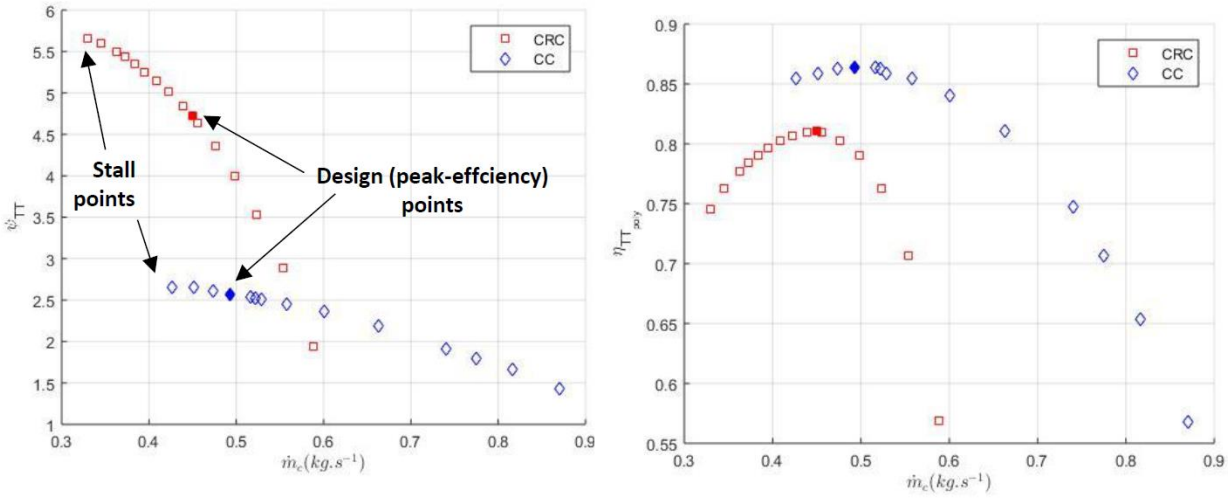

Figure 2-11 Pressure rise coefficient (left) and polytropic efficiency (right) versus corrected mass flow for low-speed counter-rotating (CRC) versus conventional (CC) centrifugal compressors [5]

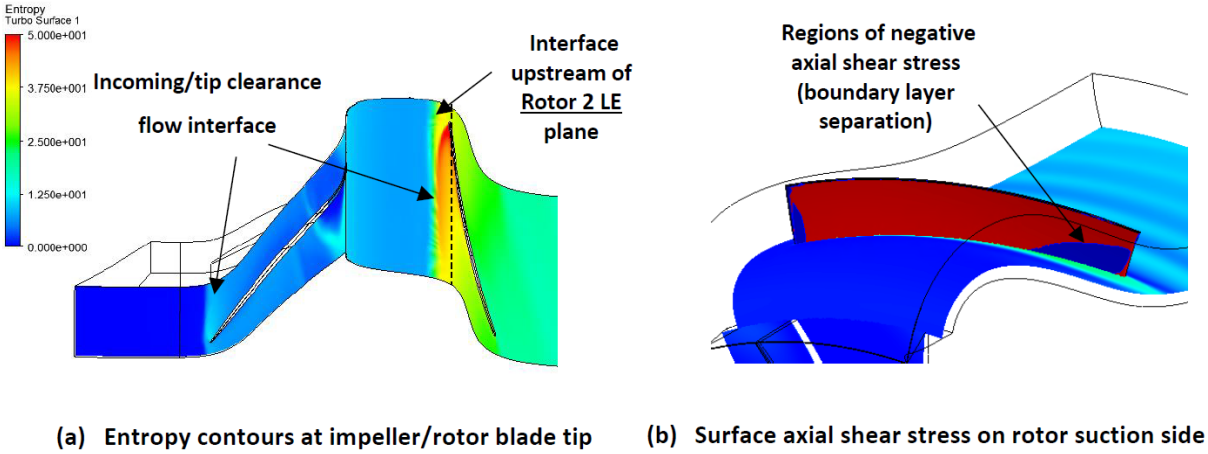

Figure 2-12 Flow assessment at the stall point for counter-rotating centrifugal compressor [5]

CHAPTER 3 METHODOLOGY

3.1 General Methodology

The general methodology is divided into four phases. Phase 1 consists of designing a baseline conventional transonic centrifugal (CC) compressor stage that is representative of one found in an aero-engine. This compressor will share the impeller geometry and design mass flow with the counter-rotating centrifugal (CRC) compressor and sets the latter's design targets, which is to double the total pressure rise while maintaining or improving the polytropic efficiency and stall margin. A vaneless diffuser and counter-rotating rotor are then designed by replacing the CC compressor diffuser to form a CRC compressor design. In phase 2, the first CRC compressor design is analyzed in detail at the design mass flow to identify the causes of any shortfall in performance (total pressure ratio and polytropic efficiency) targets and to quantify the relative importance of each cause. In phase 3, design strategies are proposed and assessed to address the performance shortfall to produce a revised CRC compressor design. Finally, phase 4 evaluates the revised CRC compressor design both at design point to identify the causes for any remaining performance shortfall, and at off-design for determining stall margin and elucidating the cause of rotating stall. Further design improvements are then proposed, if required.

A computational approach is chosen as it allows for relatively rapid assessment of design changes and detailed analysis of the flow field. A state-of-the-art commercial RANS CFD code, meshing software, and post-processing tool will be used to carry out the simulations associated with the four phases of this project.

3.2 Phase 1: Compressor Design

As mentioned in Section 3.1 and illustrated in Figure 3-1, two compressor configurations are designed: a CC compressor and an equivalent CRC compressor sharing the same impeller but with the diffuser replaced by a short vaneless diffuser and counter-rotating rotor. The flow in the compressor is assumed to be adiabatic. In order to start with a good baseline design, the CC compressor configuration is designed based on the layout and specifications of an existing small aero-engine centrifugal compressor for which the increase in pressure ratio provided by the CRC compressor concept could be highly beneficial in terms of specific fuel consumption. As shown

in Figure 3-1a, the chosen CC compressor design has fishtail-type pipe diffusers, which are often used in aero-engine compressors as this type of diffuser provides relatively high efficiency as well as compactness and simplicity since the pipes can turn the flow exiting the impeller both circumferentially and radially back to the axial direction.

Based on design experience gathered with the low-speed CRC compressor design in reference [5], the downstream rotor in the first CRC compressor design is an axial rotor (Figure 3-1b) rather than the non-axial design seen in Figure 1-1, leaving a longer vaneless diffuser between the impeller exit and the downstream rotor inlet as shown in Figure 3-1b. This longer vaneless diffuser is necessary to reduce the high swirl of the flow exiting impeller before it enters the downstream rotor. Otherwise, the flow entering the downstream rotor would be almost circumferential making the blade design impractical.

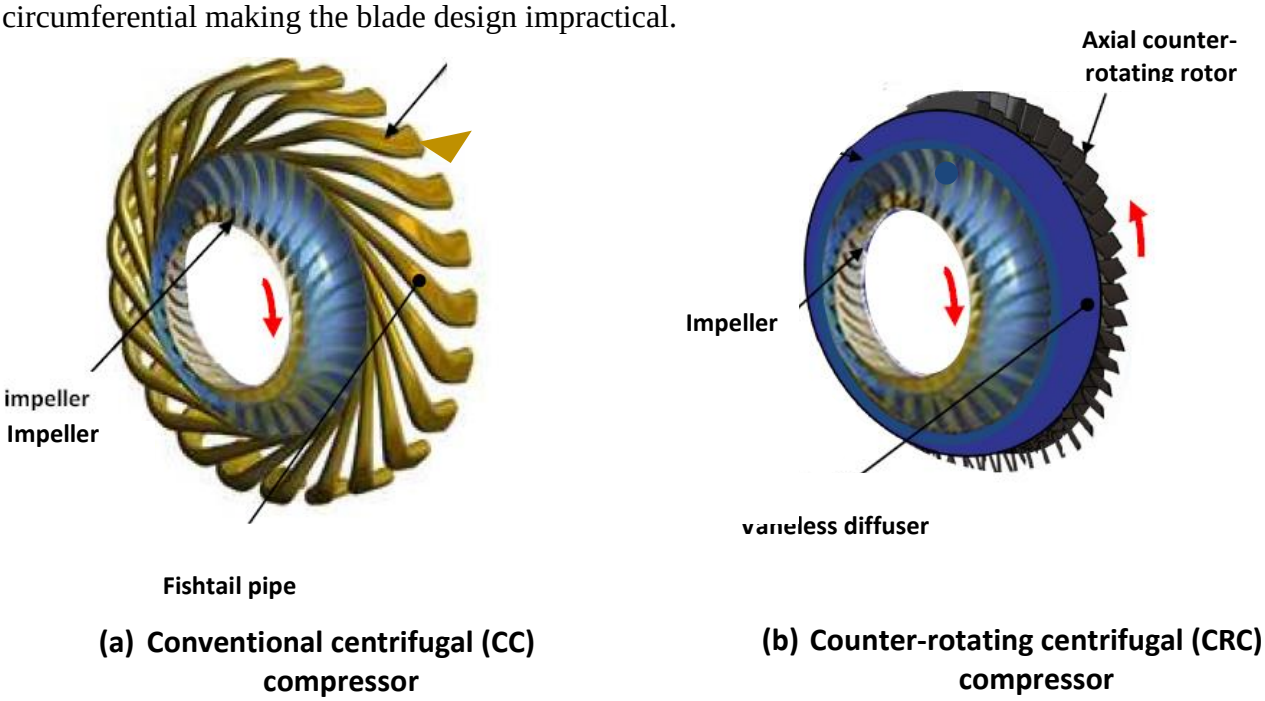

(a) Conventional centrifugal (CC) compressor

(b) Counter-rotating centrifugal (CRC) compressor

Figure 3-1 Conventional centrifugal compressor and counter-rotating centrifugal compressor (adapted from reference [3])

The design specifications for the CC compressor come from the last stage of an aero-engine. As such, the compressor inlet conditions are not atmospheric. For the CRC compressor, the speed of the downstream rotor is set to be the same as that of the impeller and the specifications call for the total pressure rise to be doubled that of the CC compressor (such that the total pressure ratio is $PR_{tt,CRC} = PR_{tt,CC}+PR_{tt,CC}-1$) while maintaining the polytropic efficiency and stall margin, and having a smaller size in both the radial and axial directions. Table 3-1 lists the design

specifications for both compressors which are based the data from a real engine. In either case, the number of diffuser pipes or downstream rotor blades is set to be the same as the number of impeller blades such that unsteady simulations can later be performed at low cost (single blade passage per row) to capture the effect of flow unsteadiness, which may be relevant near stall. Based on current design practices, both rotors are unshrouded with the impeller tip clearance set to a typical value of 0.010 inch (0.254 mm). Given the short blade span of the downstream axial rotor in CRC compressors, its tip clearance is set at the minimum practical value of 0.005 inches (0.127 mm). The design is split into four components, namely the impeller, which is common to both configurations, the fishtail pipe diffuser for the CC configuration, and the vaneless diffuser and counter-rotating axial rotor for the CRC configuration.

Table 3-1 Design specifications

Parameter	CC	CRC
Impeller total pressure ratio (PR)	5.85-5.95	same
Impeller polytropic efficiency	0.92-0.94	same
Impeller inlet diameter	99 mm	same
Impeller exit diameter	237.5 mm	same
Stage total pressure ratio (PR)	5.10	9.20
Stage polytropic efficiency (η_{tt})	0.86-0.88	same
Maximum diameter	367 mm	240-367 mm
Maximum axial length	161 mm	below 161 mm
Inlet total pressure (P_{01})	253.9 kPa	same
Inlet total temperature (T_{01})	368.5 K	same
Inlet flow direction	Axial	same
Outlet flow direction	Axial	same
Exit Absolute flow angle	0	same
Design mass flow ($\dot{m}$)	2.94 kg/s	same
Impeller speed	46,946 rpm	same
Downstream rotor speed	-	46,946 rpm
Impeller tip clearance	0.254 mm	same
Downstream rotor tip clearance	-	0.127 mm

3.2.1 Impeller and Rotor Design

The design of the impeller and axial rotor involves a preliminary design phase based on analytical modeling and loss/deviation correlations and, in the case of the impeller, a detailed design phase using CFD simulations.

Preliminary Design

The preliminary design phase in turbomachinery is a 1-D design made along a line in the middle of the gas path, called *meanline* (dashed line in Figure 3-2a), separating the normal flow area in two equal parts, along which the flow properties represent the average values at that particular meridional location. The meridional direction is the direction along the meanline. This section provides a brief qualitative description of the preliminary (or meanline) design process used. The details can be found in references [43-47] for the impeller and in references [48-49] for the axial rotor. The explanation will concentrate on the impeller first with the particularities for the axial rotor covered subsequently. Air is assumed to be a calorimetrically perfect gas. Figure 3-2 depicts the useful parameters for the preliminary design of an impeller through velocity triangles, with *C* denoting velocities in the stationary frame while *W* denotes velocities in the rotating frame. *C* and *W* are connected through the blade circumferential velocity ($\omega \cdot r$), with ω and r denoting the rotational speed and local radius, respectively.

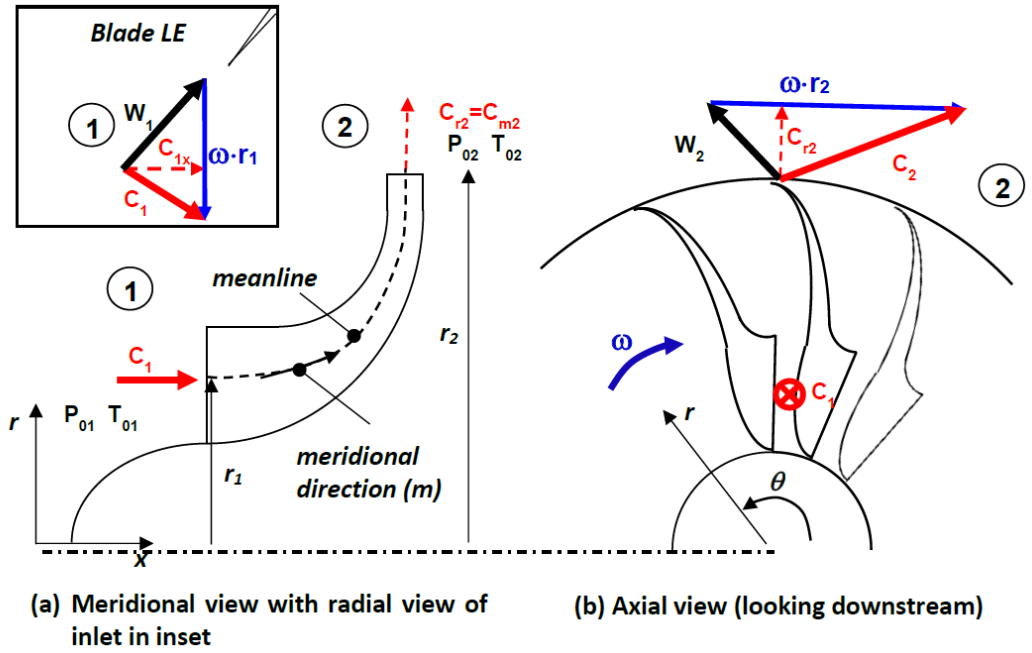

Figure 3-2 Preliminary design of impeller

The preliminary (or meanline) design starts with the definition of a gas path between the inlet (Station 1) and exit (Station 2) planes of the impeller so that the meanline can be defined as illustrated in Figure 3-2a. This is done with mass flow conservation through equation (3.1), where $\dot{m}$ is the prescribed mass flow, ρ the density, C_m the meridional velocity, and A the local area perpendicular to the meridional direction. The chosen hub and shroud lines, and thus meridional A distribution, determine the meridional velocity along the gas path. The general shape of the initial hub gas path is inspired by that of existing impellers.

$$\dot{m} = \rho C_m A \tag{3.1}$$

Equation (3.2) (Euler's turbine equation) is then used to calculate the exit total temperature (T_{02}) from its value (known) at the inlet (T_{01}) and the inlet and exit circumferential velocity components at the inlet ($C_{1\theta}$) and exit ($C_{2\theta}$), both of which depends on the local blade circumferential velocity ($\omega \cdot r$), absolute inlet velocity (C_1) and relative exit velocity (W_2) according to the velocity triangles in Figure 3-2. The inlet blade angle is usually set to the angle of the inlet relative velocity vector (W_1) for zero incidence at design mass flow. It is noted that the compressor inlet velocity is axial for the current design such that $C_{1\theta}=0$ for the impeller. The relative exit velocity vector (W_2) depends on the exit radial (meridional) velocity (C_{m2}) and exit relative flow angle, which is the chosen blade exit angle minus a deviation angle obtained using empirical correlations from reference [50]. The deviation usually mainly depends on the blade solidity (blade chord/circumferential spacing) and flow turning (set by relative inlet and exit flow angles).

$$c_p(T_{02} - T_{01}) = \omega(r_2 C_{2\theta} - r_1 C_{1\theta}) \tag{3.2}$$

The last step consists of obtaining the exit total pressure (P_{02}). One first obtains the ideal exit total pressure (P_{02s}) from an isentropic compression between T_{01} and T_{02} using equation (3.3), where γ is the specific heat ratio of air. The ideal exit total pressure in the relative frame ($P_{02s,rel}$) is then calculated from (P_{02s}) and the exit velocities (C_2 and W_2) via the static pressure (P_2) with the isentropic relations for a calorimetrically perfect gas in equations (3.4) and (3.5). The total pressure loss ($\Delta P_{0,loss}$) obtained from empirical correlations [49] (which are traditionally based on blade cascade tests) can then be subtracted from $P_{02s,rel}$ to obtain the final relative total pressure ($P_{02,rel}$) which is then converted back to (P_{02}) through equation (3.5) which is based on the static pressure P_2 being the same between the absolute and relative frames. The (relative frame) total

pressure losses are usually dependent on the blade solidity, flow turning by the blades and blade profiles and tip clearance size, all of which are selected by the designer.

$$\frac{P_{02s}}{P_{01}} = \left(\frac{T_{02}}{T_{01}}\right)^{\frac{\gamma}{\gamma-1}} \tag{3.3}$$

$$\frac{T_2}{T_{02}} = \left(1 + \frac{\gamma-1}{2}\frac{{C_2}^2}{\gamma R T_2}\right)^{-1} \tag{3.4}$$

$$\frac{P_{02s,rel}}{P_{02s}} = \left(\frac{1+\frac{\gamma-1}{2}\frac{{W_2}^2}{\gamma R T_2}}{1+\frac{\gamma-1}{2}\frac{{C_2}^2}{\gamma R T_2}}\right)^{\frac{\gamma}{\gamma-1}} \tag{3.5}$$

The total pressures and temperatures can then be used to calculate the impeller total pressure ratio (PR) and polytropic efficiency (η_{poly}), according to equations (3.6) through (3.7).

$$PR_{tt} = \frac{P_{02}}{P_{01}} \tag{3.6}$$

$$\eta_{poly} = \frac{\gamma-1}{\gamma} \cdot \frac{ln\left(\frac{P_{02}}{P_{01}}\right)}{ln\left(\frac{T_{02}}{T_{01}}\right)} \tag{3.7}$$

Using the specifications in Table 3-1, the geometrical design parameters, namely gas path, blade shape, relative spacing between blades (solidity), blade exit angle are varied until the values of impeller total pressure ratio and polytropic efficiency meet their targets.

For the meanline design of the downstream axial rotor, the procedure is the same as for the impeller except that the meanline is at constant radius, given the choice in this case to have constant hub and tip radii for simplicity. The corresponding velocity triangles at the meanline radius is shown in Figure 3-3. The inlet conditions to the axial rotor depend on the vaneless diffuser. As such, a total pressure loss factor is estimated for the vaneless diffuser (see section 3.2.3) that is subtracted from the total pressure exiting the impeller to obtain the inlet total pressure to the axial rotor. The total temperature stays the same at the exit of the impeller since no work is done in the vaneless diffuser. As for the inlet velocity to the axial rotor, its meridional (axial in this case) component is obtained through mass conservation across the vaneless diffuser according to equation (3.1) while its circumferential component is obtained through conservation of angular momentum ($r \cdot C_\theta$ = constant) from the value at the impeller exit. With the design of the

impeller and vaneless diffuser in place, the geometrical design parameters of the axial rotor are iterated upon until the CRC compressor total pressure ratio and polytropic efficiency are deemed acceptable (meet or come as close as possible to targets).

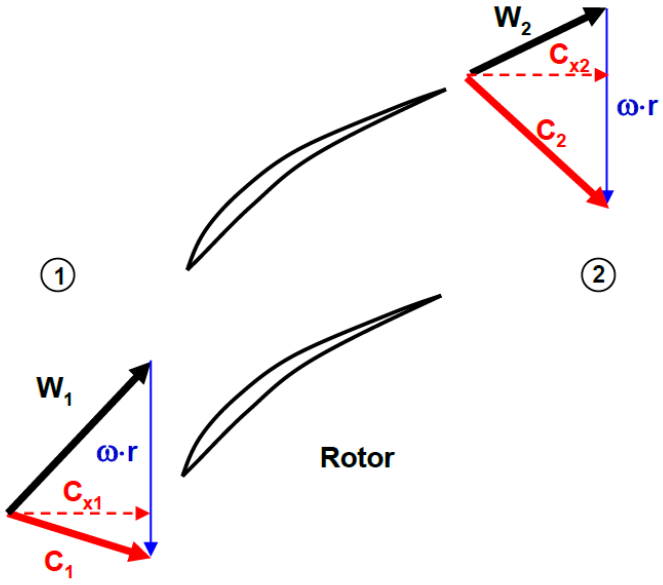

Figure 3-3 Preliminary design of axial rotor

Once the meanline design is done, a 3-D blade shape has to be generated to start the detailed design phase. For the axial rotor, the meanline design is repeated at other spans from hub to tip with the constraint that the exit flow remains axial, which sets the exit flow angle at each span through the outlet velocity triangle in Figure 3-3. Deviation correlations from reference [50] are then invoked to find the exit blade angle. To avoid highly time-consuming optimization of the axial rotor at this early stage, the blade profile chosen for all spans in this first CRC design is a double circular arc (DCA). This simple profile, formed by the superposition of two circular arcs of different radii to form the blade pressure and suction sides, has been used for relative inlet Mach number of up to 1.65 [51]. The profiles are stacked along a radial stacking line passing through the mid-chord of each profile, as shown in Figure 3-4. It is noted that, unlike the design of regular axial rotors, a through flow design using quasi-3D analysis is not carried out prior to full 3D CFD simulations. The reason is that the blade aspect ratio in this application is so much smaller than for typical axial compressor rotors, resulting in important three-dimensional effects from the tip clearance flow and hub boundary layers that render quasi-3D design tools (as well as

other analytical tools such as tip clearance loss correlations) inaccurate. As such, full 3D analysis remains the only tool to predict with some confidence the performance of such a rotor.

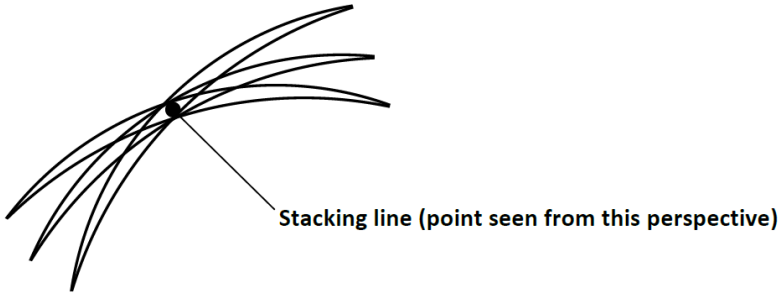

Figure 3-4 3-D blade construction for axial rotor through profile stacking

For the impeller, the 3-D blade construction is much more difficult than for an axial rotor. Consequently, the 3-D impeller blade is generated with the commercial software ANSYS BladeGen with specified geometrical parameters determined from the preliminary design. Appendix A describes in more detail the 3-D blade generation processes in ANSYS BladeGen.

Detailed Design

The detailed design phase consists of using steady-state CFD simulations to capture 3-D flow structures for high-fidelity assessment and fine-tuning of the 3-D geometries produced in the preliminary design phase. The simulations are carried out in steady-state mode at the design mass flow. The details of the numerical setup are given in section 3.3. In the post-processing of the simulated flow field, the mass–averaged total pressure (P_0) and total temperature (T_0) are taken at the inlet and exit planes of the computational domain and used to calculate total pressure ratio and efficiencies according to equations (3.6) through (3.8). For the impeller, the flow field is verified for any boundary layer separation, and the design altered iteratively to meet performance targets. The axial rotor geometry is not fine-tuned at this stage in order to identify the issues associated with using simple high-speed (DCA) blade profiles and to address them in design improvements.

3.2.2 Fishtail Pipe Diffuser Design

Due to the lack of reliable loss models for the fishtail pipe diffusers, an analytical preliminary design phase was not performed. In fact, except for a recent publication by Han et al. [52], very little public information is available on the design of this type of diffuser. Figure 3-5 shows the

main design parameters for fishtail pipe diffusers, which are the inlet angle, centerline trajectory, cone length, area distribution (along the centerline), and area shape transition from circular to a flattened cross-section composed of a rectangle and two half-circles. A design procedure is set up which uses steady-state CFD simulations to simulate different design iterations of the pipe diffusers. With the inlet conditions and inlet centerline angle fixed from the impeller outlet conditions and the area shape transition set according to that shown in reference [52], the fishtail pipe design was varied iteratively by changing the centerline trajectory, cone length and area distribution according to the different lines shown in Figure 3-6 (each line representing an iteration) and simulated with the impeller until the stage performance meet the targets set in Table 3-1 without flow separation. The details of the numerical setup are given in section 3.3.

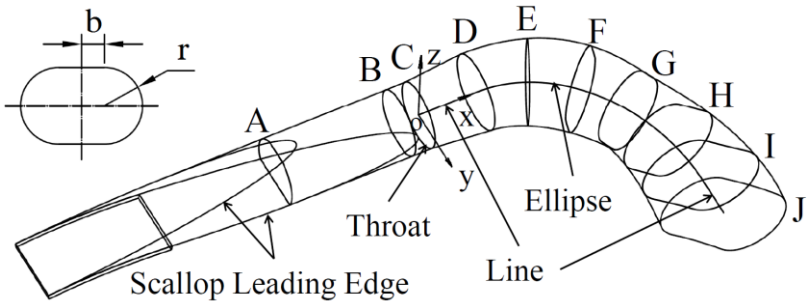

Figure 3-5 Fishtail pipe diffuser design parameters [52]

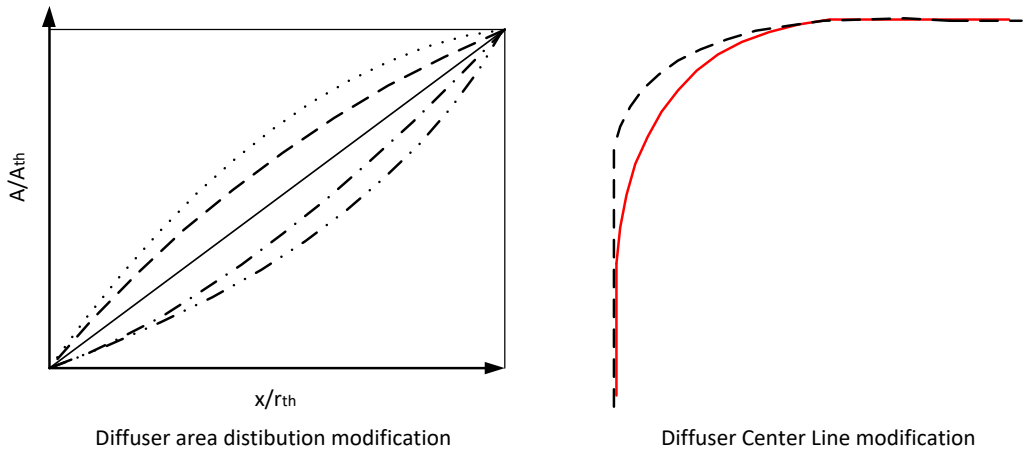

Figure 3-6 Parametric variation in area distribution and centerline trajectory for fishtail pipe diffuser design iteration

3.2.3 Vaneless Diffuser Design

Similar to the case of the pipe diffuser, a preliminary (analytical) design was not performed for the vaneless diffuser due to lack of loss correlations for this particular shape. Again, steady-state

CFD simulations were relied upon to assess the design. The details of the numerical setup are given in section 3.3. Figure 3-7 illustrates the design parameters for the vaneless diffuser, namely the hub curvature radius (*r*) and the meridional area distribution

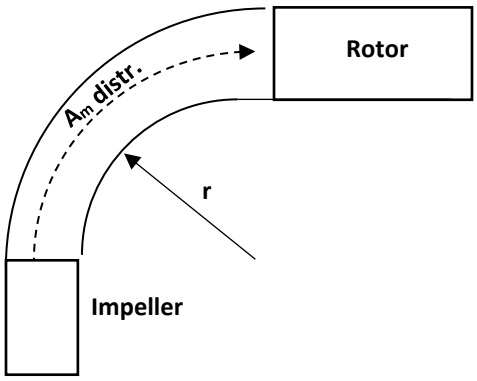

Figure 3-7 Vaneless diffuser design parameters

For the first parameter, experience gained from the design of the CRC in reference [5] indicates that the high-swirl flow exiting the impeller can tolerate a small hub curvature radius without boundary layer separation. A small hub curvature radius reduces wetted surface (viscous loss) and the radial and axial extent of the CRC compressor. As for the second parameter, maintaining a constant area distribution would result in a downstream rotor blade height that is unacceptably small due to the small impeller exit blade height (from high compression across the impeller) combined with the change in radius from the impeller exit to the rotor inlet (linked to the first design parameter). As a result, the endwall losses, especially the tip clearance loss on the axial rotor, may result in a large penalty on the stage performance. On the other hand, a large increase in area along the meridional direction will lead to boundary layer separation (performance penalty) and/or relative flow angle to the downstream rotor that is too close to the circumferential direction (due to low axial velocity relative to blade rotational velocity) making the axial rotor very hard to design. In this case, a constant area distribution would have resulted in a rotor blade height of only 3 mm. Consequently, a positive area gradient was selected to provide a rotor blade height of 4.4 mm. The value of *r* was then iterated upon to get the smallest value for which flow separation did not occur in the vaneless diffuser. The final relative inlet flow angle (and thus axial rotor leading edge angle) is 81.05 degrees (relative to the axial direction). It is noted that this unusually high but still manageable relative flow angle is the result of swirl reduction through the vaneless diffuser. A shorter vaneless diffuser, as shown in Figure 1-1 for a non-axial counter-

rotating rotor, could result is such a small swirl reduction as to make a relative flow angle that is too close to 90 degrees (circumferential direction) for a practical downstream rotor design.

3.3 Computational Setup

The CFD simulations are performed using the commercial CFD code ANSYS CFX (Version 19), mainly in steady mode. ANSYS CFX is a pressure-based, cell-centered and finite-volume Reynolds-Averaged Navier-Stokes (RANS) CFD code for both structured and unstructured grids, which is well known for turbomachinery simulations and is used in the aero-engine industry. Figure 3-8 shows the computational domain for the CC compressor configuration with its boundary conditions. The domain is split into two subdomains, a rotating subdomain for the impeller (with inlet duct) and a stationary subdomain for the pipe diffuser. The axial length of the inlet section upstream of the impeller leading edge is longer than the blade pitch to ensure that potential perturbations from the impeller blades (one blade pitch in wavelength) attenuates to zero at the domain inlet.

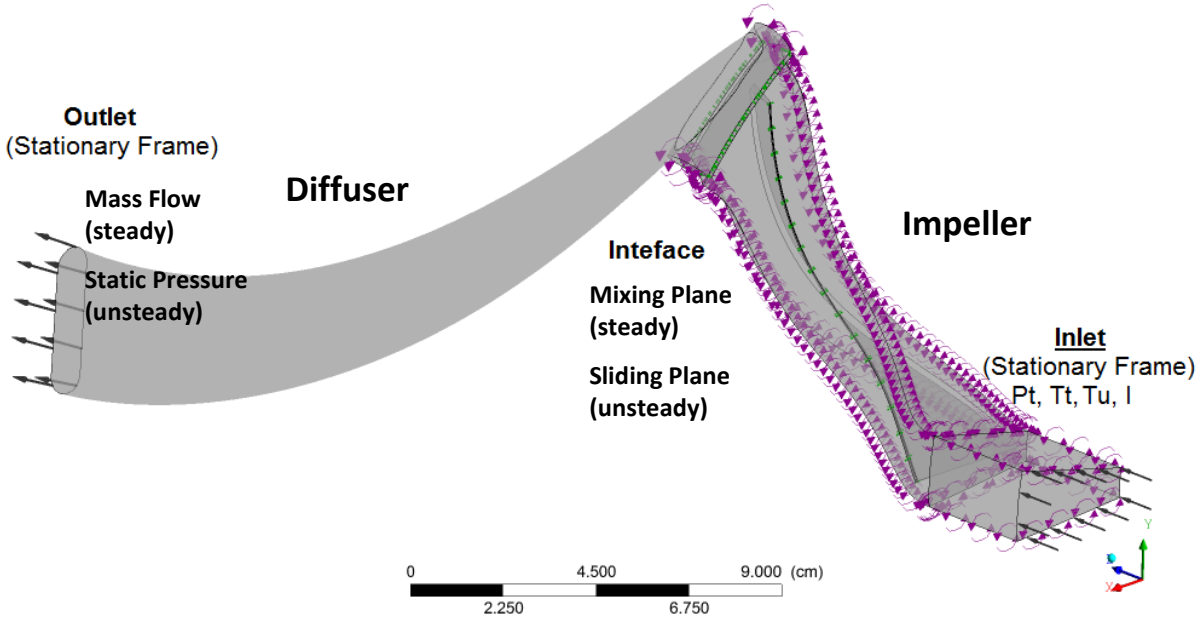

Figure 3-8 Computational domain for CC compressor configuration

Given the requirement for the same number of impeller blade passage and diffuser pipe, each subdomain contains a single passage/diffuser pipe with the same circumferential (angular) extent for the possibility of later carrying out unsteady simulations with a single blade passage. A

mixing plane interface is used between the two subdomains for steady-state simulations, and a sliding plane interface for unsteady simulations. A periodic boundary condition is applied to the lateral boundaries of the impeller subdomain, while the inlet boundary conditions consist of uniform inlet total pressure and total temperature (values from Table 3-1), zero swirl angle (axial inflow) and uniform turbulence intensity. The boundary condition at the outlet of the domain is a prescribed mass flow for steady-state simulations and prescribed average static pressure for unsteady simulations, the latter being more physical when the flow is unsteady as it is the mass flow that often oscillates rather than the back pressure. In both cases, ANSYS CFX does not impose a uniform static pressure at the exit but allows the local static pressure to vary according to the flow (e.g. radial equilibrium). A no-slip boundary condition is applied to all solid surfaces. A second-order upwind numerical discretization scheme is chosen for the simulations. The convergence criterion for the steady-state simulations is the maximum residual falling below 10^{-4}. For unsteady simulations, convergence is considered achieved when monitoring parameters, such as mass flow, oscillate at constant amplitude around a constant mean value.

Figure 3-9 presents the computational domain for the CRC compressor, which is composed of three subdomains. These are the rotating impeller subdomain (the same as in Figure 3-8), the stationary vaneless diffuser subdomain, and the counter-rotating rotor (and outlet duct) subdomain. Again, all three subdomains have the same circumferential (angular) extent with a single passage for both impeller and rotor. Similar to the CC configuration, a mixing plane interface is used between the subdomains for steady-state simulations and a sliding plane interface for unsteady simulations. Aside from the periodic boundary conditions being used at the lateral boundaries of all three subdomains, all other boundary conditions are the same as those for the CC compressor computational domain. The axial length of the exit section downstream of the axial rotor trailing edge is equal to its blade pitch as per best practice for exit subdomains with circumferential periodicity.

Given the high Reynolds number (on the order of 10^7) and the fact that the present compressor configurations are intended to be at the rear of the aero-engine, the boundary layer is assumed to be fully turbulent (no boundary layer transition) and the inlet turbulence intensity is set at 5% . This turbulence intensity value has been used by Bourgeois et al. [53] for simulating a similar rear centrifugal compressor stage with their results validated against test data. The Shear Stress Transport (SST) turbulence model with automatic wall function option is chosen for all

simulations. This model is based on the k-omega model and accounts for the transport of the turbulent shear stress. It has been used and validated against test data for both centrifugal [53] and axial compressors [54]. It is also rated by ANSYS [55] as the most accurate model for capturing flow separation in turbomachinery.

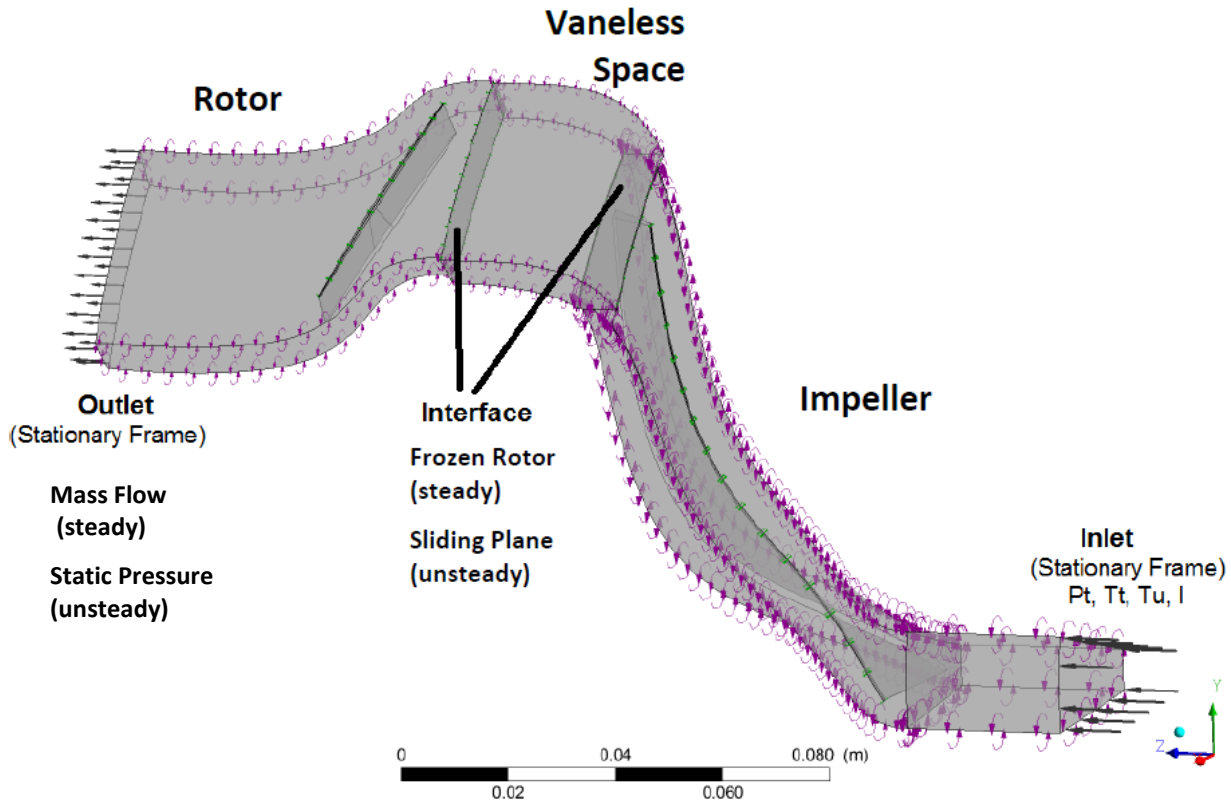

Figure 3-9 Computational domain for CRC compressor configuration

Phases 1 through 3 of the present research rely exclusively on steady-state simulations to assess the initial designs and performance improvement strategies at the design mass flow where flow unsteadiness is relatively small. For the assessment of the final CRC compressor design versus the CC compressor in phase 4, (more time-consuming) unsteady simulations are added to quantify the effect of unsteadiness from wake and potential interactions between adjacent blade rows on the performance at design mass flow as well as to find the stall point, where flow unsteadiness could be important. For unsteady simulations, a small time step equivalent to 60 time steps per blade passing is chosen at the start of the simulation to help convergence and is eventually reduced to 30 time steps per blade passing. When stable flow fluctuations occur after convergence, the flow solution is averaged in time over an integer number of oscillation periods to obtain a time-averaged flow field that can be analyzed.

It is noted that single blade passage simulations are strictly speaking not adequate to capture the spike stall inception process itself where flow periodicity breaks down due to the stall inception perturbation extending over many blade passages. However, single blade passage simulations should be adequate to capture the stall point. For modal stall, single blade passage simulations can capture the total-to-static pressure rise characteristics to find the point where its slope goes to zero. However, it would require simulation of all of the compression stages. As such, single blade passage simulations of a single stage is more appropriate for capturing the stall point for spike stall inception, which originates in flow breakdown at the blade passage level. In fact, Vo et al. [13] showed that the convergence limit in single blade passage simulations of a compressor rotor results in spike stall inception at the same mass flow in an equivalent multiple blade passage simulation. Furthermore, these authors showed that the flow breakdown process in a diverging unsteady single blade passage simulation with the exit static pressure pushed beyond that at the convergence limit (which can be referred to as “single passage” stall transient) is similar to that in the blade passage(s) downstream of the spike stall perturbation as it travels from one blade passage to another. This means that unsteady single blade passage simulations can be used in the current case to capture the stall point (convergence limit) as well as the post-convergence flow field breakdown to find the cause of rotating stall (for spike stall inception).

To help elucidate the source of rotating stall in phase 4, the stall point of the impeller is obtained by simulating the impeller alone using the computational domain shown in Figure 3-10. It couples the same impeller subdomain from Figure 3-8 and Figure 3-9 with a radial diffuser with inviscid end walls to ensure that stall occurs in the impeller. The inviscid radial diffuser subdomain has lateral boundaries with periodic boundary conditions and rotates with the impeller. As such, it is connected to the impeller subdomain through a simple GGI interface across which the flow properties are simply interpolated. The radial extent of the inviscid diffuser is longer than the impeller exit blade pitch as per best practice.

The meshing for the subdomains with blade rows (impeller and rotor) is performed with ANSYS TurboGrid, a meshing software for turbomachinery using a structured mesh. All other subdomains are meshed with ICEM CFD using an unstructured mesh. Mesh studies are carried out to determine the adequate mesh density for each component. The details are reported in Appendix B. Figure 3-11 shows the final mesh for each subdomain, with the mesh in the tip clearance included for the impeller and rotor subdomains. The mesh for the CC and CRC

configuration contain about 2 million and 2.1 million elements, respectively. The number of spanwise nodes used in the tip clearance of the impeller and axial rotor is 34 and 49, respectively.

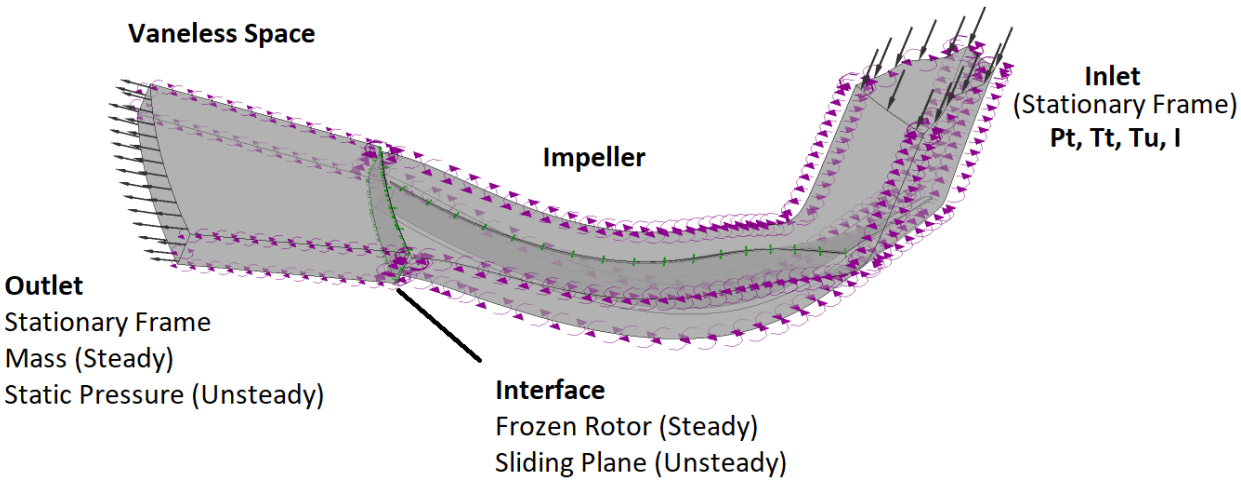

Figure 3-10 Computational domain for impeller simulations

3.4 Phase 2: Analysis

Once the design of the CC and CRC compressors are completed in phase 1, a detailed analysis is performed on the CC compressor design to ensure that it is an adequate reference and on the initial CRC compressor design to identify its performance shortfalls and to determine the causes.

3.4.1 CC Compressor Assessment

First, the CC compressor design is validated to ensure that it is a good design for use as a benchmark/reference for the CRC compressor design. This is done by verifying that integral performance parameters (total pressure ratio, polytropic efficiency) and exit flow angle at design mass flow meets the targets set in Table 3-1.

ANSYS CFX-Post, a post-processing software with special features for turbomachinery, is used to obtain the inlet and exit total pressures and temperatures at design mass flow. P_{01} and T_{01} are obtained from mass-averaging total pressure and total temperature at an axial plane 5% of impeller axial chord upstream of the impeller leading edge. P_{02}, T_{02} and the average exit flow

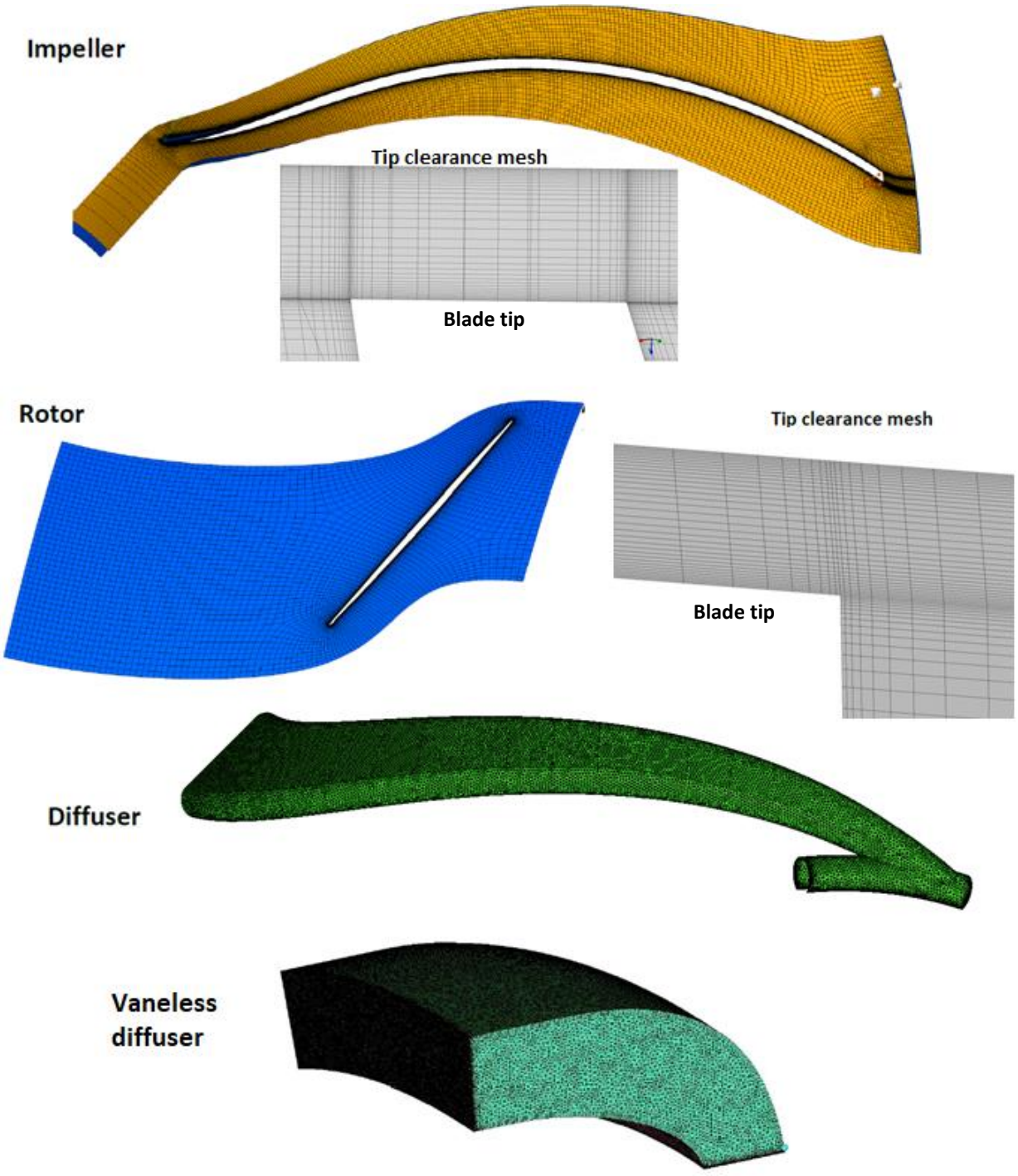

Figure 3-11 Mesh for computational subdomains

angle are obtained from mass-averaging total pressure, total temperature and circumferential flow angle at the diffuser exit plane of the fishtail pipe diffuser. The total pressure ratio and polytropic efficiency of the CC compressor are then calculated according to equations (3.6) and (3.7) and compared along with the mass-averaged exit flow angle against their target values. These steps are also repeated with P_{02}, T_{02} taken at just upstream of the impeller-diffuser interface to calculate the impeller pressure ratio and polytropic efficiency and verify that they also meet their targets.

Subsequently, the design point flow field of the CC compressor is analyzed to ensure that there is no boundary layer separation. This is verified through surface streamlines for the impeller blades and fishtail diffuser plotted by ANSYS CFX-Post.

3.4.2 CRC Compressor Assessment

The first CRC compressor design is then assessed in terms of integral performance parameters (total pressure ratio and polytropic efficiency) and exit flow angle at design mass flow against their targets in Figure 3-1 to identify any shortfall, especially in term of polytropic efficiency. The process of obtaining the integral performance parameters is similar to the CC, with the exit total pressure, total temperature and flow angle taken at an axial plane located at 5% of rotor axial chord downstream of the axial rotor trailing edge.

Next, the causes of the shortfall are elucidated and quantified. The CRC flow field at the design mass flow are analyzed using ANSYS CFX-Post with a particular focus on the downstream counter-rotating rotor as the literature review on counter-rotating compressors in Chapter 2 had identified the downstream rotor to be highly influential in terms of stage performance and stall. Moreover, the sources of losses in axial compressor identified from the literature review are boundary layer (viscous losses), tip clearance flow and shocks.

As such, streamlines and shear stress contours on blade surfaces (similar to Figure 2-12b) are used to detect the presence and extent of boundary layer separation. The entropy contours at the trailing edge plane of the axial rotor in the CRC configuration (similar to Figure 2-10a) can be used to evaluate the influence of the tip clearance on losses through the size and entropy deficit associated with the tip clearance flow region. Finally, Mach number contours at different spans allow for determining the relative inlet Mach number for the axial rotor and identifying the shock

pattern in terms of number of shocks and shock angle (with a multiple-shock system having less loss than a single shock).

The relative contribution of each source of loss in the axial rotor is then quantified to help determine which source can and should be tackled to revise the axial rotor design and improve CRC compressor performance. This is done by re-simulating the axial rotor with inviscid blades and without tip clearance and comparing the change in its polytropic efficiency to deduce the contribution of each of the three sources (boundary layer, tip clearance and shocks) to the total polytropic efficiency deficit (from 100%) of the axial rotor. One can then figure out which source(s) to address first to arrive at a polytropic efficiency value for the axial rotor that would allow the CRC compressor to reach the same polytropic efficiency as the CC compressor.

3.5 Phase 3: Design Improvement

Based on the likely loss sources for the axial rotor being the limiting factors for CRC compressor performance, design strategies could be thought out to reduce their magnitude, should the need arise. Phase 3 sets out to address the sources of losses in the axial rotor of the first CRC compressor design identified in phase 2 through redesign of the components downstream of the impeller. Several design strategies are proposed, which are described in the subsections below. The strategies are to be assessed sequentially through CFD simulations and the CRC compressor design updated with each successful strategy.

To illustrate the effect of certain design improvement strategies on the flow, Figure 3-12 shows the velocity triangles at different stations across the CRC compressor. Stations 1 and 2 represent the inlet and exit of the impeller, while stations 3 and 4 denote respectively the inlet and exit of the counter-rotating axial rotor. As defined previously, C and W denote velocities in the stationary frame and relative (rotating) frames, respectively, while U is the local blade circumferential velocity ($\omega \cdot r$).

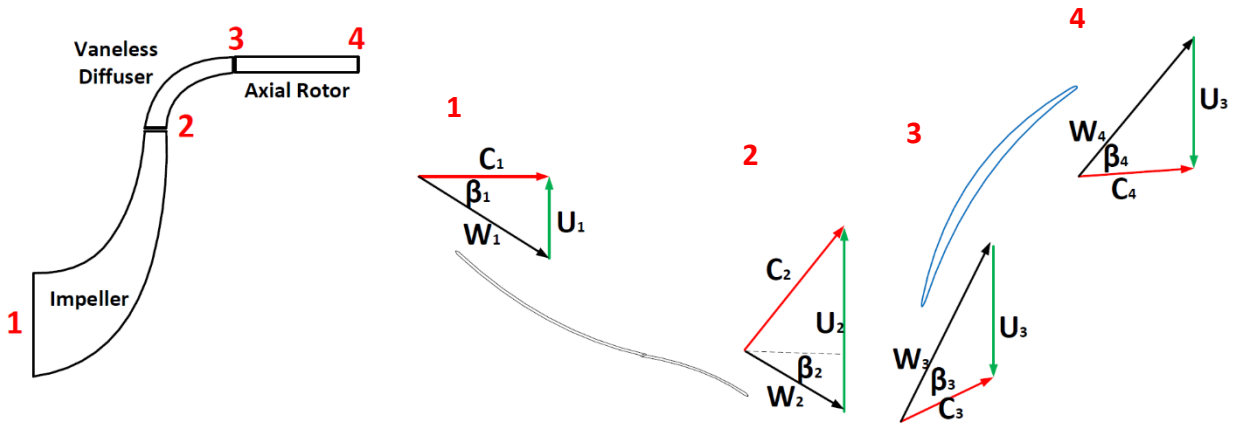

Figure 3-12 Velocity triangles across CRC compressor

3.5.1 Gas Path Modification

A modification in the vaneless diffuser gas path to reduce the hub and tip radii of the downstream rotor as well as increase the gas path height, as illustrated in Figure 3-13, can bring about two advantages. The first is the reduction in the circumferential blade velocity and incoming axial velocity of the axial rotor (U_3 to U_3' and C_{3x} to C_{3x}' in Figure 3-14). As a result, the incoming relative velocity would decrease (W_3 to W_3' in Figure 3-14), reducing shock strength and thus losses from shocks and shock-boundary layer interaction (boundary layer thickening and/or flow separation). The second advantage is the increase in rotor blade height to reduce the effect of tip clearance and thus improve efficiency (and stall margin).

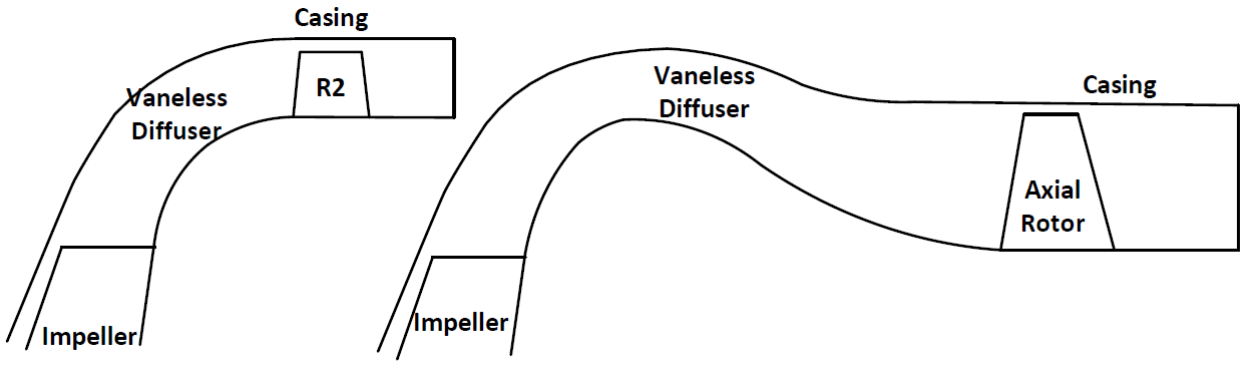

Figure 3-13 Gas path modification

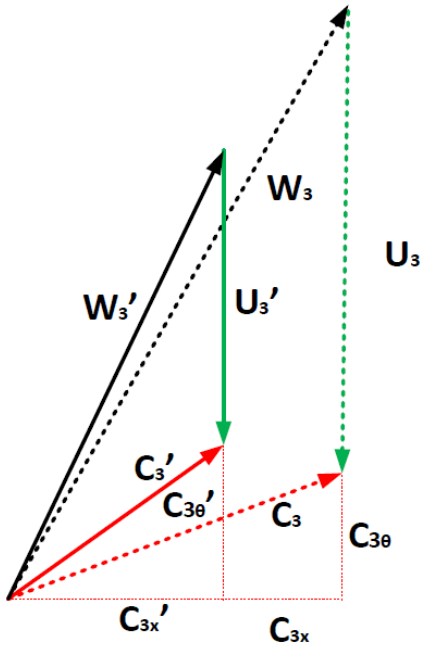

Figure 3-14 Effect of gas path modification on velocity triangle at the inlet of axial rotor

However, this strategy has three potential drawbacks that may reduce or negate its effectiveness. First, a lower mean radius for the rotor means that the circumferential component of the absolute incoming velocity is higher at the rotor leading edge ($C_{3\theta}$ to $C_{3\theta}$‘ in Figure 3-14) due to the smaller change in radius from the impeller exit to axial rotor inlet (conservation of angular momentum). The higher value of $C_{3\theta}$ can partially negate the reduction in relative inlet velocity (W_3) from reduced U_3, as well as bring the relative inlet flow (and thus axial rotor blade leading edge angle) closer to the circumferential direction, making the rotor design more difficult. Second, as can be deduced from the velocity triangle in Figure 3-14, a lower rotational velocity (U_3’) will require more flow turning (camber) from the rotor blade to maintain the exit flow axial (and thus do the same work). More camber increases the risk of boundary layer separation and its associated negative impact on efficiency (and stall margin). Last but not least, the higher hub and/or shroud curvature of the vaneless diffuser gas path can result in flow separation. An axial length increase to mitigate this effect would not only lengthen the CRC but also bring about more viscous losses from added wetted surface area.

3.5.2 Speed Ratio

The literature review on counter-rotating axial compressors in Section 2.4 indicated that the speed ratio affects the efficiency and stall margin and that both may be improved with the downstream rotor turning more slowly. In the present concept, one can see from Figure 3-15 that the rotating velocity of the downstream rotor (U_3) contributes to the relative velocity (W_3) (and relative inlet Mach number) of the incoming flow to this rotor. A lower rotational velocity of this rotor (U_3 to U_3') would reduce the relative incoming velocity (W_3 to W_3') and thus the strength of the shocks and associated losses mentioned in section 3.5.1, as well as the relative inlet flow angle to facilitate the rotor design. However, a lower rotational velocity (U_3') reduces the work done by the rotor (and thus its total pressure ratio) and addressing it would entail other inconveniences, as mentioned in section 3.5.1.

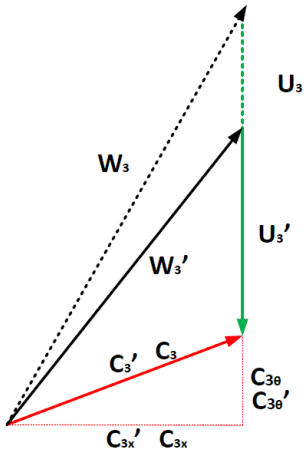

Figure 3-15 Effect of speed ratio reduction on velocity triangle at the inlet of axial rotor

3.5.3 Vaned Diffuser

The velocity triangles in Figure 3-12 indicates that the relative inlet Mach number to the axial rotor can also be reduced by decreasing the swirl of the incoming flow ($C_{3\theta}$ to $C_{3\theta}$' in Figure 3-16). This can be done by replacing the vaneless diffuser by a vaned diffuser. The resulting reduction in inlet relative Mach number and associated shock-related losses would be beneficial for efficiency, as well as the relative inlet flow angle to facilitate the rotor design. However, as shown in Figure 3-16, a reduction in inlet swirl reduces the work done on the flow by the axial rotor (by increasing $C_{1\theta}$ in equation (3.2)) and thus its total pressure rise. Moreover, the additional wetted surface (boundary layers) from the diffuser vanes will increase viscous losses,

possibly by a significant amount if boundary layer separation occurs due to the larger pressure gradient (more diffusion) in the diffuser.

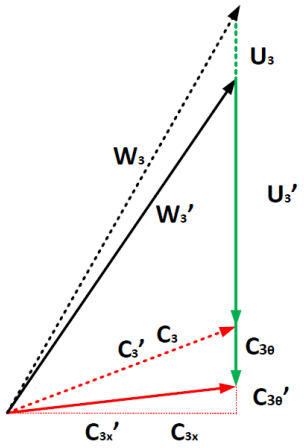

Figure 3-16 Effect of vaned diffuser on velocity triangle at the inlet of axial rotor

3.5.4 Blade Profile Modification

The literature in section 2.3 indicated that an un-cambered blade profile, such as that of Schreiber and Starken [22] (1992), can potentially reduce shock-related losses in supersonic axial compressor rotors by diffusing the flow through multiple lower-strength shocks. However, the design of such blade is more complicated as the geometry must be tailored for a particular set of local inlet condition to achieve the proper shock pattern.

3.6 Phase 4: Final Design

The evaluation of the design strategies from section 3.5 should lead to an improved design of the CRC compressor. This final design will be analyzed in detail both at design and off-design. Based on this assessment, strategies for further design improvements can be proposed.

The design point assessment consists of simulating the final CRC compressor configuration (in steady mode) and comparing it against the original configuration both in terms of integral performance to see if it better meets the total pressure ratio, polytropic efficiency and exit flow angle targets. The flow fields of the two designs are then compared to ensure that problematic items (flow separation, high inlet Mach number and shock structure) are resolved. Unsteady simulations are also carried out at design mass flow to ensure that the performance is not

noticeably affected by flow unsteadiness, namely from potential and wake interactions between adjacent blade rows.

The off-design assessment aims to compare the stall margin of the final CRC compressor design against that of the CC compressor, for which the stall point (last stable operating point) must be found. For each compressor geometry, this is done by first carrying out steady-state CFD simulations with incrementally decreasing the mass flow value until the convergence limit is achieved. The area-averaged static pressure at the exit of the computational domain for this solution is applied to the computational domain exit in unsteady simulations where this value is incrementally increased until the unsteady convergence limit is found. This simulation procedure is also applied to the stand-alone impeller to find its stall point. For the final CRC compressor, a simulation with the exit static pressure just slightly higher than the value at the convergence limit is carried out to simulate the initial "single passage" stall transient so that the instantaneous flow field can be analyzed for the cause of flow breakdown that leads to rotating stall.

The compressor characteristics (speedlines) are then plotted for the final CRC and CC compressors in terms of total pressure ratio and polytropic efficiency versus corrected mass flow ($\dot{m}_c$), as defined in equation (3.8), where the reference pressure and temperature are 1 atm and 288 K, respectively. For unsteady solutions, the values from the time-averaged flow-field are plotted. First, the speedlines allow to verify that the solution at design mass flow for the CRC and CC configurations corresponds to their respective peak efficiency. Second, a comparison of the unsteady and steady solutions of the CRC compressor at peak efficiency is made to assess the effect of flow unsteadiness on design-point performance. Finally, the stall points are compared. It must be noted that modal rotating stall inception requires the simulation of the full compression system (all stages combined) in a full-annulus setting. With the current single blade passage simulation of a single stage, the convergence limit represents flow breakdown associated with the spike stall inception initiated in the simulated stage. This flow breakdown is usually due to either tip clearance flow or boundary layer separation. The value of the stall margin (SM), as defined in equation (3.9), is calculated for the CRC and CC compressors and compared to see if the CRC compressor has a better stall margin than its conventional equivalent.

$$\dot{m}_c = \frac{\dot{m}\sqrt{T_{02}/T_{ref}}}{P_{02}/P_{ref}} \tag{3.8}$$

$$SM = \frac{\dot{m}_{c,design} - \dot{m}_{c,stall}}{\dot{m}_{c,design}} \tag{3.9}$$

To determine the source of stall for the CRC compressor, one first compares its stall point to that of the impeller on the speedlines. If the impeller stalls at a higher mass flow, then the source of stall is the impeller (and the axial rotor is actually helping to stabilize the impeller). However, if the impeller stalls at a lower mass flow than the CRC compressor, the axial rotor is the source of stall and the exact cause of stall should be investigated further to help improve its design in the future. In this case, the time-averaged flow field of the CRC compressor at the stall point is analyzed. The entropy contours at the blade tip of the axial rotor (similar to Figure 2-10b and Figure 2-12a) are plotted to assess the position of the incoming/tip clearance flow interface see if the first criterion proposed by Vo et al. [13] (Figure 2-1a) applies. If yes, this would indicate that tip clearance flow on the axial rotor is the cause of stall and strategies, such as casing treatment, must be applied to minimize its effects and increase the stall margin. However, if the incoming/tip clearance flow interface criterion is not satisfied, then the surface streamlines must be plotted for the axial rotor (and vaneless diffuser) at the near-stall and stall points, as well as at instantaneous point during the single-passage stall transient (flow breakdown), to see if there are any boundary layer separation regions and whether the extent of these regions grows as the mass flow is decreased toward and past the stall point. If this is the case, then boundary layer separation is the cause of stall and axial rotor (or vaneless space) design modifications are needed to improve stall margin.

CHAPTER 4 INITIAL DESIGN AND ASSESSMENT

This chapter presents the results of phases 1 and 2 of the research, namely the CC and first CRC compressor designs and their assessment.

4.1 Compressor Design

Figure 4-1 and Figure 4-2 provide the 3-D, front (axial) and side (meridional) views of the two designs along with their axial lengths and outer diameters. Both compressors share the same impeller (thus have the same inlet diameter) and have the same design corrected mass flow of 1.311 kg/s. The impeller has 21 blades without splitters and is complemented in the CC design by 21 fishtail diffuser pipes. In the CRC design, the diffuser is replaced by a vaneless diffuser and a (counter-rotating) axial rotor featuring 21 blades with a DCA profile. The CC compressor design falls exactly within its dimensional specifications. Moreover, one can see that the CRC configuration is much smaller in both radial and axial extents than the equivalent CC compressor.

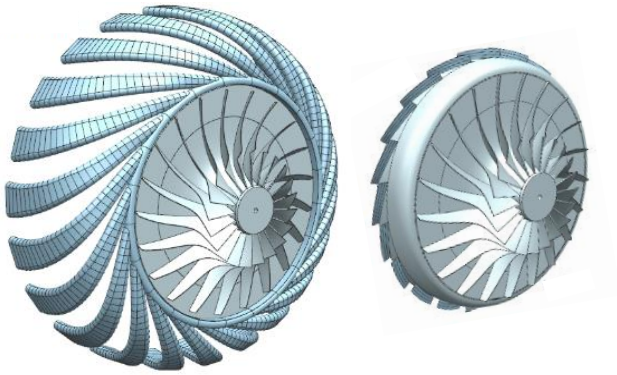

Figure 4-1 3-D view of CC compressor and first CRC compressor design

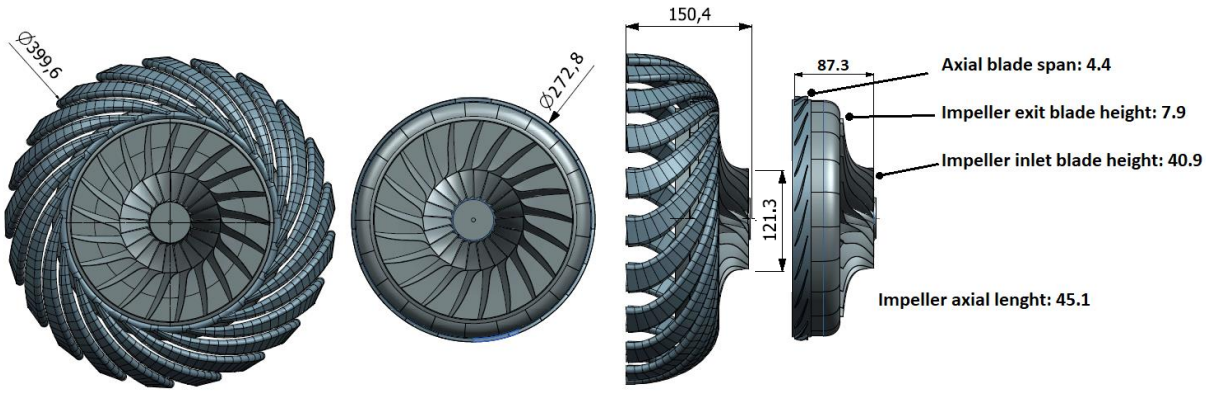

Figure 4-2 Final CC compressor and first CRC compressor design (all dimensions in mm)

4.2 CC Compressor Assessment

Table 4-1 compares the performance parameters of the CC compressor at design mass flow against the corresponding design targets from Table 3-1. One can see that the CC compressor meets its design-point performance specifications (including the impeller total pressure ratio and polytropic efficiency), as well as the requirement for axial exit flow within 0.6 degree.

Table 4-1 Performance of compressor designs

Parameter	**CC**	
	Target	**Final**
Total pressure ratio (*PR*)	5.10	5.09
Polytropic efficiency (η_{poly})	0.84-0.88	0.856
Exit flow angle (deg)	0	0.6
Impeller total pressure ratio	5.85-5.95	5.93
Impeller polytropic efficiency	0.92-0.94	0.938

For a more detail analysis of the flow field in the impeller, Figure 4-3 shows the surface streamlines on its suction and pressure sides. These streamlines do not indicate any flow reversal. Hence, there is no boundary layer separation on the impeller blades. As for the diffuser, the surface streamlines on the walls of the fishtail diffuser shown from two perspectives in Figure 4-4 indicate smooth flow in the streamwise direction without any sign of impending boundary layer separation. It is noted that the entrance angle of the pipe diffusers is set at the exit flow angle of the impeller (for the design mass flow), which is 78.13 degrees from the radial direction. This flow field analysis thus certifies that the final CC configuration is a good design and can serve as a reference for the CRC compressor design. Since the same impeller is used for the CRC compressor, any shortfall in the efficiency of the latter would be due to the vaneless diffuser and/or the axial rotor.

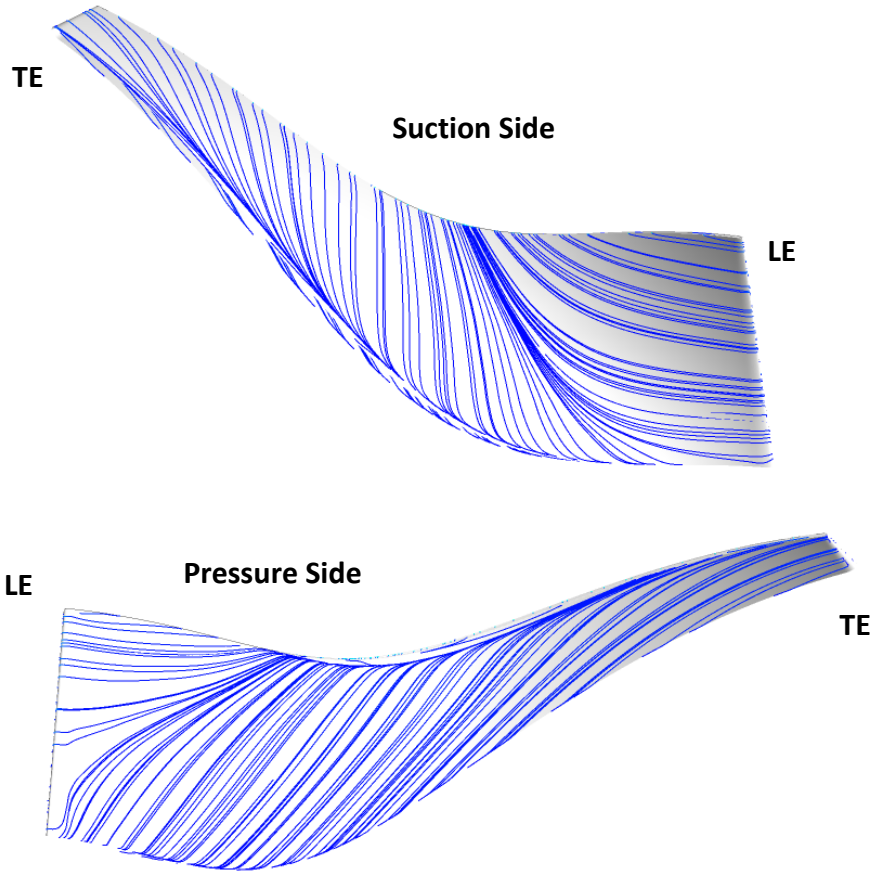

Figure 4-3 Surface streamlines on the pressure side and suction side of the impeller

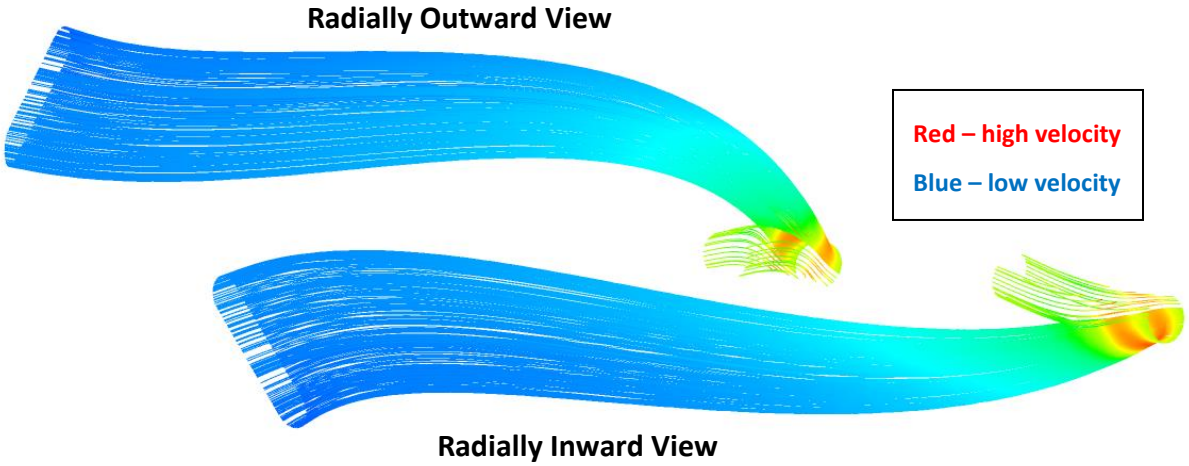

Figure 4-4 Surface streamlines for the fishtail diffuser

4.3 CRC Compressor Assessment

Table 4-2 compares the performance parameters of the CRC compressor at design mass flow against the corresponding design targets from Table 3-1. Note that the target polytropic efficiency is set to that of the CC compressor in Table 4-1, i.e. 85.6%. For this CRC compressor design, while the total pressure ratio exceeds the target, the polytropic compression efficiency is only 68.7%, which is far short of the target. Moreover, the exit flow is far from the axial direction with an average value of -47.64 degrees due to excessive flow turning by the axial rotor, which explains the high pressure ratio despite very low efficiency.

Table 4-2 Performance of compressor designs

Parameter	**CRC**	
	Target	**Final**
Total pressure ratio (*PR*)	9.20	9.55
Polytropic efficiency (η_{poly})	0.856	0.687
Exit flow angle (deg.)	0	-47.6

A more detailed analysis is required to uncover the sources of the efficiency deficit. It starts with Figure 4-5, which plots the evolution of the polytropic efficiency from the inlet to the exit of the CRC compressor. This plots comes from CFX-Post, which calculates the polytropic efficiency with mass-averaged total pressure and total temperature along the compressor gas path.. The horizontal axis represents the approximate streamwise location: the impeller subdomain goes from stations 0 to 1, the vaneless diffuser subdomain from 1 to 2 and the counter-rotating axial compressor subdomain from 2 to 3. The locations of the leading edge (LE) and trailing edge (TE) of the impeller (Imp) and axial rotor (R2) are indicated by vertical dashed lines. This plot indicates that the axial counter-rotating rotor is responsible for the largest loss in polytropic efficiency reduction (30%), while the vaneless diffuser causes only a drop in efficiency of about 3%. One can observe two regions of (counter-intuitive) polytropic efficiency increase located downstream of the impeller leading and trailing edges. These are artefacts due to local flow reversal in the tip region from impeller tip clearance flow, which corrupts the mass-averaging of total pressure and temperature used in calculating the polytropic efficiency. However, these

artefacts do not affect the main finding with regard to the central role of the axial rotor in the efficiency shortfall of the CRC compressor.

In parallel, the mass-averaged inlet and exit conditions of each component (Imp – impeller; VD - vaneless diffuser; R2 – axial rotor) are listed in Table 4-3. The data for the Imp_{out} and VD_{in} columns are taken on either side of the interface between the impeller and diffuser subdomains. On the other hand, VD_{out} is taken just upstream of the interface between the diffuser and axial rotor subdomains, but $R2_{in}$ are taken a short distance downstream of this interface just ahead of the rotor leading edge. *Alpha* and *Beta* are, respectively, the absolute and relative flow angles with respect to the meridional direction. The data show that the axial component of the inlet velocity (C_x) to the axial rotor is only 153.35 m/s (less than Mach 0.5), but that the relative inlet Mach number is 2.21, which is much higher than the typical value for high-speed axial compressors in the literature, which is between 1.3 to 1.6 [27]. Another interesting observation is that the total temperature rises slightly from VD_{out} to $R2_{in}$ due to flow turning by a shock extending upstream of the axial rotor leading edge.

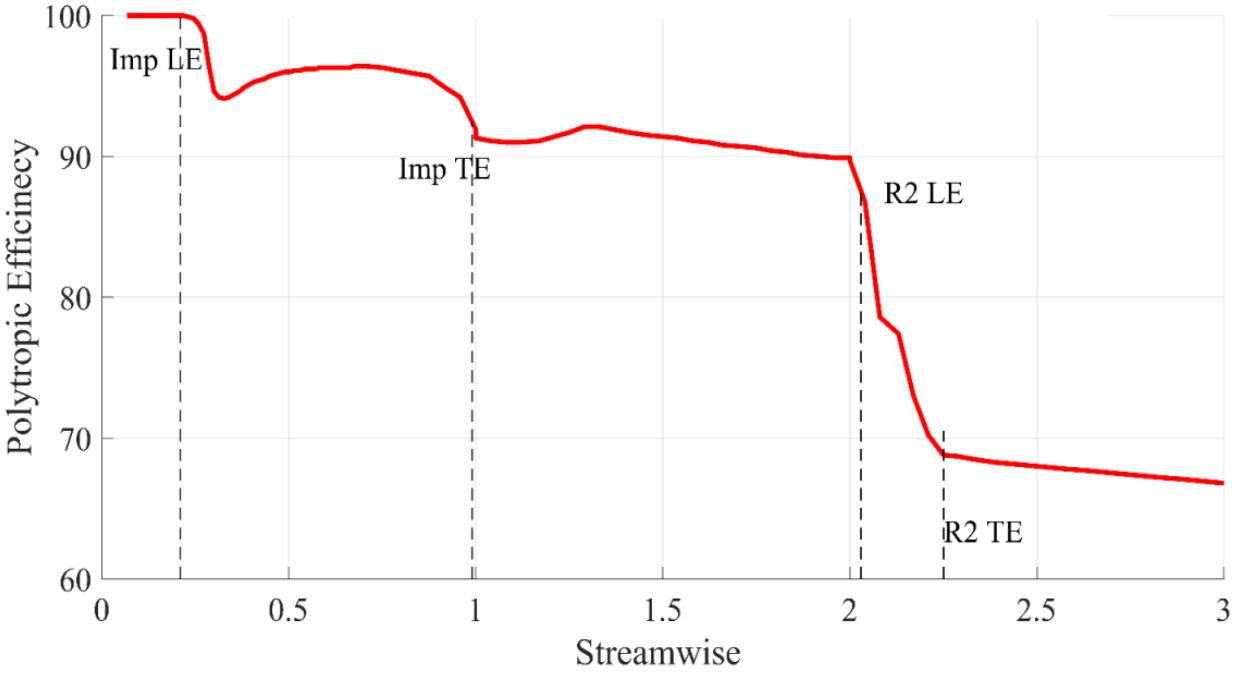

Figure 4-5 Variation of polytropic compression efficiency from inlet to outlet of CRC compressor

Table 4-3 Flow conditions across CRC compressor

	Imp_{out}	VD_{in}	VD_{out}	$R2_{in}$	$R2_{out}$
C_θ (m/s)	-444.6	-436.8	-384.2	-376.7	119.8
Cx (m/s)	149.7	62.8	140.5	153.4	95.8
C (m/s)	469.9	465.4	409.2	408.1	158.8
Alpha (deg)	-78.1	-76.8	-70.0	-67.7	-47.6
Wy (m/s)	161.6	-436.8	-384.2	-1036.1	-540.0
W (m/s)	219.4	465.4	409.2	1047.9	548.7
Beta (deg)	47.3	76.8	70.0	81.6	79.9
Pt (bar)	15.0	14.8	13.8	13.5	25.4
Tt (K)	643.82	644.16	644.11	647.07	974.51
Mach	1.01	1	0.86	0.86	0.25
$Mach_{rel}$	0.48	1	0.86	2.21	0.88

An investigation of the flow field helps to explain the causes of the polytropic efficiency drop downstream of the impeller in the CRC compressor. Figure 4-6 plots the flow vectors and Mach number contours in the vaneless diffuser while Figure 4-7 shows the relative streamlines at mid-span for the exducer (rear part of impeller), vaneless diffuser and axial rotor. These figures indicate that the flow is relatively well behaved in the vaneless diffuser with no sign of boundary layer separation on the hub. The small region of backflow at the inlet of the vaneless diffuser near the shroud is due to the tip clearance flow of the impeller. These observations explain the relatively low drop in polytropic efficiency across this component.

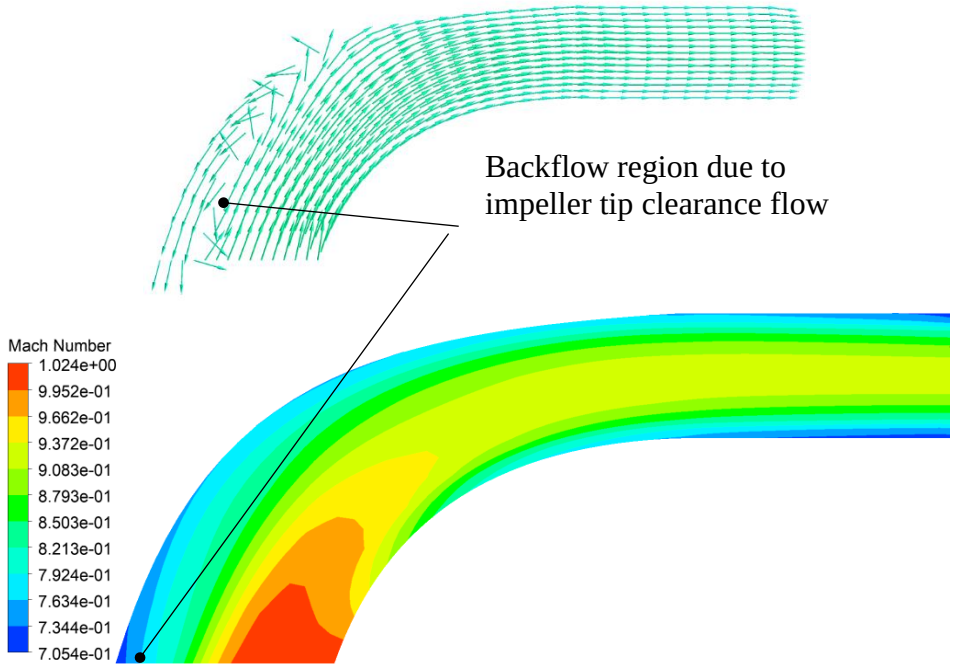

Figure 4-6 Flow vectors (top) and Mach number contours (bottom) at a meridional plane in the vaneless diffuser of the CRC compressor

On the other hand, Figure 4-7 also shows the presence of a large region of boundary layer separation over the suction side of the axial rotor. The shear stress contours (red for negative -upstream- shear stress) in Figure 4-8 and surface streamlines in Figure 4-9 for the axial rotor blade show that the suction side boundary layer separation covers about the 40% of the of the axial rotor blade and extends almost over the full span. Moreover, these two figures also show a boundary layer separation bubble on the lower half span of the pressure side just after the mid-chord. These separation regions constitute significant sources of loss from viscous shear, as evidenced by the high entropy region at their location seen in Figure 4-10, and are likely a significant factor in the large drop in polytropic efficiency across the axial rotor seen in Figure 4-5.

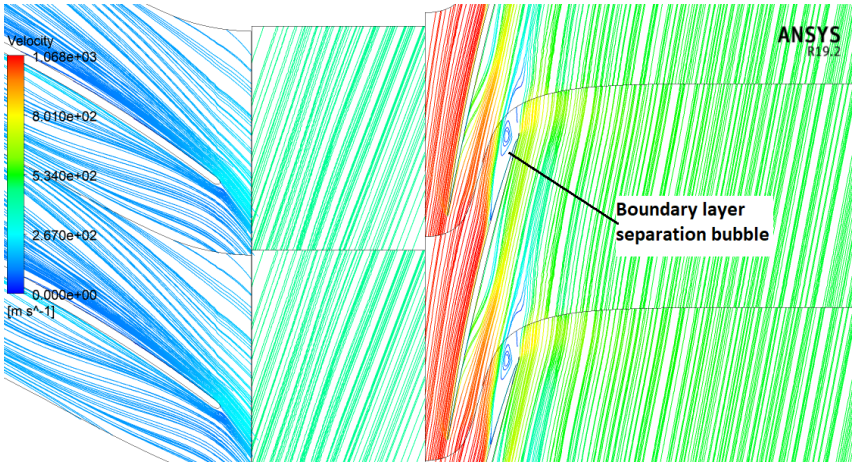

Figure 4-7 Relative streamlines at 50% span for the CRC compressor

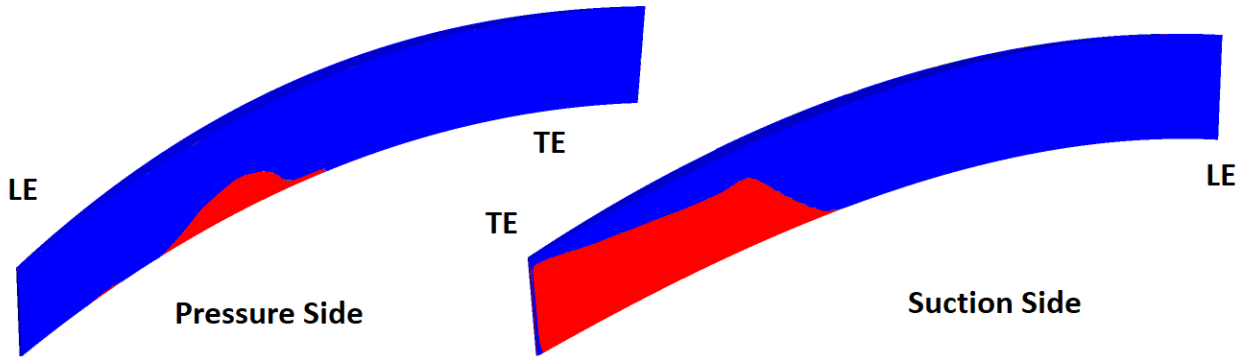

Figure 4-8 Shear stress contours for the CRC compressor axial rotor

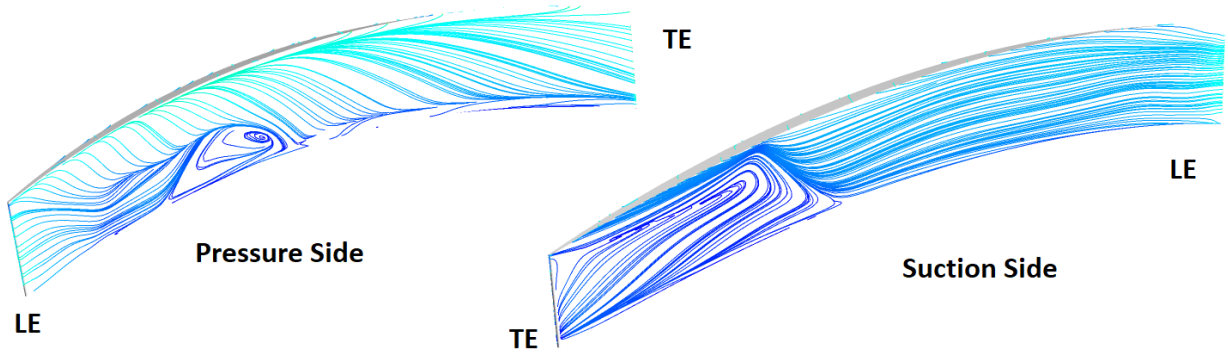

Figure 4-9 Surface streamlines for the pressure and suction sides of CRC compressor axial rotor

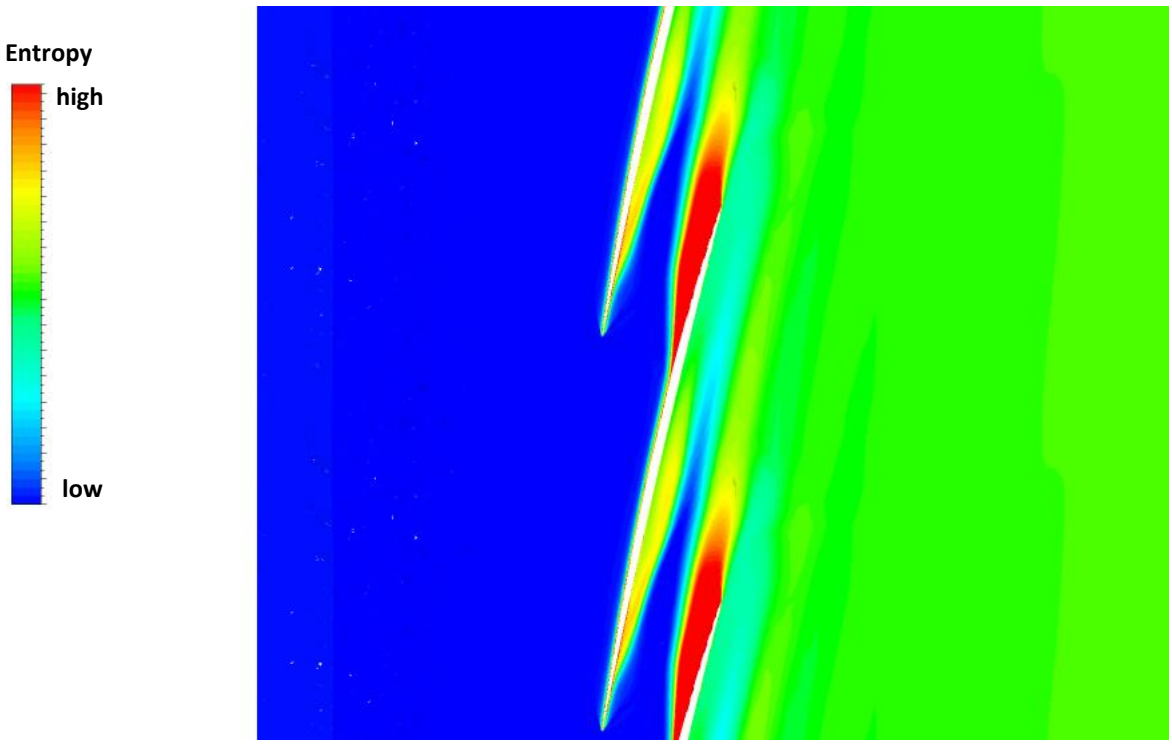

Figure 4-10 Entropy contours in axial rotor at mid-span

Another source of loss in the CRC axial rotor are the shocks. Figure 4-11 presents the contours of relative Mach number at the axial rotor mid span. Two oblique shocks emanate from the leading edge followed by another oblique shock emanating from the suction side aft of mid-chord.

The first main observation is that these shocks are much more oblique (smaller angle with respect to the blade) than those seen for the high-speed axial compressor rotors from the literature (Figure 2-3 through Figure 2-6), which is indicative of larger shock strength due to the higher relative inlet Mach number and higher shock losses.

Second, one can see that the strong shocks induce boundary layer separation on both suction and pressure side observed previously. (The boundary layer on the pressure side thickens after the leading edge shock and separates further along the chord). As such, the high relative inlet Mach number not only causes larger losses due to the stronger shocks themselves but also viscous losses from the boundary layer separation they induce.

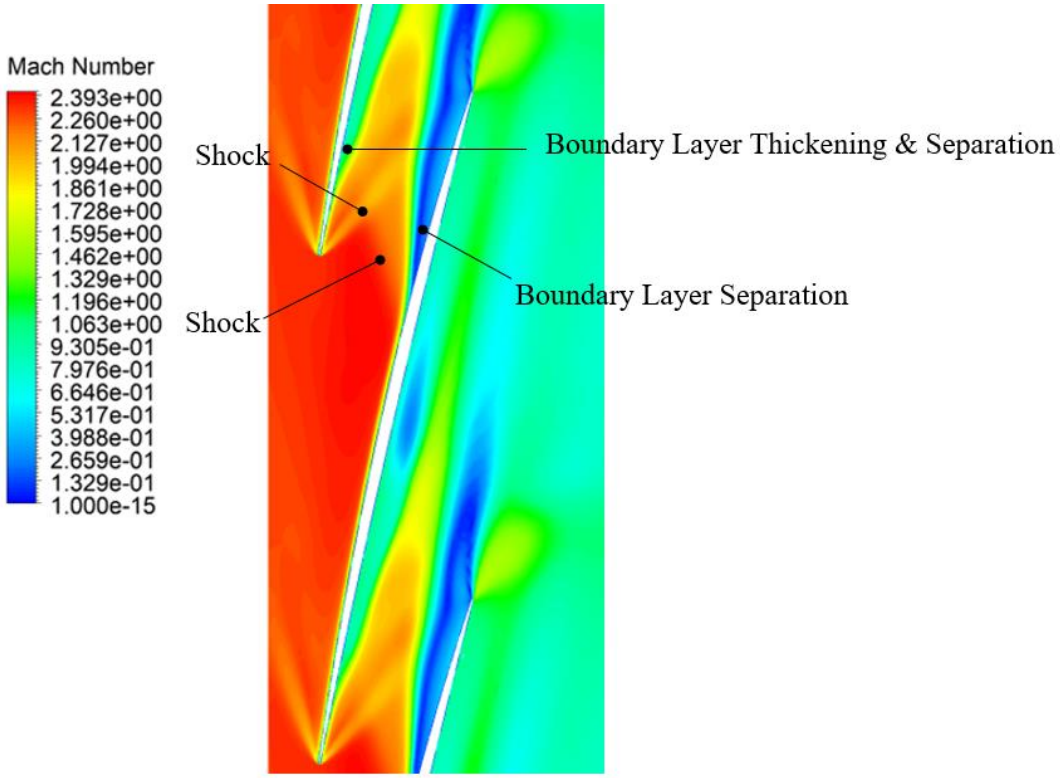

Figure 4-11 Relative Mach number contours at mid-span of axial rotor at design mass flow

Finally, with reference to the velocity triangle at the exit of the axial rotor (Station 4 in Figure 3-12), the stronger flow deceleration from the stronger shocks and flow separation result in a relative exit velocity (W_4) that is small enough such that its combination with the high blade speed (U_3) results in an absolute velocity (C_4) that is highly skewed in the direction of rotation as evidenced by the streamlines downstream of the axial rotor shown in Figure 4-12. As expected from a supersonic axial compressor rotor, most of the flow turning (in the stationary frame) comes from the decrease in relative velocity across the shocks rather than from blade camber as is the case in subsonic flows.

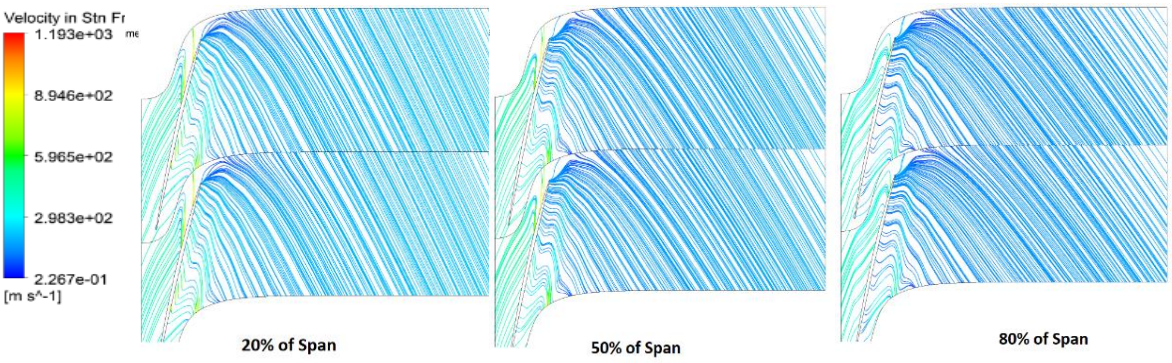

Figure 4-12 Streamlines in stationary frame across axial rotor

Another source of loss in the CRC axial rotor is the loss due to the tip clearance flow. The contours of entropy at the trailing edge of the axial rotor are shown in Figure 4-13. In this figure, the low-entropy (blue) region is the core flow. The tip clearance flow region as indicated on the figure is overwhelmed in both size (blockage effect) and entropy magnitude (loss) by the regions associated with the boundary layer flow separation on the blade suction and pressure side, which confine the core flow to a relatively small area.

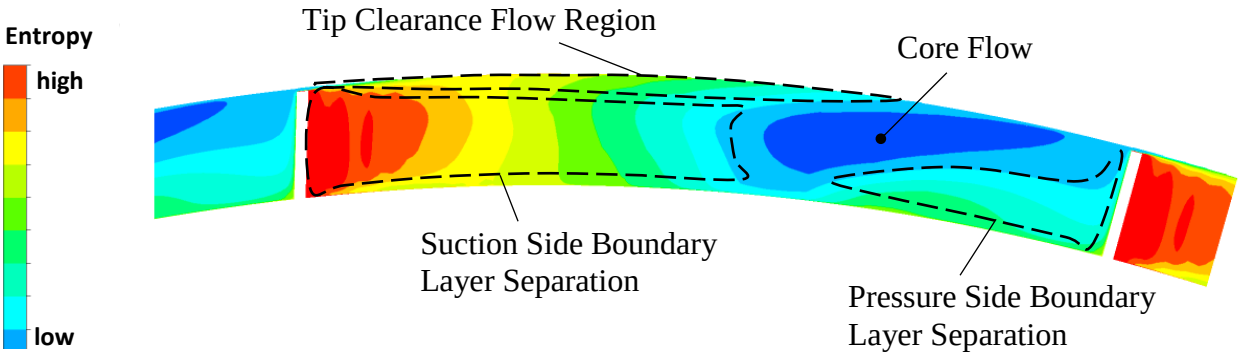

Figure 4-13 Static entropy contours at the trailing edge of axial rotor

Based on the flow field analysis above, one can infer that the leading sources of loss in the axial rotor would be viscous (boundary layer) loss and shock loss, and that the latter has a great influence on the former. The tip clearance flow is expected to have a more minor role in terms of

loss. To quantify the relative contribution of each of these sources of loss so as to determine which one can and should be addressed in priority, a procedure is devised based on single blade passage simulation of the axial rotor.

To do this, the counter-rotating rotor subdomain is extracted from the CRC compressor computational domain in Figure 3-9 to form a single computational domain. The total pressure, total temperature and velocity components of the flow at the exit of the vaneless diffuser subdomain is extracted from the CRC compressor simulation at the design mass flow and used as the inlet boundary conditions to the new isolated axial rotor computational domain. Three CFD simulations of this domain are carried out at the design mass flow.

The first simulation, referred to as the *Base Case*, is for the baseline setup with viscosity and nominal tip clearance. The converged solution is verified in performance and flow field to match the solution of the axial rotor in the CRC compressor simulation. The polytropic efficiency for the axial rotor, calculated from just upstream of the leading edge to just downstream of the leading edge, is 41.0%. In other words, the combine contributions of all sources of loss in the axial rotor should add up to 59.0% in polytropic efficiency deficit (since the no-loss case is at 100% polytropic efficiency).

The second simulation, referred to as the *Inviscid Case*, features a free-slip boundary condition on all solid surfaces to simulate inviscid walls. In this case, the polytropic efficiency of the axial rotor is 75.7%, which incorporates only loss across the shocks and loss from tip clearance flow. Therefore, the polytropic efficiency reduction due to viscous losses is obtained by subtracting the rotor polytropic efficiency of the *Base Case* from that of the *Inviscid Case* to arrive at a value of 34.7 %.

The third simulation, referred to as *No Tip Clearance Case*, features zero tip clearance. The polytropic efficiency reduction due to tip clearance can then be found by subtracting the rotor polytropic efficiency of the *Base Case* from the *No Tip Clearance Case*. Unfortunately, simulations below a tip clearance of 0.004 inch do not converge in this case possibly due to observed corner separation at the blade tip and/or mesh quality issues with ANSYS TurboGrid for very low tip clearance sizes. To remedy this situation, the rotor polytropic efficiency values for simulations carried out at tip clearances of 0.004, 0.006, 0.007 and 0.008 inch are used (along with that of the nominal case at 0.005 inch tip clearance) to fit a curve for extrapolating the rotor

polytropic efficiency value at zero tip clearance. As illustrated in Figure 4-14, this process yields a rotor polytropic efficiency at zero tip clearance of 46.7% from a fourth-order polynomial curve fit. Thus, the polytropic efficiency reduction due to tip clearance is estimated to 5.7%.

Finally, the reduction in axial rotor polytropic efficiency from shocks is estimated by subtracting the contributions from viscous losses and tip clearance from the total polytropic efficiency deficit (59.0%) to arrive at a value of 18.6%.

The contributions of the three sources to the polytropic efficiency deficit of the axial rotor are summarized in Table 4-4. Although the contribution of viscous losses is higher than that of shock loss, it is noted that a portion of the former (loss from boundary layer separation) is directly linked to the presence of shocks. Moreover, a simple calculation with equations (3.6) through (3.8) using the inlet total pressure and total temperatures at the inlet of the impeller and those at the inlet of the axial rotor (taken from the CFD simulation of the CRC compressor) indicates that the axial rotor requires a polytropic efficiency of 90.3% for the CRC compressor to meet the pressure ratio and polytropic efficiency targets in Table 3-1. This value is at the upper end of what can be achieved in high-speed axial compressor rotors [56].

In other words, the polytropic efficiency of the axial rotor in the current CRC compressor design must be increased by 90.3% - 41.0% = 49.3%. Taking into account the minor contribution of tip clearance loss in this case and the fact that basic viscous loss from (un-separated) boundary layers cannot be decreased without removing blades (decreasing wetted surfaces), the only option is to remove shock losses and viscous losses from boundary layer separation. This can be achieved by reducing the strength of the shocks. In addition to reducing loss, the lower change in relative flow velocity across the weaker shocks should reduce over-turning as seen in Figure 4-12 and bring the exit flow closer to the axial direction. Chapter 5 will assess design strategies proposed in section 3.5 to try to reduce shock strength.

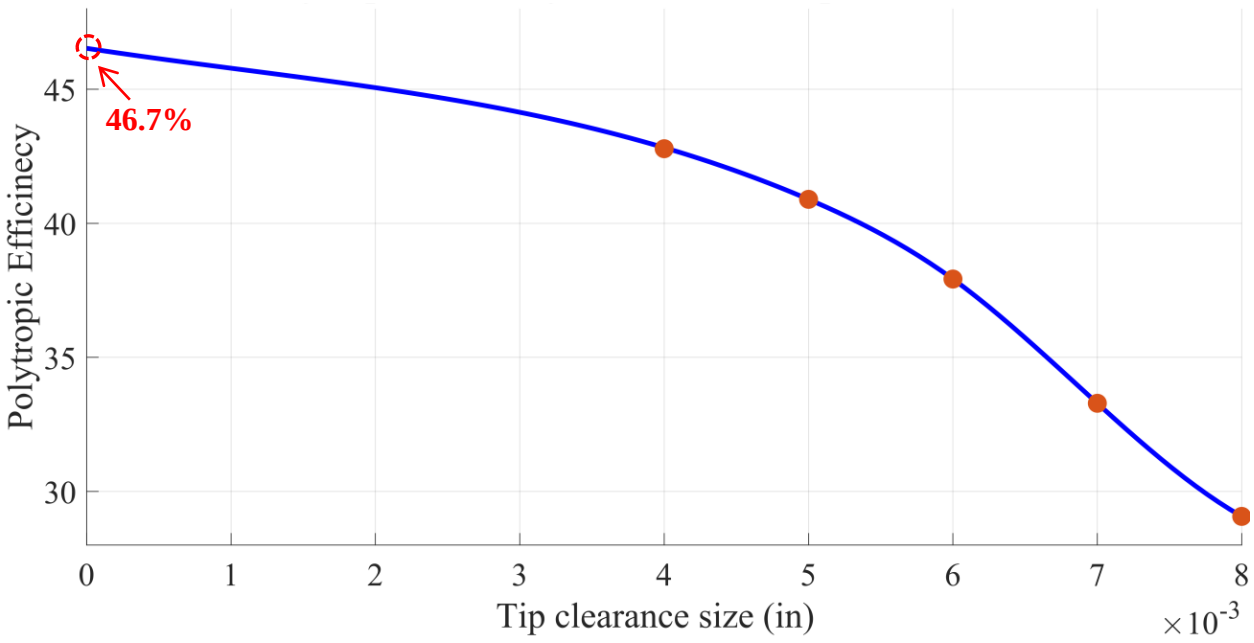

Figure 4-14 Variation of R2 polytropic efficiency with the size of tip clearance at the R2 shroud

Table 4-4 The contribution of different sources of loss to axial rotor polytropic efficiency reduction

Loss	**Contribution in polytropic efficiency (%)**
Viscosity	34.7
Shock Loss	18.6
Tip Clearance Size	5.7

CHAPTER 5 DESIGN IMPROVEMENT

This chapter assesses design strategies to reduce shock strength in the counter-rotating axial rotor to improve its design-point efficiency and by extension that of the CRC compressor. These strategies, introduced in section 3.5, involve reducing relative inlet Mach number through gas path modification, smaller speed ratio, using a vaned diffuser; and altering shock pattern in the axial rotor passage through blade profile modification. The CRC compressor design is updated after each assessment if the strategy is successful. As such, the gas path modification is evaluated first because the preference is to avoid reducing speed ratio as it decreases the work done and thus total pressure rise of the axial rotor. Conversely, the blade profile modification strategy is evaluated last because it is highly dependent on the inlet conditions to the axial rotor which would depend on the implementation of the other strategies. The evaluation of the four design improvement strategies is detailed in the sections below.

5.1 Gas Path Redesign

A new vaneless diffuser with the alternative gas path illustrated in Figure 3-13 is implemented as the stationary computational subdomain whose meridional view and mesh is shown in Figure 5-1. As the axial rotor would need to be redesigned for this gas path, this simulation is run without any axial rotor subdomain in order to assess the flow in the gas path and obtain the inlet flow conditions needed to revise the rotor design. A mass flow boundary condition is applied at the exit. As mentioned in Section 3.5.1, this alternative gas path aims to lower the axial velocity and blade tip rotational velocity in order to reduce the relative inlet Mach number of the axial rotor to about 1.6, as well as to increase the rotor blade span to reduce tip clearance flow effects. The mesh for the new subdomain is created with ICEM CFD and the mesh density is similar to that of the baseline vaneless diffuser. In this simulation, the mass flow rate for the outlet boundary condition is chosen.

Figure 5-2 presents contours of axial velocity for one of many iterations for the alternative vaneless diffuser depicted in Figure 3-13. The presence of regions of negative axial velocity (in blue) indicates a significant flow separation occurring on the hub at the potential location of the axial rotor, as confirmed by the flow vectors in Figure 5-3. The suppression of this region would entail extending the gas path which would increase wetted surface (higher viscous loss) as well as

compressor length and weight, negating one of the key advantages of the CRC compressor concept. None of the iterations have so far managed to remove the flow separation. Thus, this strategy is not pursued.

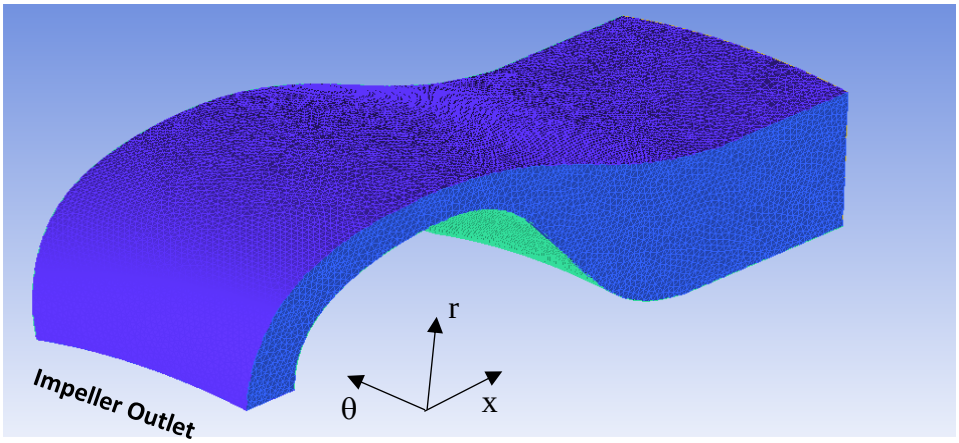

Figure 5-1 Computational subdomain and mesh for alternative vaneless diffuser used for CRC compressor

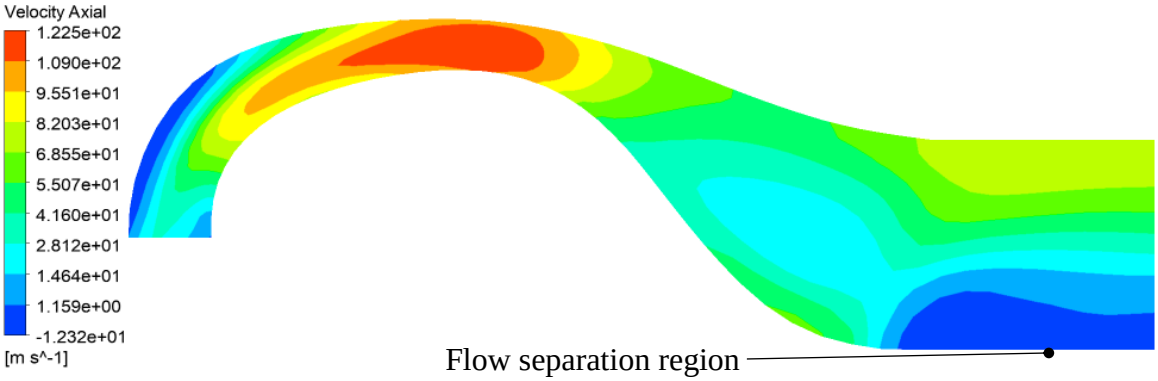

Figure 5-2 Axial velocity contours for alternative vaneless diffuser

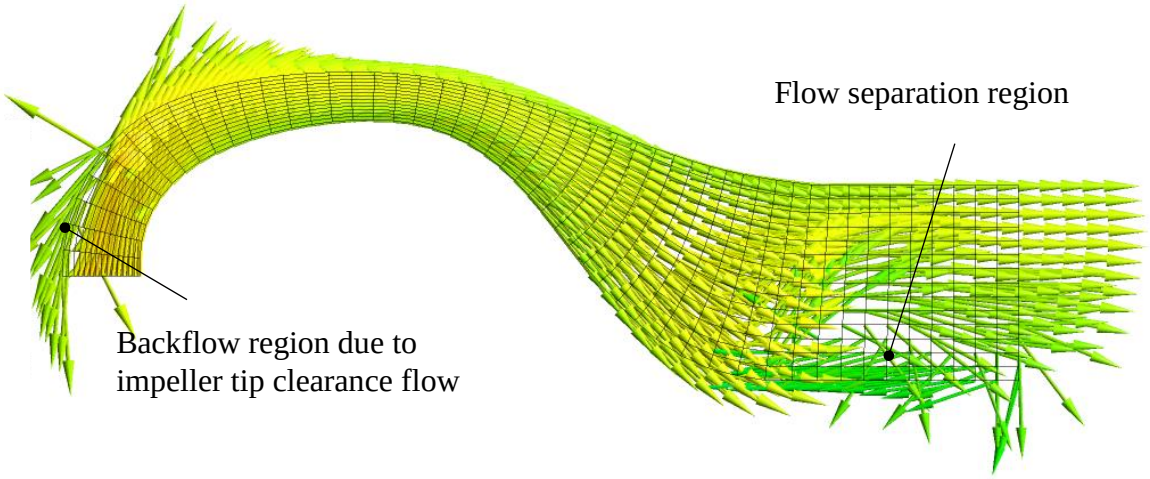

Figure 5-3 Velocity vectors for alternative vaneless diffuser

5.2 Speed Ratio

In the first CRC compressor design, the rotational speed of the axial rotor is the same as the centrifugal impeller (100% speed ratio) resulting in an inlet relative Mach number of about 2.2. CFD simulations of the CRC compressor are repeated for lower rotational speeds of the axial rotor to obtain the mass-averaged relative Mach number at the inlet of the axial rotor to confirm analytical predictions (from meanline analysis) and to determine loss in CRC compressor total pressure ratio (meanline analysis can only predict loss in total temperature rise). The results are reported in Table 5-1, which shows the decrease in the mass-averaged inlet relative Mach number with speed ratio. As the maximum inlet relative Mach number for high-speed axial compressor rotor in the literature is around 1.6 [27], the speed ratio of 60% is chosen for the final design so as not to sacrifice further work (thus total pressure rise) of the axial rotor by decreasing the speed ratio further. Figure 5-4 compares the spanwise distribution of relative Mach number at the axial rotor inlet for speed ratios of 60% and 100%, indicating a significant reduction in inlet Mach number to the axial rotor across the entire span. The corresponding CFD simulations show that the polytropic efficiency of the CRC compressor improves by only 3.45% while the pressure ratio decreases by 29.4%. An analysis of the flow field in Figure 5-5 and Figure 5-6 shows that flow separation is still present and that the shock pattern has not improved much from the original case in Figure 4-8 and Figure 4-10. Thus, the relative inlet Mach number needs to be decreased to an even lower value without further reducing the speed ratio. This can be done by converting the vaneless diffuser into a vaned diffuser to reduce flow swirl at the axial rotor inlet, as discussed in section 3.5.3. This strategy is evaluated in the next section.

Table 5-1 the effect of speed ratio on the inlet relative Mach number

Speed ratio (%)	**50**	**60**	**70**	**80**	**90**	**100**
R2 Rotational Speed (rpm)	23,473	28,168	32,862	37,557	42,251	46,946
Blade Tip Speed (m/s)	335.28	402.34	469.40	536.45	603.51	670.57
Inlet Relative Mach Number	1.520	1.663	1.807	1.951	2.095	2.219

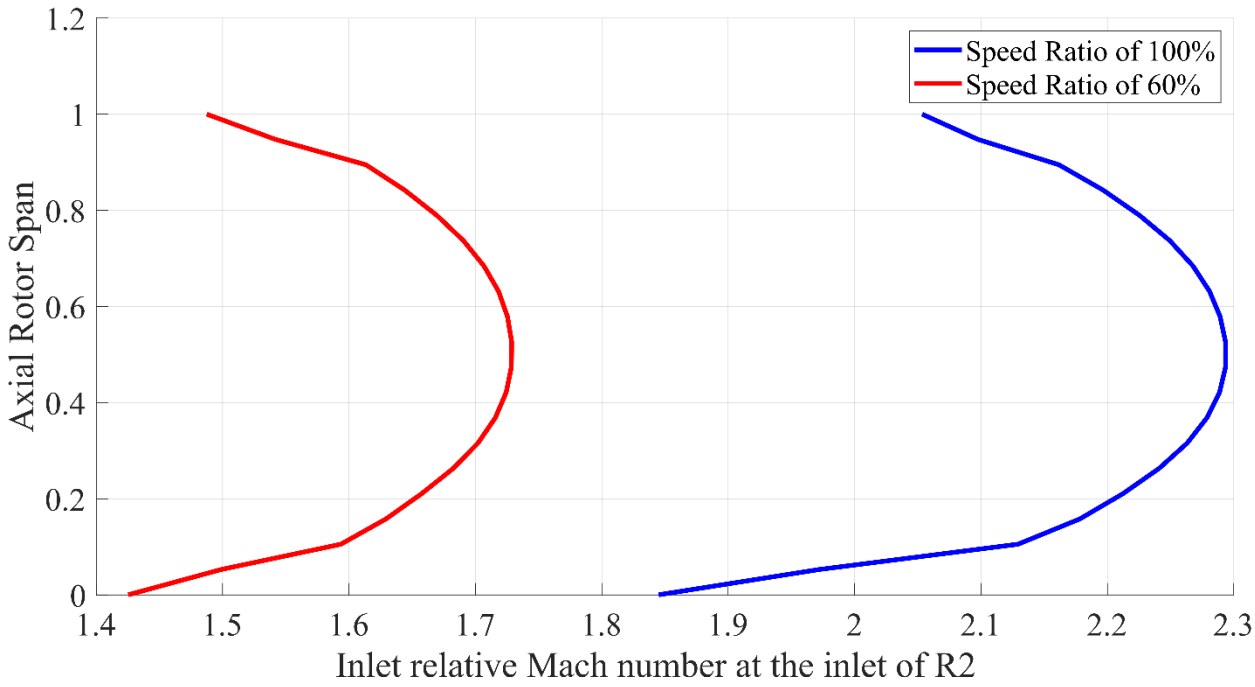

Figure 5-4 Spanwise distributions of relative inlet Mach number for axial rotor

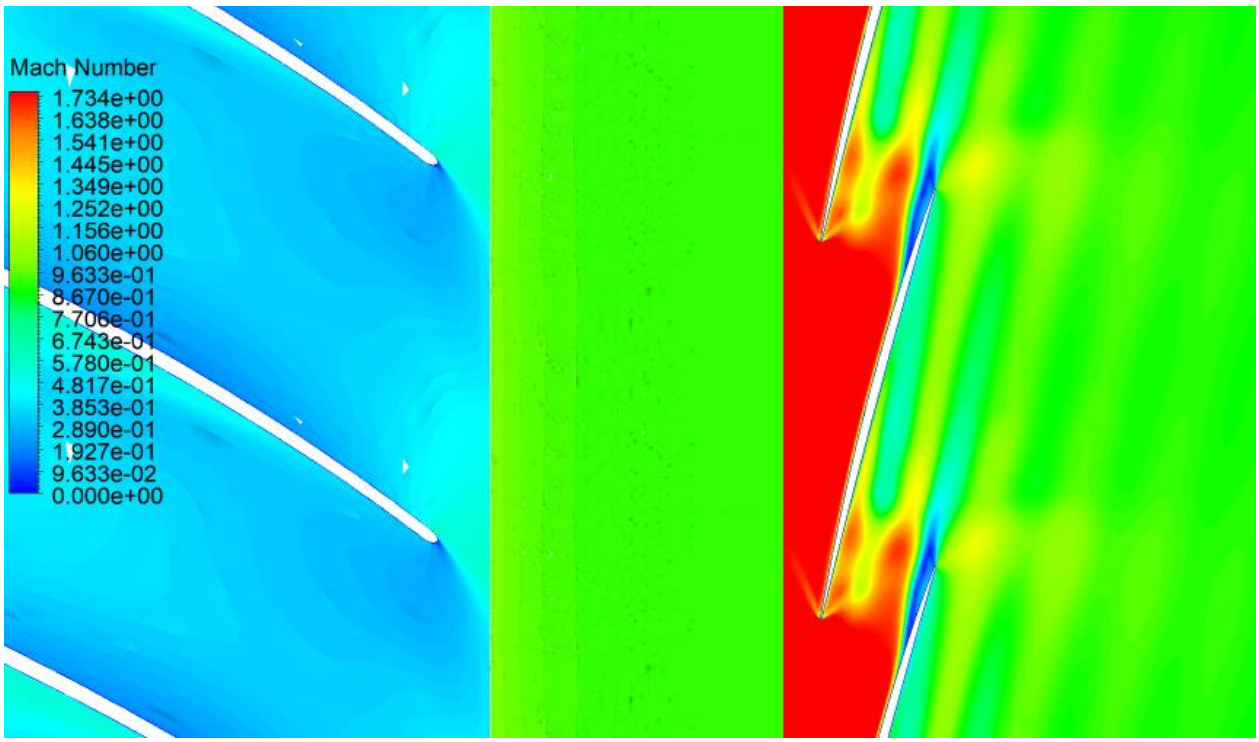

Figure 5-5 Relative Mach number contours at mid-span of axial rotor at 60% speed ratio

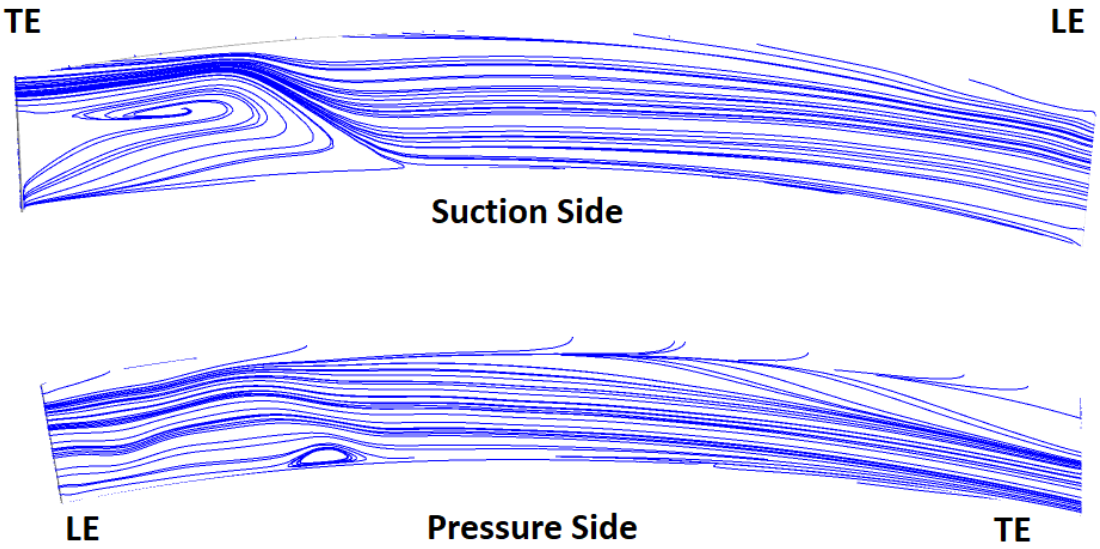

Figure 5-6 Surface streamlines for axial rotor at 60% speed ratio

5.3 Vaned Diffuser

A design of a vaned diffuser is carried out with the objective of bringing the inlet relative Mach number to the axial rotor down to about 1.2 where the shock strength (and losses) should be much lower. The addition of a preliminary stator vane design to the original vaneless diffuser results in a flow separation on the hub, as shown by flow vectors in Figure 5-7, due to the higher pressure gradient from the higher flow diffusion rate. Hence, the gas path has to be modified.

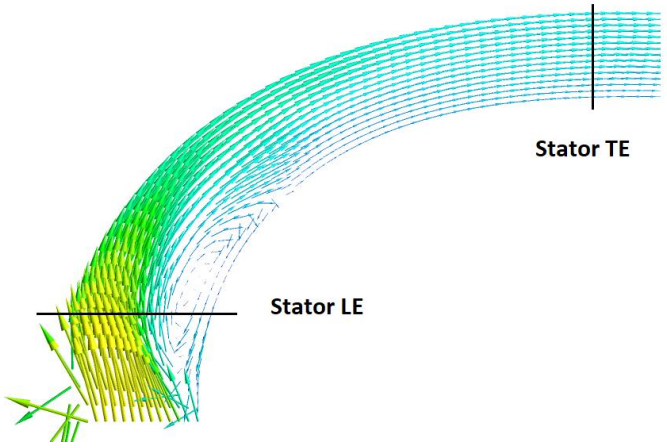

Figure 5-7 Flow separation during the design of stator vane

Given the coupling effect between the gas path and the stator vane geometry, the vaned diffuser design is parametrized in ANSYS BladeGen (see Appendix A). Figure 5-8 shows the meridional view of the vane diffuser with the control points for the gas path and locations of the stator vane leading edge and trailing edge. The other geometrical input parameters are the control points for the distributions of angle and circumferential location of the camberline from leading edge to trailing edge at the hub and shroud. Given the very low aspect ratio of the blade (short span and long chord), the blade are chosen to be thin with constant thickness and elliptical leading and trailing edges. The number of vanes are the same as the blade number for the impeller. The computational subdomain for the original vaneless diffuser is replaced with one for the vane diffuser, which features a structured mesh generated using ANSYS TurboGrid. The mesh study and selected mesh size are shown in appendix B. Hand iterations of the vane diffuser design are performed by modifying the above inputs in ANSYS BladeGen starting with the gas path geometries shown in Figure 5-9 then designing the stator vane for each, and performing corresponding CFD simulations for 60% speed ratio at design mass flow. The goal of this manual optimization is to obtain a diffuser design without flow separation which can bring an average inlet relative Mach number to the axial rotor at around 1.2.

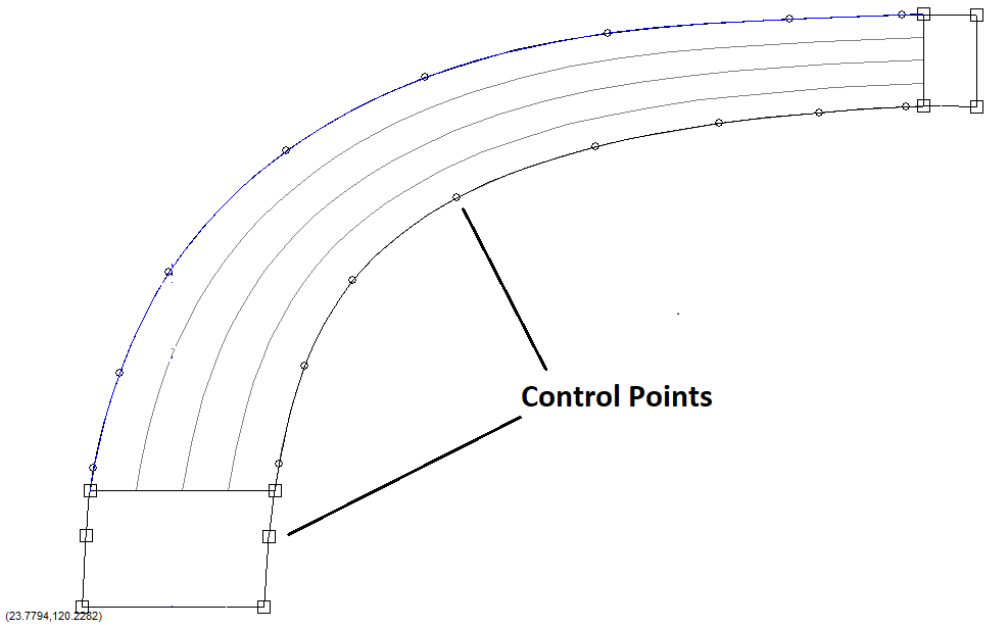

Figure 5-8 Gas path shape parametrization for vaned diffuser design

The final vaned diffuser design is shown in Figure 5-10, which reduces the average (absolute) circumferential flow angle at the inlet of the axial rotor from 69.8 to 58.3 degrees. The plots of

blade surface streamlines in Figure 5-11 indicate that the vaned diffuser is virtually free of flow separation except for a small region at the leading edge near the shroud due to backflow from the impeller tip clearance flow (see Figure 4-6). Figure 5-12 shows that the relative Mach number has been reduced to about 1.2 with a more uniform spanwise distribution compared to the case with the original vaneless diffuser at 60% speed ratio. Moreover, the relative average flow angle entering the axial rotor (thus the rotor leading edge blade angle) has been reduced from 81.05 degrees to 75.4 degrees, which helps the geometrical design of the axial rotor.

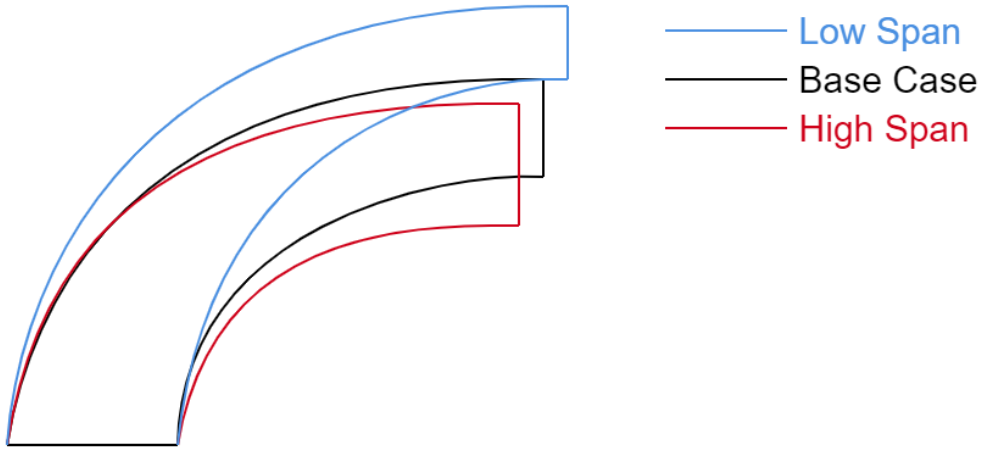

Figure 5-9 Hub and shroud curve modification for the design of vaned diffuser

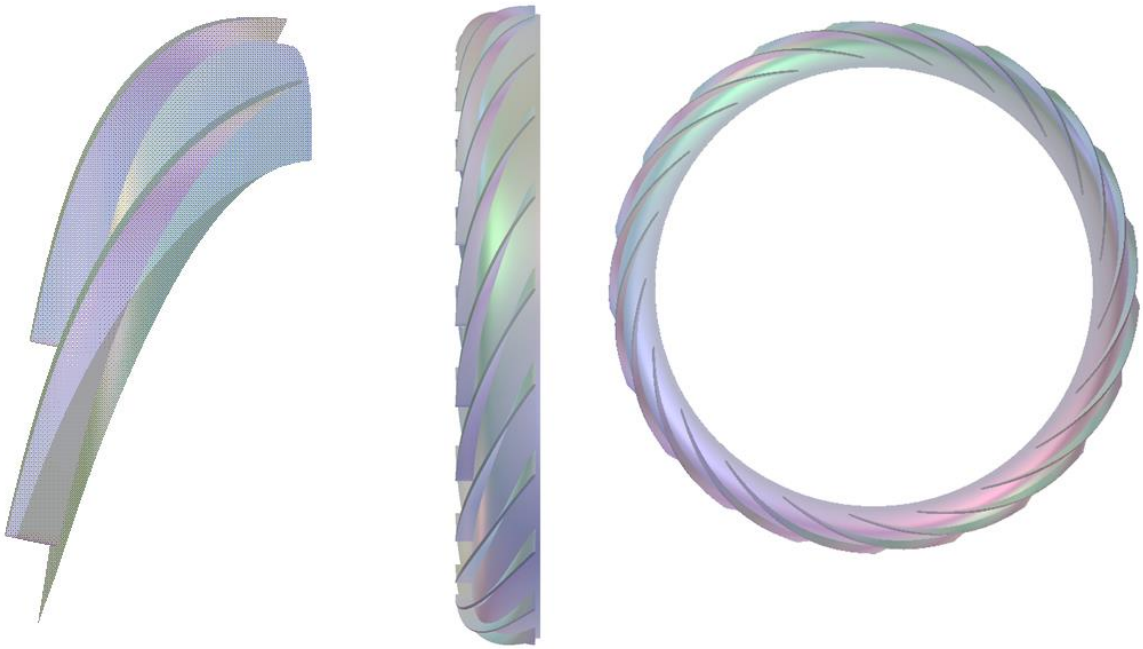

Figure 5-10 Different views of final vaned diffuser design

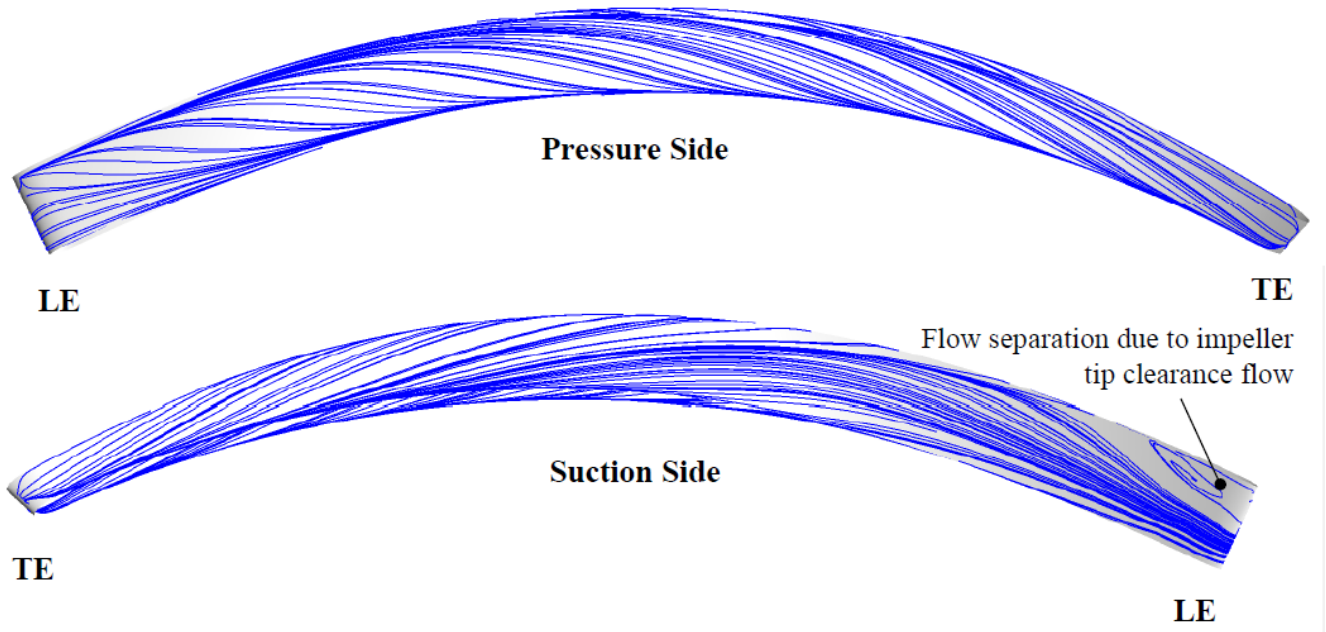

Figure 5-11 Surface streamlines for stator vane in final vaned diffuser design

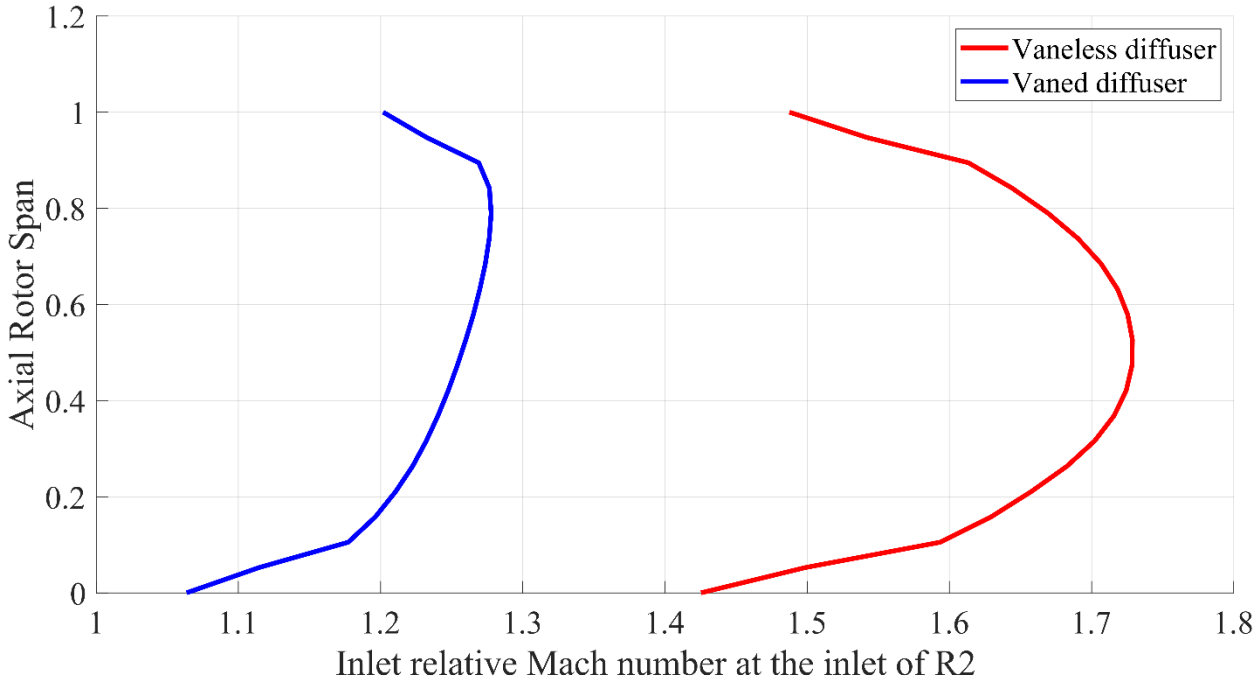

Figure 5-12 Effect of vaned diffuser on inlet relative Mach number of CRC compressor axial rotor at 60% speed ratio

However, the use of this vaned diffuser is also a compromise as it does presents some drawbacks. First, hub boundary layer separation was only achieved with the gas path with a larger radius and lower height (blue shape in Figure 5-9). As a result, the outer diameter of the CRC has increased from 272.8 mm to 291.6 mm and the gas path height (thus axial rotor blade span) has decreased from 4.4 to 4.0 mm. This is less desirable because of higher blade tip circumferential velocity (U_3' in figure 3-12) and lower axial rotor span (higher relative tip clearance size). Second, the vaned diffuser increases wetted surfaces and thus viscous loss. Table 5-2 indicates that the vaned diffuser adds over 8% in total pressure loss and cause 4.7% drop in polytropic efficiency (calculated from impeller inlet to axial rotor inlet), which must be compensated by additional gain in the axial rotor efficiency to be worthwhile.

Table 5-2 Performance of vaned diffuser versus vaneless diffuser

	P_T,out/ P_T,in	$\eta_{poly}(excluding\ axial\ rotor)$
Vaneless diffuser	0.93	90.0
Vaned diffuser	0.90	85.3

5.4 Blade Profile Modification

The high flow separation and loss from the original axial rotor observed in section 4.3 indicate that the DCA profile is not suitable for this application, To further confirm this conclusion, a revised axial rotor with the DCA profile is designed for the new inlet conditions produced with the vaned diffuser at 60% speed ratio. CFD simulations of this profile fails to converge due large flow separation inside the blade passage.

Since the literature review points to un-cambered rotor blade profiles as more effective for supersonic applications, a manual iteration process to design the axial rotor using un-cambered profiles for is carried out. For each design iteration, the blade is generated with ANSYS BladeGen (see Appendix A) by defining blade profiles at three span locations (hub, mid-span and tip) using the local relative inlet flow conditions obtained from CFD simulations. The blade profiles are updated by modifying the distribution of blade angles and thickness from leading edge to trailing edge and chord length (thus solidity) until CFD simulations of the CRC

compressor show the desired shock pattern and minimal boundary layer separation in the axial rotor and reasonable CRC compressor polytropic efficiency.

Figure 5-13 shows the first iteration of the new profile, which is characterized by near-zero camber on the upstream part and small camber on the downstream section of the chord. Following CFD simulations, Figure 5-14 and Figure 5-15 presents the associated contours of inlet relative Mach number and streamlines, respectively, at mid-span. The results show a significantly improved flow field compared to the previous blade profiles (Figure 4-12 and Figure 5-5) with less oblique (weaker) shocks, subsonic exit relative flow and absence of boundary separation (at least at mid-span). This is reflected in better CRC compressor performance with a polytropic efficiency of 75.5%. However, there is still overturning of the flow by the axial rotor in the stationary frame, giving a mass-averaged exit flow angle of -72.05 degrees such that the total pressure ratio is 9.11 (close to the target) despite a speed ratio of only 60%. This profile is iterated upon to further improve the CRC compressor's polytropic efficiency while bringing the exit flow closer to the axial direction. The final blade profile is shown in Figure 5-16 and, along with the original impeller, the final vaned diffuser in Figure 5-10 and a speed ratio of 60% constitute the revised design of CRC compressor. The details and assessment of this new CRC compressor design will be presented in Chapter 6.

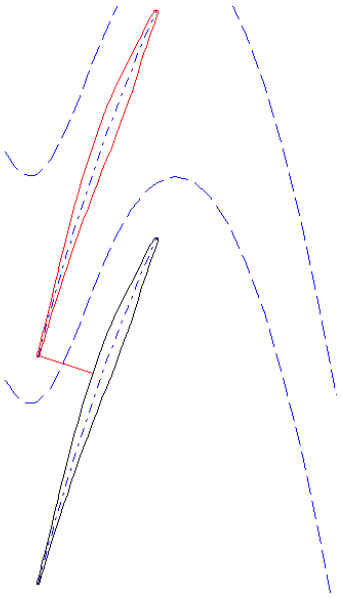

Figure 5-13 First iteration of un-cambered blade profile for axial rotor

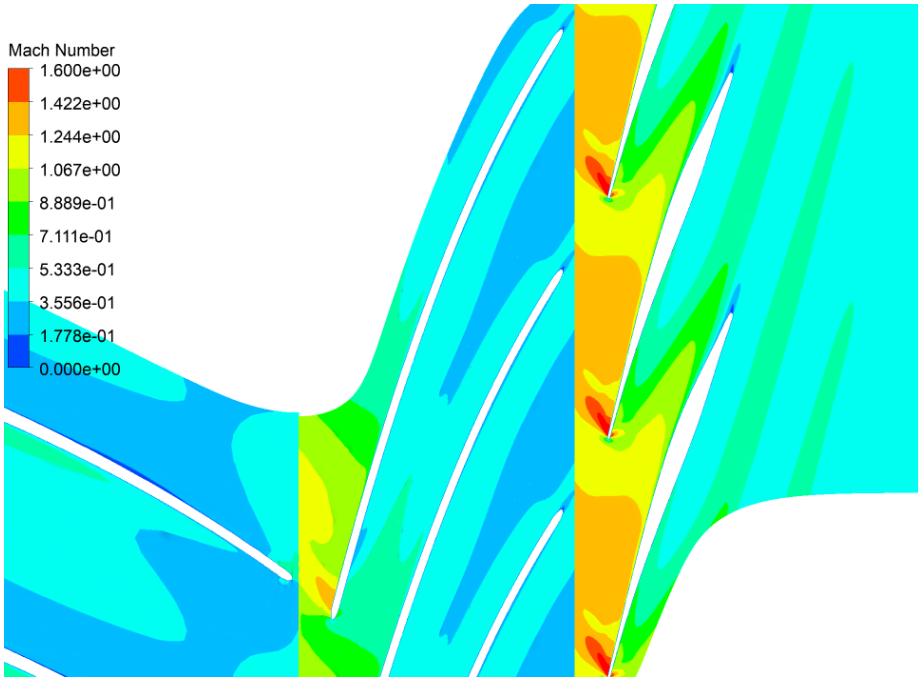

Figure 5-14 Relative inlet Mach number contours at mid-span for CRC compressor axial rotor with first iteration of un-cambered blade profile

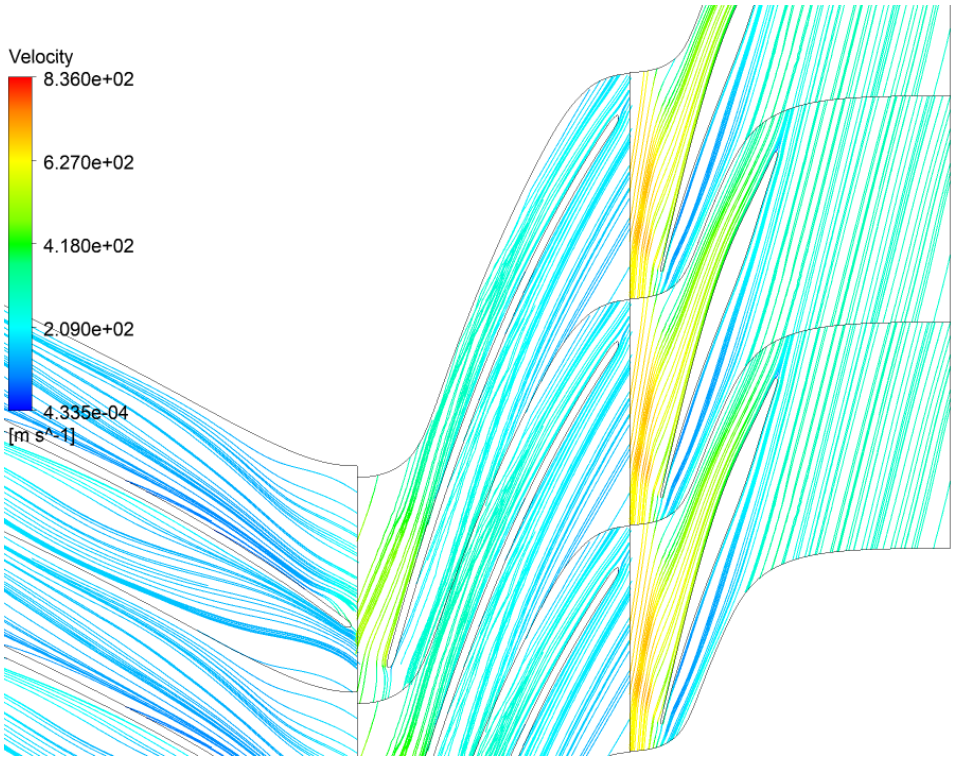

Figure 5-15 Relative streamlines at mid-span for CRC compressor axial rotor with first iteration of un-cambered blade profile

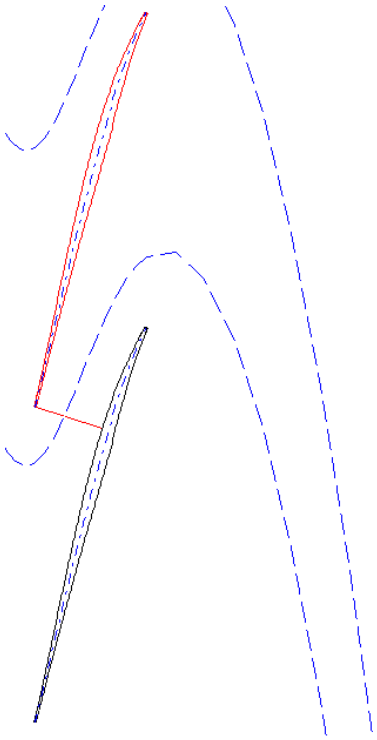

Figure 5-16 Final iteration of un-cambered profile for axial rotor

CHAPTER 6 FINAL DESIGN AND ASSESSMENT

This chapter presents the results from the assessment of new CRC compressor design resulting from applying the selected design improvement strategies in Chapter 5, both at design point for performance evaluation and off-design for stall margin and determination of the cause of stall. This assessment will lead to proposals for further design improvements.

6.1 New CRC Compressor Design

Figure 6-1 and Figure 6-2 give a visual comparison of the new CRC compressor design with the reference CC compressor design. Relative to the original CRC compressor design, the new design features a vaned diffuser that is larger in diameter and longer in axial extent than the original vaneless diffuser. These features result is a 10% lower blade span for the downstream axial rotor and a slightly larger CRC compressor (increase of 6.9% in diameter and 13.5% in axial extent), but which still remains noticeably smaller in outer diameter and axial extent than the equivalent CC compressor. The axial rotor of the new CRC compressor design has the same number of blades, blade chord and tip clearance (0.005 inch) as the original axial rotor but rotates at 60% of the original speed, i.e. at 28,168 rpm.

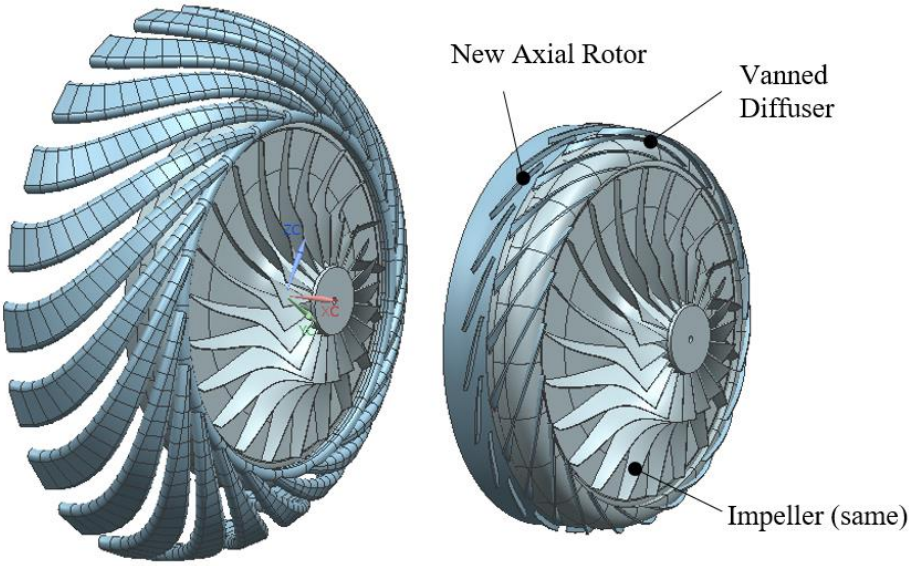

Figure 6-1 3D view of CC compressor (left) and new CRC compressor (right)

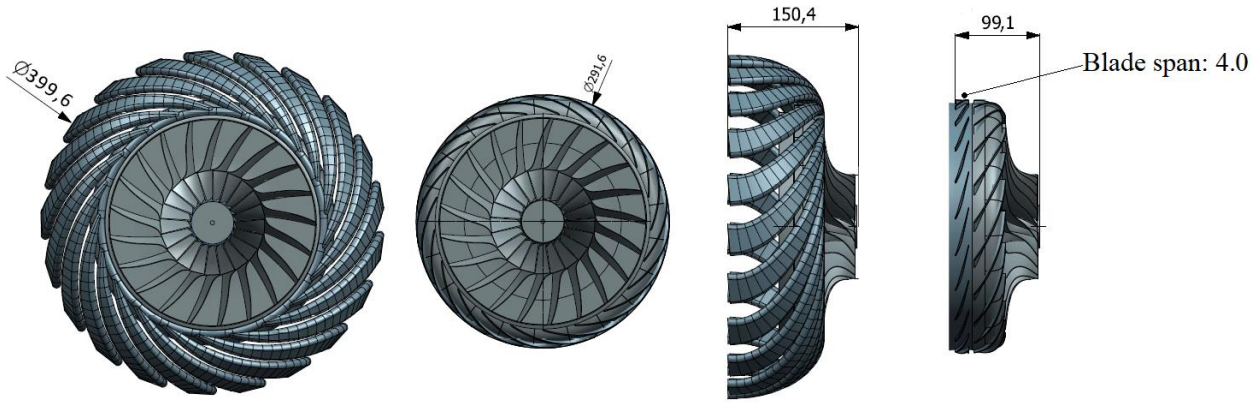

Figure 6-2 Axial and meridional views of CC compressor and new CRC compressor (all dimensions in mm)

6.2 Design Point Performance

Starting with an integral analysis, the performance of the new CRC compressor at the design mass flow is reported in Table 6-1. These results indicate that, compared to the original design, the new CRC compressor design comes much closer to the target polytropic efficiency, recovering over two-third of the original shortfall. Figure 6-3 compares the evolution of the polytropic efficiency across each of the two designs. The data shows that the drop in polytropic efficiency from the impeller exit to the entrance of the axial rotor is slightly larger for the new CRC compressor design due to higher losses in vane diffuser relative to the original vaneless diffuser as discussed in Section 5.3. However, this effect is largely compensated by the much smaller drop in polytropic efficiency across the new axial rotor relative to the original design. The polytropic efficiency of the new axial rotor is 58.5% compared to 41.0% for the original design. However, this is still well below the normal range of 80-90% for high-speed axial compressor rotors [56]. The reasons will be elucidated with analysis of the flow field.

Table 6-1 Performance of CRC compressor designs

Parameter	**CRC**		
	Target	**Original Design**	**New Design**
Total pressure ratio (*PR*)	9.20	9.55	6.97
Polytropic efficiency (η_{poly})	0.856	0.687	0.804
Exit flow angle (deg.)	0	-47.6	-1.6

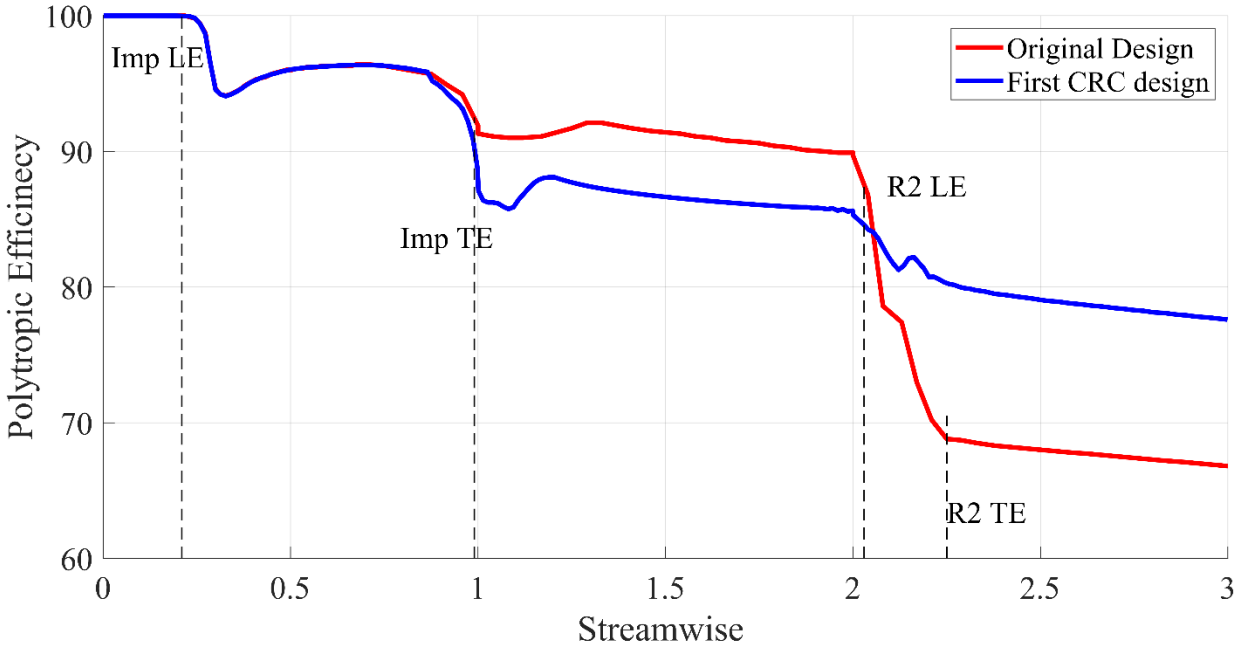

Figure 6-3 Variation of polytropic efficiency from the inlet to the outlet of the CRC compressors

Another improvement of the new CRC compressor design is a more axial exit flow, as evidenced in Figure 6-4 which shows the exit streamlines in stationary frame at different spans, and a mass-averaged exit flow angle in Table 6-1 that is much closer to zero than for the original CRC compressor design.

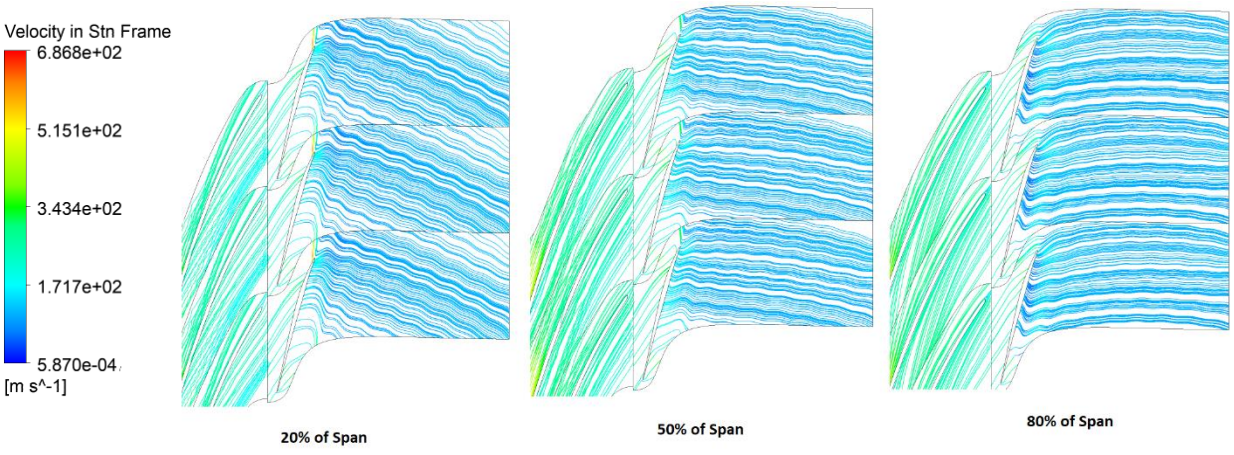

Figure 6-4 Streamlines in stationary frame across new axial rotor

On the other hand, Table 6-1 also indicates that while the original CRC compressor exceeds the target total pressure ratio, the new CRC compressor design falls far short of the target. Instead of giving the same total pressure rise as the impeller (to reach the target total pressure ratio for the

CRC compressor), the new axial only provides 46% of it. The total pressure rise deficit of the new axial rotor versus that of the initial design and the target can largely be explained through equation (3.2) (Euler's turbine equation) applied to the impeller and the counter-rotating axial rotor in the form of equations (6.1) and (6.2), where the left side (c_p*total temperature rise) represents the work done on the air (per unit mass) by the impeller (w_{imp}) or the axial rotor (w_{R2}). Referring to Figure 3-12, Stations 1 and 2 represent the inlet and exit of the impeller, while stations 3 and 4 are the inlet and exit of the counter-rotating axial rotor. The rotational velocity and local radius are denoted by ω and r.

$$(w_{imp} =)\ c_p(T_{02} - T_{01}) = \omega_{imp}(r_2 C_{2\theta} - r_1 C_{1\theta}) \tag{6.1}$$

$$(w_{R2} =)\ c_p(T_{04} - T_{03}) = -\omega_{R2}(r_4 C_{4\theta} - r_3 C_{3\theta}) \tag{6.2}$$

It must be noted that $r_4 = r_3$ due to the design choice of constant hub/shroud radii for the current axial rotor, and that $r_3 C_{3\theta} = r_2 C_{2\theta}$ across the vaneless diffuser from conservation of angular momentum. In the ideal (target) case, axial inlet and exit flow implies that $C_{1\theta} = C_{4\theta} = 0$ and a speed ratio of 100% means that $\omega_{R2} = \omega_{imp}$. Equations (6.1) and (6.2) thus simplify to equation (6.3) which indicates that the axial rotor does the same amount of work (same total temperature rise) on the flow as the impeller and thus should give similar total pressure rise.

$$w_{R2} = -\omega_{imp}(-r_2 C_{2\theta}) \quad = \quad \omega_{imp}(r_2 C_{2\theta}) = w_{imp} \tag{6.3}$$

For the original CRC compressor design, the axial rotor over-turns the flow in the stationary frame past the axial direction (see Figure 4-12) such that $C_{4\theta}$ has a negative value and can be denoted as $-|C_{4\theta}|$. Equations (6.1) and (6.2) thus simplify to equation (6.4), indicating that the axial rotor does more work than the impeller. This explains why the original axial rotor has higher total pressure rise than the impeller despite its low efficiency.

$$w_{R2} = -\omega_{imp}(-r_4|C_{4\theta}| - r_2 C_{2\theta}) \quad > \quad \omega_{imp}(r_2 C_{2\theta}) = w_{imp} \tag{6.4}$$

Lastly, in the case of the new CRC compressor, $\omega_{R2} = 0.6 * \omega_{imp}$ ($< \omega_{imp}$) due to the 60% speed ratio, and $r_3C_{3\theta} < r_2C_{2\theta}$ because the vaned diffuser decreases the swirl C_θ faster for the same radius change than a vaneless diffuser and $C_{4\theta} \approx 0$ from the almost axial exit flow. Thus, equations (6.1) and (6.2) simplify to equation (6.5), which shows that this axial rotor does lower than 60% of the work on the impeller (due to $r_3C_{3\theta} < r_2C_{2\theta}$) and generally explains why its total pressure rise is about 46% of that of the impeller. The only way to increase the total pressure rise with this configuration is to make the axial rotor overturn the exit flow in the stationary frame past the axial direction ($C_{4\theta} < 0$) which would result in equation (6.6) where the value of the term $r_4|C_{4\theta}|$ can be set so that the left hand side equals the right hand side. This will be shown in section 6.4.1.

$$w_{R2} = -0.6 * \omega_{imp}(-r_3C_{3\theta}) \quad < \quad \omega_{imp}(r_2C_{2\theta}) = w_{imp} \tag{6.5}$$

$$w_{R2} = -0.6 * \omega_{imp}(-r_4|C_{4\theta}| - r_3C_{3\theta}) \quad \equiv \quad \omega_{imp}(r_2C_{2\theta}) = w_{imp} \tag{6.6}$$

A flow field analysis can be done to investigate the source of the improved, but still low efficiency of the new axial rotor design in order to propose corrective design strategies. Figure 6-5 compares the relative Mach number contours at mid-span of the new versus original axial rotor. One can observe that the inlet relative Mach number is much lower for the new design relative to the original design, and that the shock pattern for the new rotor closely resembles those of the literature, in particular those in Figure 2-3, Figure 2-5 and Figure 2-6. It features an oblique shock emanating from the leading edge (which is less oblique, i.e. weaker than the corresponding shock on the original axial rotor) followed by a near-normal second passage shock downstream. This pattern of weaker shocks should contribute to improve the efficiency of the new axial rotor. Furthermore, a comparison of relative streamlines at mid-span in Figure 6-6 indicates that the separation region on the suction side is greatly reduced in the new axial rotor. This is confirmed by a comparison of the surface streamlines contours for the new axial rotor in Figure 6-7 compared with that of the original design in Figure 4-9, which shows the almost-full span flow separation region in the aft 40% chord on the suction side has been shrunk to a small triangular region covering the aft 15% at hub and reaching about 70% span at its most outer region. This smaller separation region is also visible at mid-span in Figure 6-5 as the smaller low Mach (dark

blue) region in the new design that lies immediately downstream of the second passage shock which likely induces the boundary layer separation. Moreover, Figure 6-7 also shows that the boundary layer separation on the lower span of the pressure side in Figure 4-9 has disappeared in the new axial rotor.

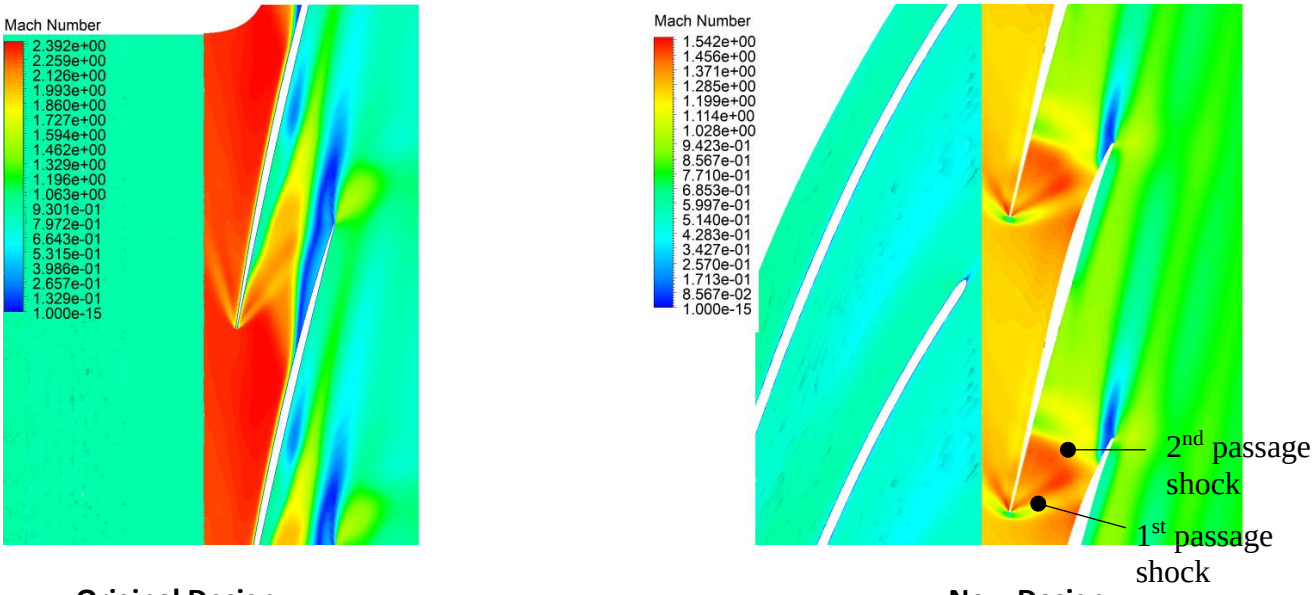

Figure 6-5 Relative Mach number at mid-span of original and new axial rotor

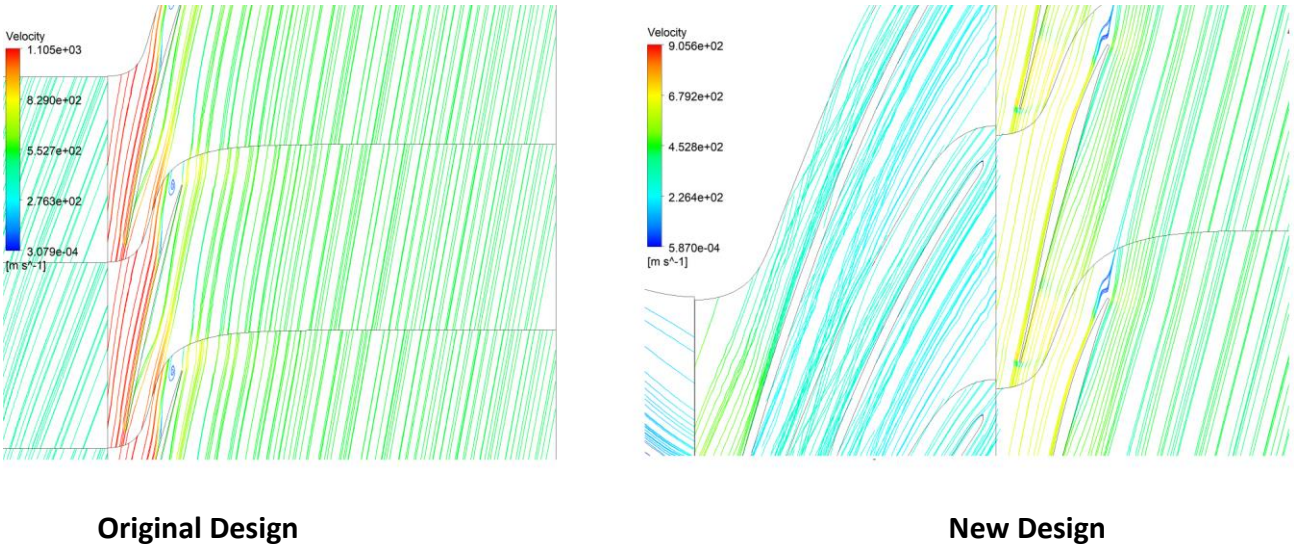

Figure 6-6 Streamlines at mid-span of original and new axial rotor

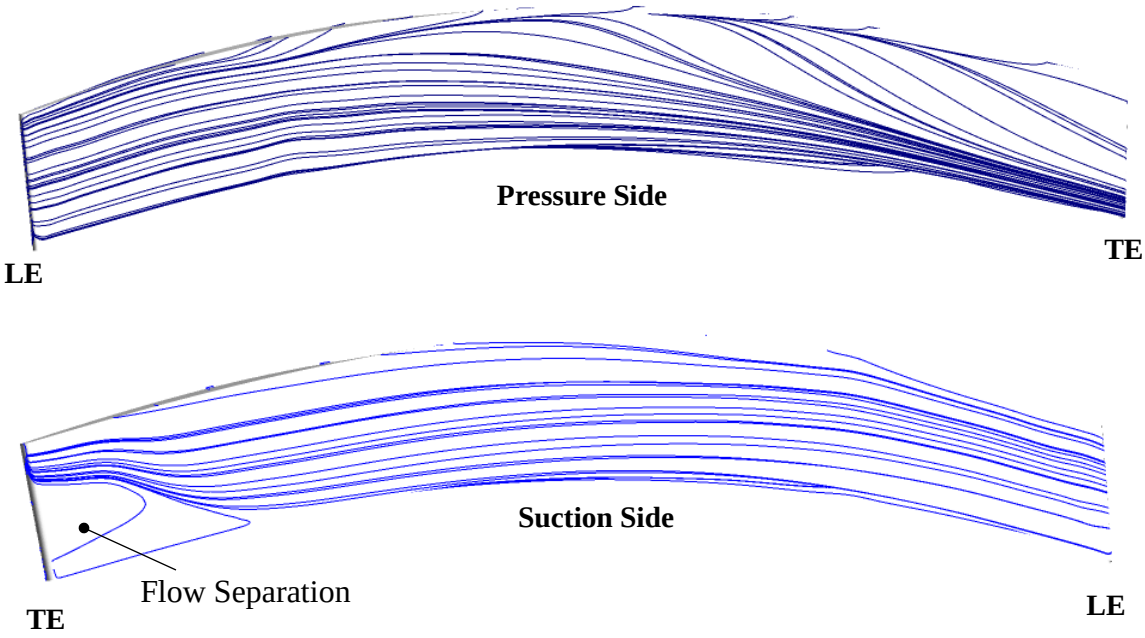

Figure 6-7 Surface streamlines for the pressure and suction sides of new axial rotor

The improved shock pattern (reduced shock loss) and reduced boundary layer separation (lower viscous loss) explains the significantly higher polytropic efficiency of the new axial rotor relative to the original design. However, the source of its still low polytropic efficiency (58.5%) can be found in Figure 6-8, which plots the entropy contours at different axial planes along the blade passage of the new axial rotor. The lowest entropy (darker blue) region represents the core flow. The higher entropy (light blue) region at the hub seen in the first two (most upstream) planes is the hub boundary layer, which takes on a relatively large proportion of the blade passage area due to the very short blade span (4.0 mm). The highest entropy (red) region seen in Figure 6-8 is the suction side boundary layer separation, which only appears near the trailing edge of the blade passage (most downstream plane shown). The viscous losses associated with these two high-entropy region are likely significant factors in penalizing the efficiency of the new axial rotor. However, one can observe that, in the absence of significant boundary layer separation, the tip clearance flow region (marked by dashed lines) takes over the large majority of the blade passage area, growing rapidly from leading edge to the trailing edge, merging with the hub boundary layer along the way to eliminate the core region completely near the trailing edge plane, creating a lot of viscous and mixing loss in the process. Thus, with reduced shock strength and flow separation, tip clearance flow becomes a major factor behind the low polytropic efficiency, as proven later in section 6.4. This unusually large impact of tip clearance on the efficiency of this

axial compressor rotor is a direct result of the large tip clearance over span ratio, which in the current case stands at 3.175% (0.127 mm / 4.0 mm). This is significantly higher than the value for typical axial compressors, which is usually much less than 1%. Had the blade span been higher for the same tip clearance (to bring the tip clearance over span ratio to more standard value), the tip clearance region would likely not have come anywhere near the hub boundary layer and a large core region would remain at the trailing edge.

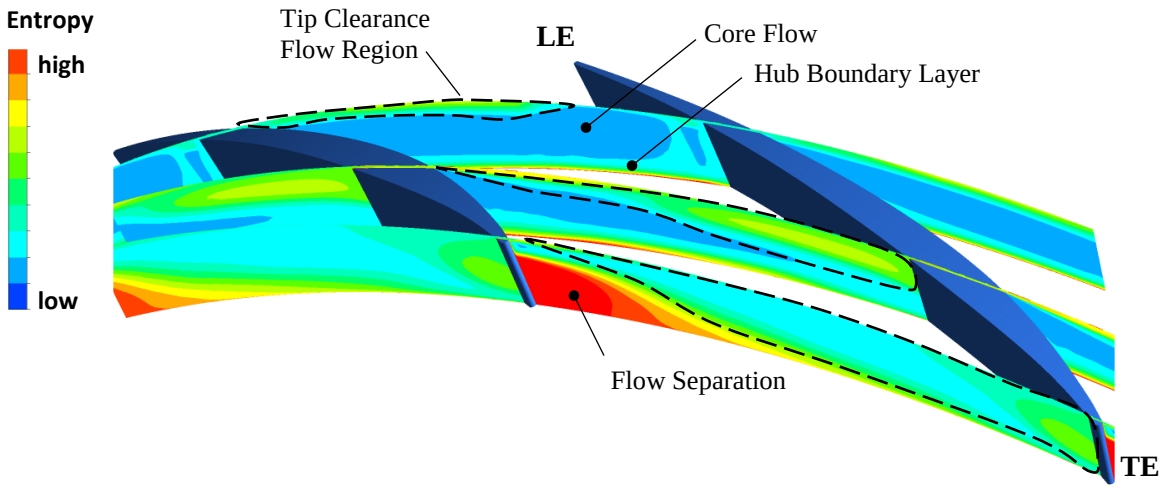

Figure 6-8 Entropy contours at different axial planes of new axial rotor

6.3 Off-design Performance

Figure 6-9 plots the variation of polytropic efficiency with corrected mass flow for the new CRC compressor and the reference CC compressor, while Figure 6-10 shows their total pressure rise characteristics, as obtained from additional simulations at off-design mass flow values all the way to the convergence limit (stall point) of each geometry. The filled points are results obtained by steady-state simulations while their empty equivalents are from the time-averaged solutions of transient simulations. Points *A*, *B* and *C* are the design, near-stall and stall (convergence limit) points of the new CRC compressor (from unsteady simulations) while points *a*, *b* and *c* are their counterparts for the CC compressor. Points *A'* and *a'* are the design point from steady-state simulations of the new CRC and CC compressors, respectively. Figure 6-10 also incorporates an additional point (point *S*) representing an instantaneous solution taken during the "single passage" stall transient to study flow field breakdown.

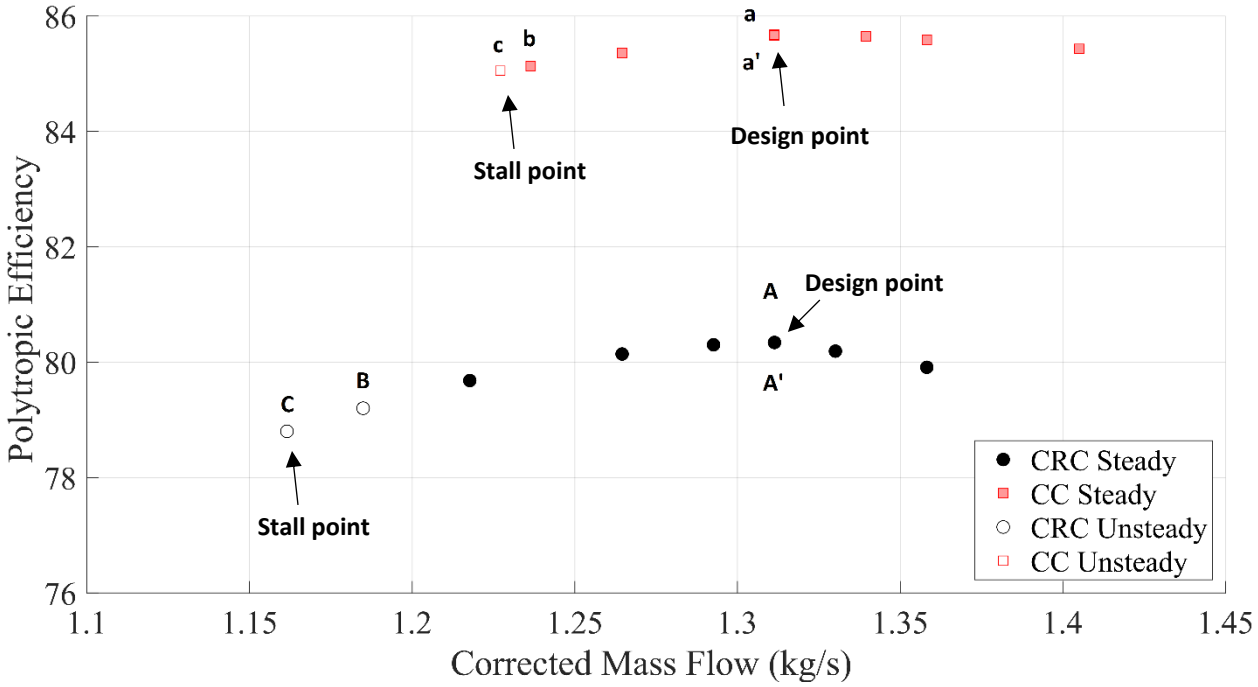

Figure 6-9 Variation of the polytropic efficiency with corrected mass flow rate

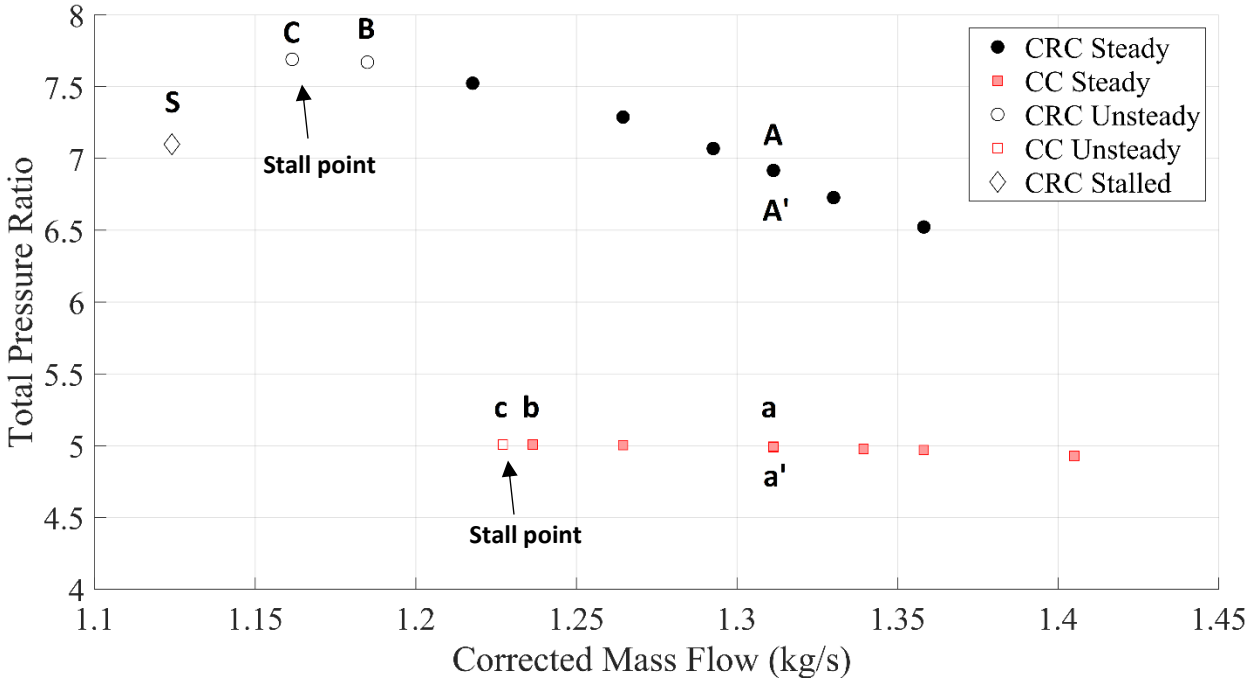

Figure 6-10 Variation of the total pressure ratio with corrected mass flow rate

Figure 6-9 confirms that the peak efficiency of each case occurs at the design mass flow for both CC and CRC compressors, thus validating their design points. Furthermore, the fact that the points from unsteady (time-averaged) and steady simulations at design mass flow in both Figure 6-9 and Figure 6-10 for each compressor visually overlap (points *a* versus *a'* and points *A* versus *A'*) indicates that the effect of any flow unsteadiness on their design point performance is negligible.

Figure 6-10 shows that the stall point for the CC compressor (point *c* in Figure 6-10) occurs at a corrected mass flow of 1.22 kg/s for a stall margin of 6.4% calculated according to equation (3.10). On the other hand, the new CRC compressor design stalls at 1.16 kg/s (point *C* in Figure 6-10) for a stall margin of 11.4%, representing a 5 % improvement relative to its equivalent conventional compressor. Although the impeller-alone simulations have not reached the convergence limit, they show convergence at mass flow below that of the CRC compressor stall point, indicating the counter-rotating axial rotor is the source of rotating stall, which is consistent with the literature on counter-rotating compressors. (Moreover, the fact that the impeller stalls at a lower mass flow than the CC compressor indicates that the fishtail pipe diffuser is the source of rotating stall in the CC compressor).

Figure 6-11 plots the entropy contours at the blade tip span of the impeller and axial rotor. The results shows that the interface between the incoming/tip clearance flow interface has already reached the leading edge of the axial rotor on the tip pressure side, marking the onset of tip clearance flow spillage into the adjacent the blade passage. This is a common criterion for spike stall inception reported for axial compressors [13] through [16] and even for impellers [57]. Figure 6-11 also indicates that this criterion is not satisfied for the impeller, which is consistent with the impeller not being the source of stall. Therefore, tip clearance flow breakdown in the axial rotor is likely the source of rotating stall for the CRC compressor. This conclusion is further supported by Figure 6-12, which presents the blade surface streamlines for the axial rotor as the CRC compressor is throttled towards stall (points *B* to *C* in Figure 6-10) and during the stall transients (point *S* in Figure 6-10) as the flow field breaks down. One can observe that the boundary layer separation region at the base of the suction side trailing edge of the axial rotor does not grow as the compressor approaches and goes into stall, nor does any other flow separation region develop during this throttling process. The same has been verified for the stator in the vaned diffuser.

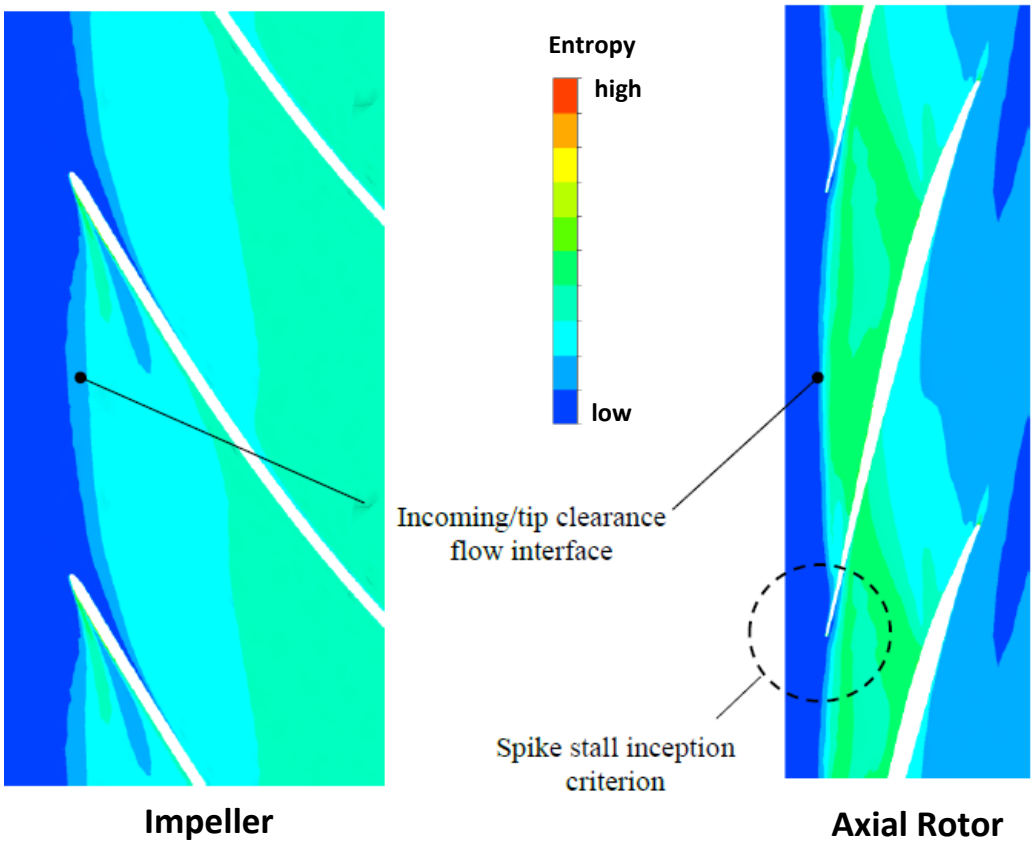

Figure 6-11 Entropy contours at blade tip span of impeller leading edge (left) and axial rotor (right) for CRC compressor at point C

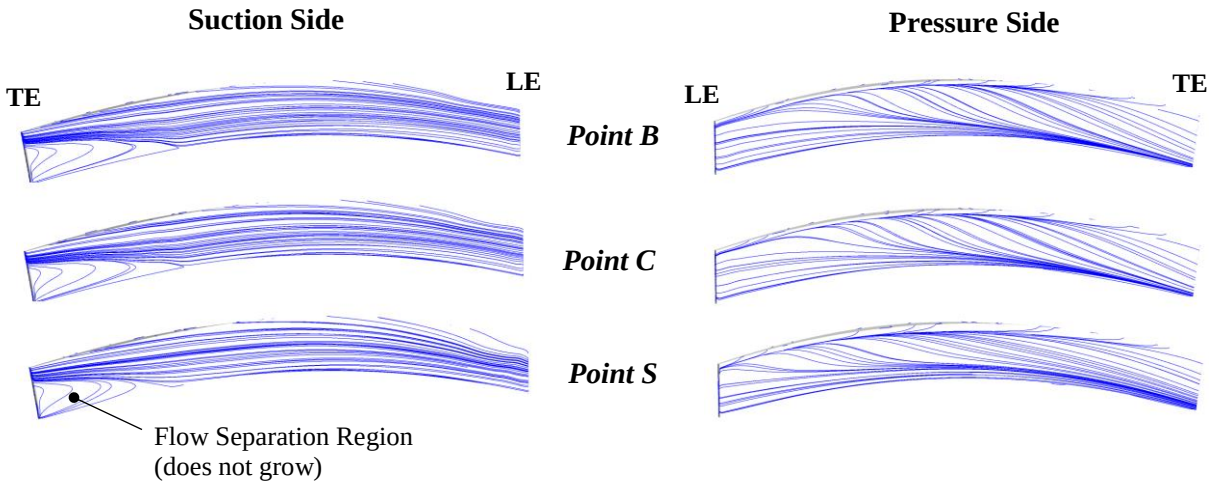

Figure 6-12 Surface streamlines for new axial rotor near stall and during stall transient

6.4 Further Design Improvement Strategies

The analysis so far of the new CRC compressor design indicate that this concept can significantly improve stall margin relative to its conventional compressor equivalent while being much more compact in both length and diameter. Thus, there is no need for design improvements with respect to aerodynamic stability. However, considering the additional gears or spool that would be required to implement this concept in real aero-engines, the design-point performance of the new CRC design is still far short of the initial targets to make this concept more attractive, namely of doubling the total pressure rise and maintaining similar polytropic efficiency to its CC compressor equivalent. This subsection proposes further design changes that should help the CRC compressor meet design total pressure ratio and efficiency targets.

6.4.1 Tip Clearance Reduction

Section 6.2 points to the high tip clearance (relative to blade span) being a major factor in reducing the polytropic efficiency of the axial rotor and by extension that of the new CRC compressor. However, the elimination of the tip clearance (using a shrouded rotor) may bring about flow separation at the shroud-suction side corner. On the other hand, reducing the tip clearance to below 0.005 inch is not practically feasible for an unshrouded compressor.

One solution is to apply the CRC compressor concept only for applications where the mass flow rate is sufficiently high such that the blade span on the downstream axial rotor is high enough to bring the tip clearance-to-blade span ratio to more typical values (well below 1%). The other is to use a shrouded axial rotor with very thin slit cuts on the shroud along the chord to mimic the effect of a small tip clearance. The aerodynamic effect of this solution is predicted with CFD simulation of the new CRC compressor design at a tip clearance of 0.001 inch (0.0254 mm or 0.64% of span). The change in performance of the CRC compressor at design mass flow is tabulated in Table 6-2.

The results indicate that the large reduction in tip clearance size has a highly significant impact on performance, bringing the new CRC compressor to within 2.5% of the target polytropic efficiency and the total pressure rise of the axial rotor from 46% to 89% of that of the impeller (target). Figure 6-13 shows that the increase of over 3% in CRC compressor polytropic efficiency

comes from the increase in polytropic efficiency of the axial rotor, which changes from 58.5% to 78.8% from lowering its tip clearance size.

Table 6-2 Effect of tip clearance size on performance of CRC compressor at design mass flow

Parameter	**New CRC Compressor**		
	Target	**0.005 inch t.c.**	**0.001 inch t.c**
Total pressure ratio (*PR*)	9.20	6.97	8.73
Polytropic efficiency (η_{poly})	0.856	0.804	0.831
Exit flow angle (deg.)	0	-1.6	-48.5

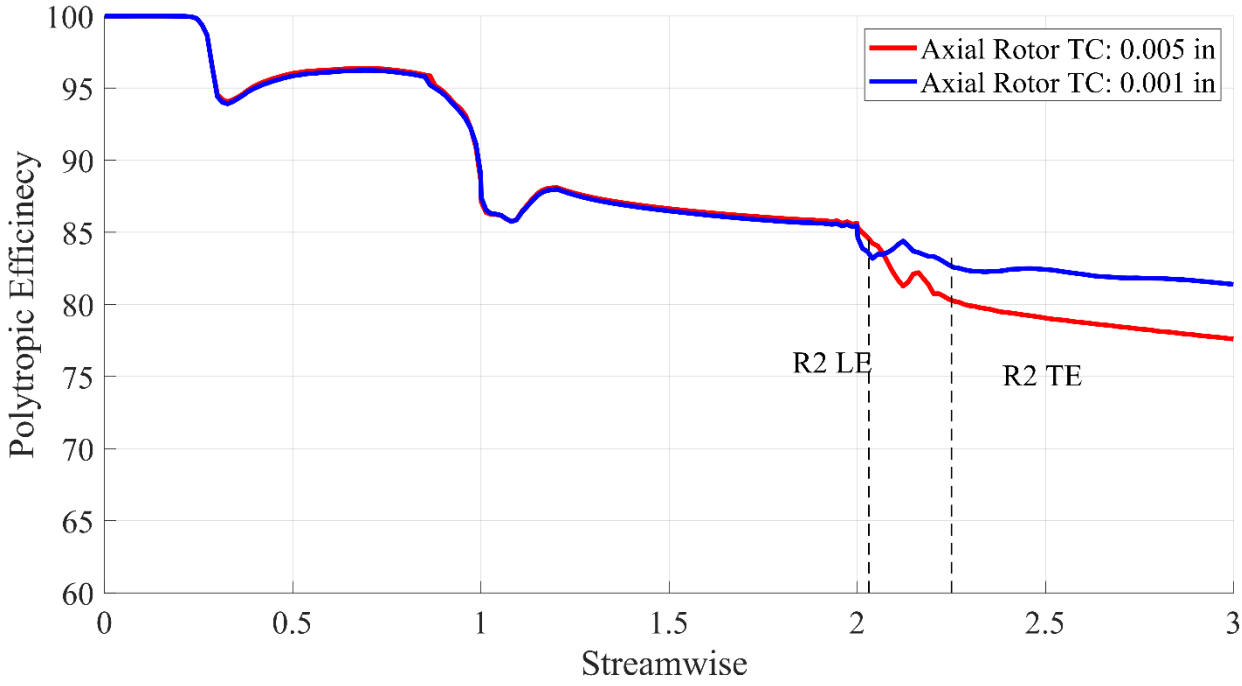

Figure 6-13 Variation of polytropic efficiency from inlet to outlet of new CRC compressor for different axial rotor tip clearances

Figure 6-14 plots the entropy contours at different axial planes along the blade passage of the new axial rotor at 0.001 inch tip clearance. When compared to Figure 6-8, one can observe that the tip clearance flow region grows much more slowly along the passage, indicating reduced loss from tip clearance flow in this case. Indeed, its proportion of the passage area does not seem

higher than that of the hub or pressure side boundary layers nor that of the separated suction side boundary layer. As a result, a core region is still visible at the rotor exit plane.

Moreover, given the very short blade span, the reduced size of the tip clearance flow region has a large impact on the flow field as evidenced by the flow separation on the suction side whose extent has significantly increased both chordwise and spanwise when comparing the suction side surface streamlines of the axial rotor on Figure 6-15 to those in Figure 6-7. The resulting change in passage flow field increases the flow turning by the axial rotor in the absolute frame past the axial direction as indicated in Table 6-2 and evidenced by Figure 6-16. This explains the much higher total pressure seen at reduced axial rotor tip clearance, based on the explanation associated with equation (6.6).

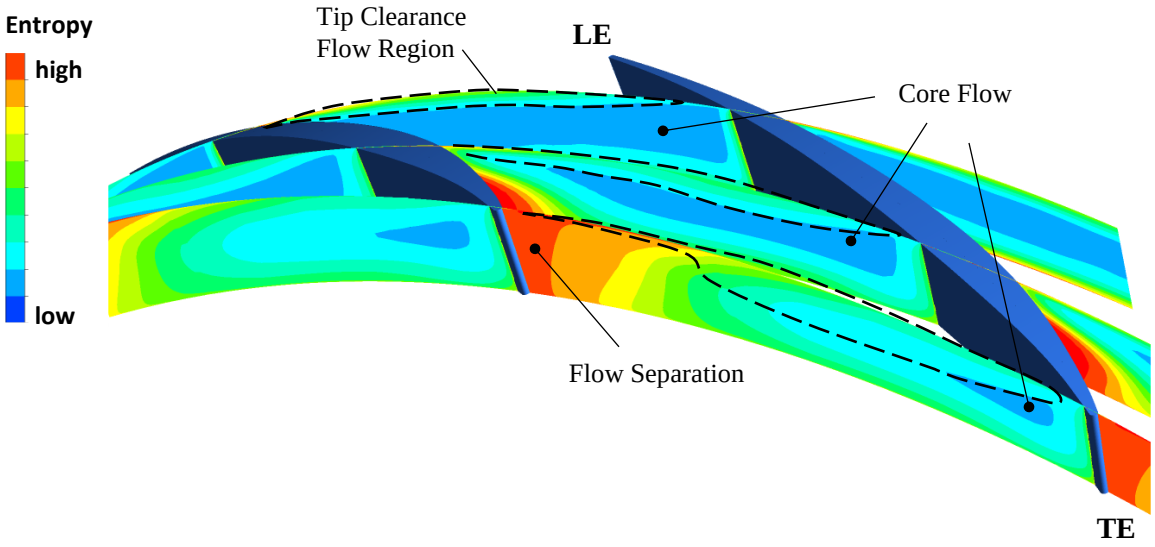

Figure 6-14 Entropy contours at different axial planes of new axial rotor with reduced (0.001 inch) tip clearance

If a non-axial exit flow is required for a CRC compressor design to have acceptably high total pressure ratio with high polytropic efficiency, there are two solutions for an implementation of this concept in a gas turbine engine. The first consists of adding a stator downstream of the axial rotor to bring the flow back to the axial direction while sacrificing a few percent in polytropic efficiency. The second solution involves designing the downstream engine component to cope with non-axial flow. If the CRC compressor is the last stage of a gas turbine engine with a spool linking its counter-rotating axial rotor to a turbine rotor as illustrated in Figure 1-5 (red spools), a non-axial combustor can be implemented, as illustrated in Figure 6-17, so that the flow exiting

the CRC compressor does not need to be de-swirled (redirected to axial direction). The swirling flow that exits the combustor can feed directly the first turbine rotor (without upstream stator) that in turns drives the axial compressor rotor.

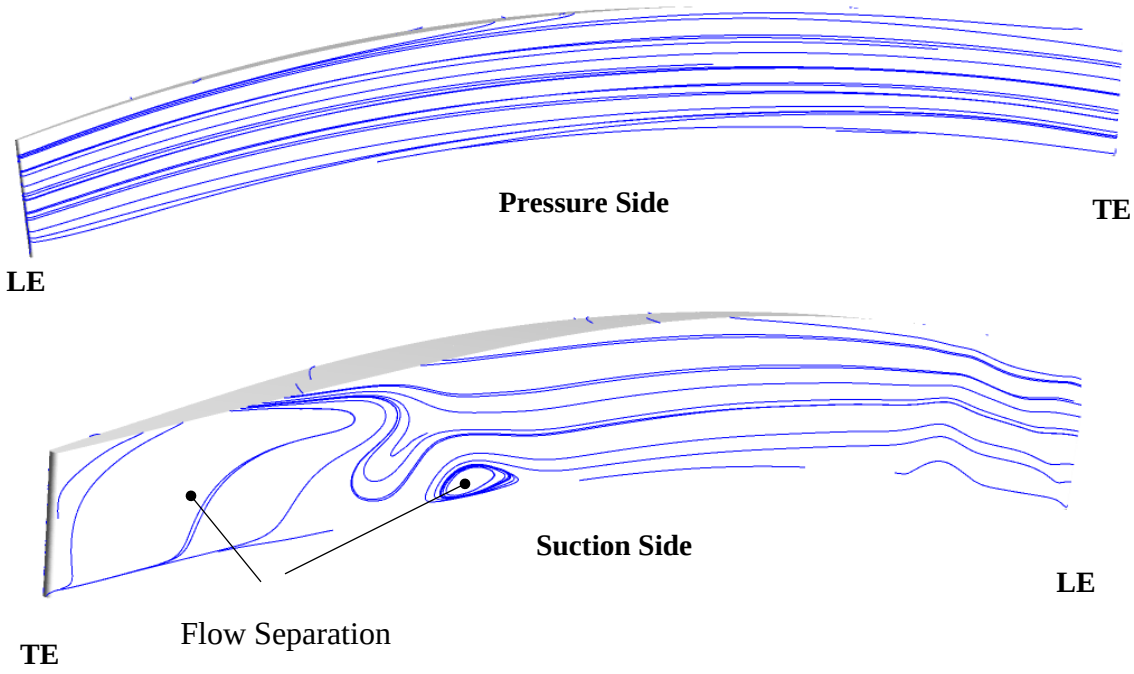

Figure 6-15 Surface streamlines for the pressure and suction side of new axial rotor with reduced (0.001 inch) tip clearance

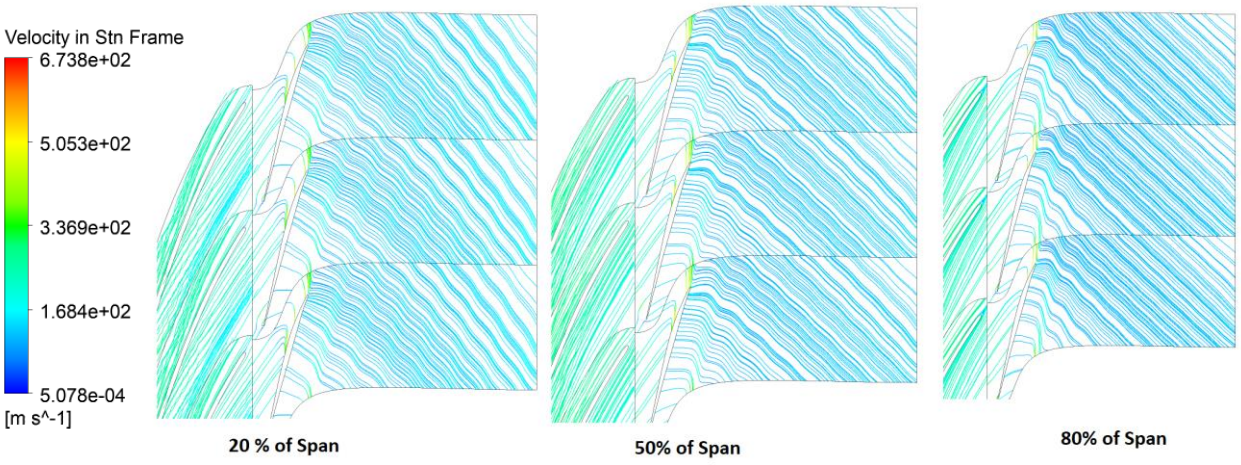

Figure 6-16 Streamlines in stationary frame across new axial rotor with reduced (0.001 inch) tip clearance

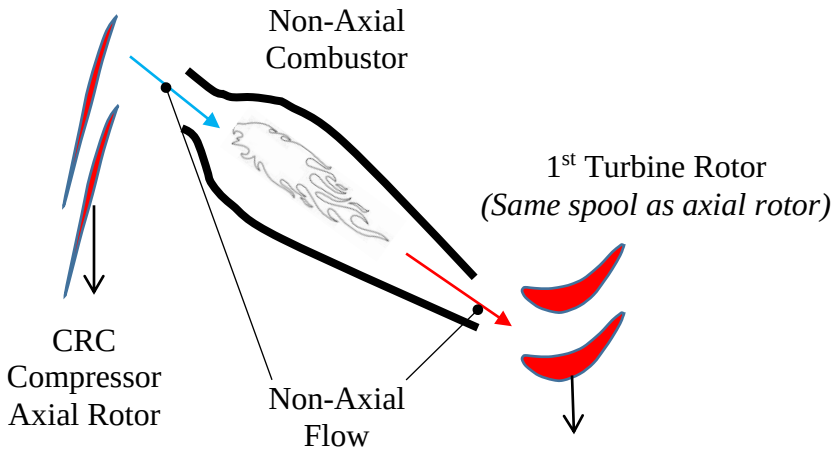

Figure 6-17 Example of engine implementation for CRC compressor with non-axial exit flow

6.4.2 Axial Rotor Blade Optimization

Figure 6-14 and Figure 6-15 indicate that while a smaller tip clearance on the axial rotor significantly reduces losses in the axial rotor and allows the CRC compressor to get close to performance targets, the boundary layer separation on the suction side has significantly worsened. Therefore, there is still significant potential for further improvement in efficiency and pressure ratio by optimizing the axial compressor rotor geometry to eliminate this separation and associated losses.

6.4.3 Vaned Diffuser Optimization

Figure 6-18 shows a meridional view of the vaned diffuser inlet along with flow vectors. These vectors indicate a flow recirculation bubble in the inlet tip region due to the impeller tip clearance flow. This region overlaps with the outer span of the stator vane leading edge, which creates a flow separation region on the blade tip (see Figure 5-11) and associated losses that can be recovered to improve CRC compressor efficiency. Attempts to move the stator vane leading edge downstream to avoid this region results in flow separation on the hub gas path (similar to that shown in Figure 5-7). A nonlinear stator vane leading edge as shown by the dashed line in Figure 6-18 could resolve this issue and allow a small efficiency improvement.

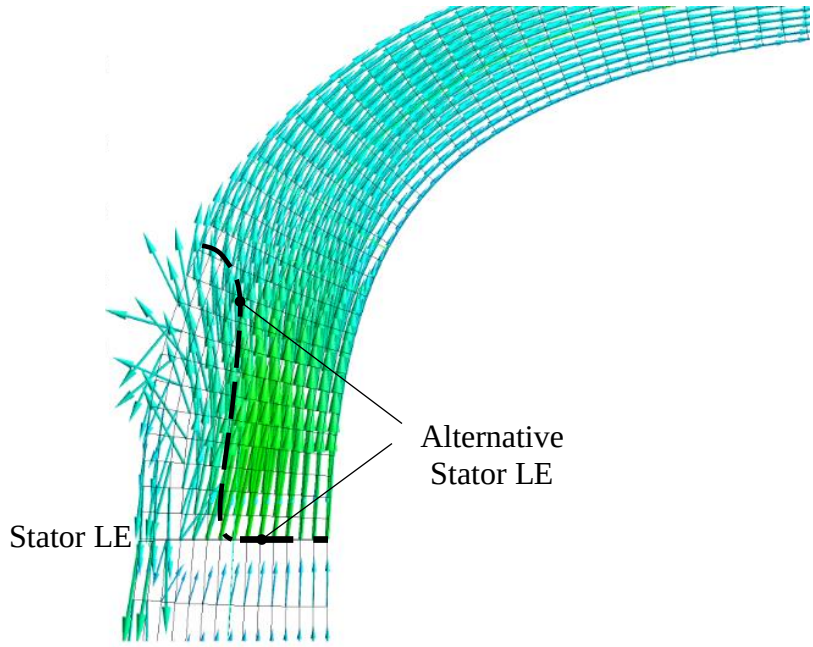

Figure 6-18 Flow vectors at inlet of vaned diffuser

6.4.2 Impeller Redesign

The work so far has been constrained by the use of the same impeller in both the CC and CRC compressors. A conventional impeller imposes the use of a vaneless diffuser or vaned diffuser as designed in Section 5.3 to remove the radial component of the flow exiting the impeller, which incurs three drawbacks. The first is the additional losses brought about by the vaneless or vaned diffuser which can bring the polytropic efficiency down by about 5%. Second, this component raises the overall diameter of the CRC compressor. Finally, the larger diameter increases the circumferential velocity (U_3 in Figure 3-12) of the downstream counter-rotating axial rotor which leads to higher relative inlet Mach number (and thus shock-related losses) as well as reduces blade height (hence increasing tip clearance-related losses).

One possible solution consists of replacing the centrifugal impeller with an aggressive (short axial extent) mixed flow rotor, as illustrated in Figure 6-19, with the same mean exit radius as the impeller exit radius and providing the same exit velocity magnitude and angle as the impeller but with an axial rather than radial velocity component. While a stator may have to be placed downstream to reduce the high swirl of the exit flow (instead of the original vaneless/vaned diffuser), the radial extent of the compressor would be reduced along with its impact on the losses related to shock and tip clearance as discussed in the previous paragraph.

The initial mixed flow rotor design shown in Figure 6-19 is simulated in CFD with a downstream stator that gives similar exit flow velocity and angle as the exit of the vaned diffuser of the new CRC design presented in sections 6.1 to 6.3. These simulations indicate that the polytropic efficiency of the mixed flow rotor and stator combination could be higher than that of the impeller-vaned diffuser combination. Moreover, the gas path height at the stator exit (i.e. axial rotor inlet) is 7.0 mm compares to 4.0 mm for the vaned diffuser exit. These preliminary results are highly promising and indicate that the use of an aggressive mixed flow rotor could allow for the CRC compressor concept to more easily reach performance targets.

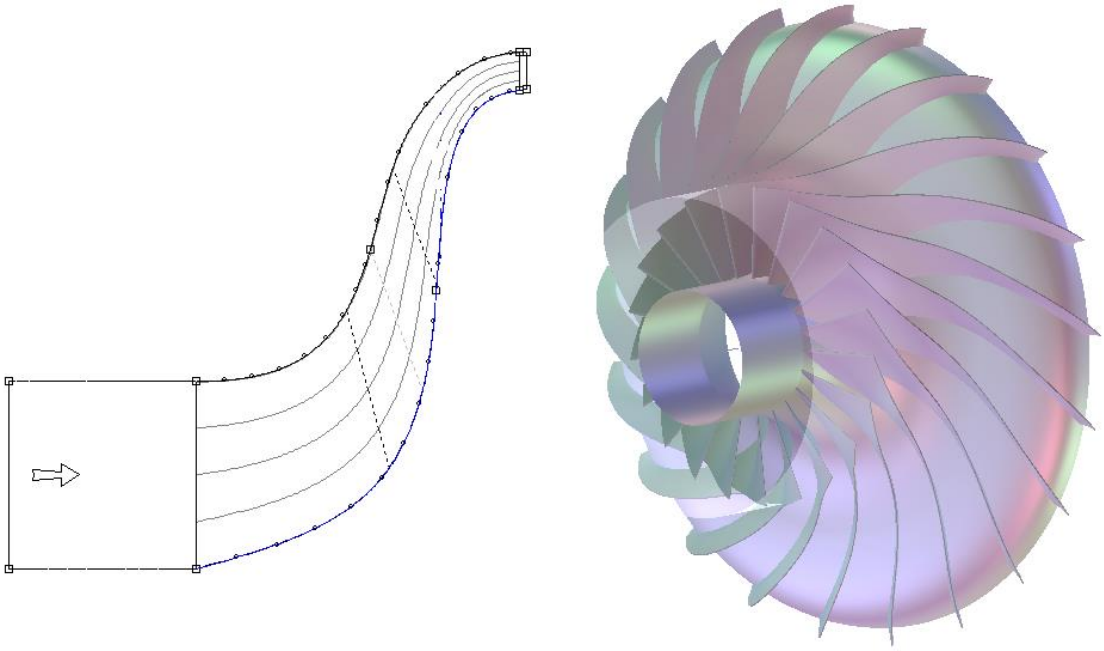

Figure 6-19 Mixed flow rotor with similar dimensions and performance to impeller

CHAPTER 7 SUMMARY, CONCLUSION AND FUTURE WORK

A novel counter-rotating centrifugal compressor concept had been proposed to double the total pressure rise of an equivalent centrifugal compressor at similar efficiency in a simpler and smaller design. This concept can reduce the fuel consumption of an aero-engine and/or its size, weight and mechanical complexity. However, it had only been evaluated at speeds that are far below that required for real gas turbine engine applications. The present work provides the first assessment of this concept at realistic transonic speeds to identify the aerodynamic issues that can prevent the concept from reaching to its full potential and proposes and assesses design strategies to address them. As a result, this work constitutes a first and crucial step toward the implementation of the counter-rotating centrifugal compressor concept in gas turbine engines.

This research chooses a computational approach for rapid assessment of design changes and detailed analysis of the flow field. The project is divided into four phases. Phase 1 consists of designing a representative conventional centrifugal (CC) compressor and the first version of its counter-rotating (CRC) equivalent, which has the same design mass flow and uses the same impeller but replaces the diffuser with a vaneless diffuser and a counter-rotating axial rotor rotating at the same speed as the impeller. The design performance targets for the CRC design are to double the total pressure rise of CC compressor at the same (or better) polytropic efficiency and stall margin with an axial flow exit. In phase 2, a detailed assessment of the first CRC compressor design is performed to quantify its performance shortfalls and identify their causes. Phase 3 is devoted to addressing these shortfalls with the evaluation and implementation of strategies to improve the CRC compressor. Finally, phase 4 evaluates the new (revised) CRC compressor design to validate the improvements, verify aerodynamic stability (stall margin) and elucidate the causes for any remaining performance shortfall and for stall in order to propose strategies for further improvements.

The main findings of this work can be summarized as follows:

- The counter-rotating axial rotor is the main source of performance deficit in the CRC compressor concept at transonic speeds.
- The low efficiency of the axial rotor is due to highly supersonic inlet relative Mach number from the counter-rotation. This leads to shock losses and high viscous losses from

shock-induced boundary layer separation, which must be reduced through lowering relative inlet Mach number and shock strength to bring the polytropic efficiency to reasonable values.

- The most effective first-line improvement strategies are a combination of axial rotor speed reduction and replacement of the vaneless diffuser by a vaned diffuser to reduce the inlet relative Mach number to low supersonic values, along with optimized un-cambered blade profile to reduce shock strength through multiple passage shocks.
- Implementation of the first-line improvement strategies greatly increases polytropic efficiency of the CRC compressor but decreases total pressure ratio due to reduced work from lower rotation speed and reduced inlet swirl of the axial rotor. In this case, the total pressure rise of the axial rotor can only equal that of the impeller if the CRC compressor exit flow is allowed to be non-axial.
- For CRC compressors with an axial rotor of very low blade span, the losses associated with tip clearance flow in this rotor will likely prevent the CRC compressor from closing the efficiency gap with its target once the shock related losses are resolved. This can be addressed through reducing the ratio of tip clearance-to-blade span to standard values (well below 1%) which may involve using a shrouded rotor if the blade height is small.
- High-speed CRC compressors should have better stall margin than equivalent CC compressors even with relatively large axial rotor tip clearance. The counter-rotating axial rotor is likely the source of stall inception through tip clearance flow breakdown.
- Further improvement strategies to achieve the full potential of the CRC compressor concept in terms of design point performance also include optimizing the shape of the vaned diffuser and of the axial rotor to remove all flow separation, as well as replacing the impeller by an aggressive mixed flow rotor.

Based on the above findings, the proposed future work consists of the following tasks:

- Implement the suggested improvements in section 6.4 to achieve the performance targets for the CRC compressor design
- Experimentally validate the best CRC compressor design on a compressor test rig

REFERENCES

[1] Engine Alliance GP7000. (2020, November 17). Retrieved from Wikipedia website: https://en.wikipedia.org/wiki/Engine_Alliance_GP7000

[2] Braembussche R. V. (2019). Design and Analysis of Centrifugal Compressors. Chichester, UK: John Wiley & Sons, Ltd

[3] Vo, H.D. (2016). Counter-rotating compressor (Patent No US 20170074280A1 - Application). https://patents.google.com/patent/US20170074280A1

[4] Dejour, Q., & Vo, H. D. (2018). Assessment of a Novel Non-Axial Counter-Rotating Compressor Concept for Aero-Engines. Volume 2A: Turbomachinery. https://doi.org/10.1115/gt2018-77039

[5] Dejour, Q & Vo, H.D., (2022). Assessment of A Novel Counter-Rotating Centrifugal Compressor Concept for Aero-Engines. Paper currently under work.

[6] Chen, F. Y. (2020). Estimation d'impact d'un Nouveau Concept de Compresseur sur Moteurs d'avion. Rapport Projet Intégrateur 3, Polytechnique Montréal.

[7] Koch, , C. C., & Smith, L. H., Jr. (1976). Loss Sources and Magnitudes in Axial-Flow Compressors. Journal of Engineering for Power, 98(3), 411–424. https://doi.org/10.1115/1.344620

[8] Lei, V. M., Spakovszky, Z. S., & Greitzer, E. M. (2008). A Criterion for Axial Compressor Hub-Corner Stall. Journal of Turbomachinery, 130(3).

[9] Storer, J. A., & Cumpsty, N. A. (1991). Tip Leakage Flow in Axial Compressors. Journal of Turbomachinery, 113(2), 252-259. doi: 10.1115/1.2929095

[10] Camp, T. R., & Day, I. J. (1997). A Study of Spike and Modal Stall Phenomena in a Low-Speed Axial Compressor. Paper presented at the ASME 1997 International Gas Turbine and Aero engine Congress and Exhibition.

[11] Greitzer, E. M., & Moore, F. K. (1986). A Theory of Post-Stall Transients in Axial Compression Systems: Part II—Application. Journal of Engineering for Gas Turbines and Power, 108(2), 231-239. doi: 10.1115/1.3239893

[12] Day, I. J. (1993). Active Suppression of Rotating Stall and Surge in Axial Compressors. Journal of Turbomachinery, 115(1), 40-47. doi: 10.1115/1.2929216

[13] Vo, H. D., Tan, C. S., & Greitzer, E. M. (2008). Criteria for Spike Initiated Rotating Stall. Journal of Turbomachinery, 130(1). doi: 10.1115/1.2750674.

[14] Deppe, A., Saathoff, H. & Stark,U. (2005). Spike-type stall inception in Axial Flow Compressors. proceedings of 6th Conference on Turbomachinery, Fluid Dynamics and Thermodynamics, Lille, France.

[15] Hah, C., Bergner, J. r., & Schiffer, H.-P. (2006). Short Length-Scale Rotating Stall Inception in a Transonic Axial Compressor: Criteria and Mechanisms. Paper presented at the ASME Turbo Expo 2006: Power for Land, Sea, and Air.

[16] Bennington, M. A., Cameron, J. D., Morris, S. C., & Gendrich, C. P. (2007). Over Rotor Casing Surface Streak Measurements in a High Speed Axial Compressor. Volume 6: Turbo Expo 2007, Parts a and B. https://doi.org/10.1115/gt2007-28273.

[17] Kantrowitz, A. (1950). The Supersonic Axial-Flow Compressor. NACA Rept. 974

[18] York, R. E., & Woodard, H. S. (1976). Supersonic Compressor Cascades—An Analysis of the Entrance Region Flow Field Containing Detached Shock Waves. Journal of Engineering for Power, 98(2), 247–254. https://doi.org/10.1115/1.3446153

[19] Gustafson, B.-A. . (1976). A Simple Method for Supersonic Compressor Cascading Performance Prediction. Volume 1A: General. https://doi.org/10.1115/76-gt-64

[20] Broichhausen, K.-D., & Gallus, H. E. (1982). Theoretical and Experimental Analysis of the Flow through Supersonic Compressor Rotors. AIAA Journal, 20(8), 1097–1103. https://doi.org/10.2514/3.51169

[21] Freeman, C., & Cumpsty, N. A. (1989). A Method for the Prediction of Supersonic Compressor Blade Performance. Volume 1: Turbomachinery.

[22] Schreiber, H. A., & Starken, H. (1992). An Investigation of a Strong Shock-Wave Turbulent Boundary Layer Interaction in a Supersonic Compressor Cascade. Journal of Turbomachinery, 114(3), 494–503. https://doi.org/10.1115/1.2929170

[23] Suder, K. L., (1996). Experimental Investigation of the Flow Field in a Transonic, Axial Flow Compressor With Respect to the Development of Blockage and Loss. Ph.D. Dissertation, Case Western Reserve University: also NASA TM 107310.

[24] Bloch, G. S., Copenhaver, W. W., & O'Brien, W. F. (1999). A Shock Loss Model for Supersonic Compressor Cascades. Journal of Turbomachinery, 121(1), 28–35. https://doi.org/10.1115/1.2841231

[25] Burguburu, S., Toussaint, C., Bonhomme, C., & Leroy, G. (2004). Numerical Optimization of Turbomachinery Bladings. Journal of Turbomachinery, 126(1), 91–100. https://doi.org/10.1115/1.1645869

[26] Sonoda, T., Olhofer, M., Arima, T., & Sendhoff, B. (2009). A New Concept of a Two-Dimensional Supersonic Relative Inlet Mach number Compressor Cascade. Volume 7: Turbomachinery, Parts a and B. https://doi.org/10.1115/gt2009-59926

[27] Liu, B., Shi, H., & Yu, X. (2017). A New Method for Rapid Shock Loss Evaluation and Reduction for the Optimization Design of a Supersonic Compressor Cascade. Proceedings of the Institution of Mechanical Engineers, Part G: Journal of Aerospace Engineering, 232(13), 2458–2476. https://doi.org/10.1177/0954410017715277

[28] Wennerstrom, A. J. (1990). Highly Loaded Axial Flow Compressors: History and Current Developments. Journal of Turbomachinery, 112(4), 567-578

[29] Sharma, P. B., Jain, Y. P., Jha, N.K., & Khanna, B.B. (1985). Stalling Behaviour of a Contra-Rotating Axial Compressor Stage. ISABE paper 85-7087.

[30] Sharma, P.B., Jain, Y., & Pundhir, D.S. (1988). A Study of Some Factors Affecting the Performance of a Contra-Rotating Axial Compressor Stage. Proceedings of the Institution of Mechanical Engineers, Journal of Power and Energy, 202, 15 - 21.

[31] Pundhir, D., & Sharma, P.B. (1992). A Study of Aerodynamic Performance of a Contra Rotating Axial Compressor Stage. Defence Science Journal, 42, 191-199.

[32] Chen, Y.-Y., Liu, B., Xuan, Y., & Xiang, X.-R. (2008). A Study of Speed Ratio Affecting the Performance of a Contra-Rotating Axial Compressor. Proceedings of the Institution of Mechanical Engineers, Part G: Journal of Aerospace Engineering, 222(7), 985–991

[33] Wang, Z., Yuan, W., Li, Q., & Lu, Y. (2012). Experimental Investigation on the Stall Inception of a Counter-Rotating Compressor. Paper presented at the ASME Turbo Expo 2012: Turbine Technical Conference and Exposition.

[34] Mao, X., & Liu, B. (2016). Numerical Study of the Unsteady Behaviors and Rotating Stall Inception Process In a Counter-Rotating Axial Compressor. Proceedings of the Institution of Mechanical Engineers, Part G: Journal of Aerospace Engineering, 230(14), 2716–2727.

[35] Wallscheid, L., Eulitz, F., & Heinecke, R. (1998). Investigation of Unsteady Flow Phenomena in a Counterrotating Ducted Propfan. Paper presented at the ASME 1998 International Gas Turbine and Aeroengine Congress and Exhibition.

[36] Cho, L., Choi, H., Lee, S., & Cho, J. (2009). Numerical and Experimental Analyses for the Aerodynamic Design of High Performance Counter-Rotating Axial Flow Fans. Paper presented at the ASME 2009 Fluids Engineering Division Summer Meeting.

[37] Mistry, C. S., & Pradeep, A. M. (2012). Effect of Speed Ratio and Axial Spacing Variations on the Performance of a High Aspect Ratio, Low Speed Contra-Rotating Fan. Paper presented at the ASME Turbo Expo 2012: Turbine Technical Conference.

[38] Wang, J., Ravelet, F., & Bakir, F. (2013). Experimental Comparison between a Counter-Rotating Axial-Flow Fan and a Conventional Rotor-Stator Stage. In 10th European turbomachinery conference (p. 1).

[39] Sun, X., Meng, D., Liu, B., & Wang, Q. (2017). Numerical Investigation of Differential Speed Operation of Two Impellers of Contra-Rotating Axial-Flow Fan. Advances in Mechanical Engineering.

[40] Lengyel, T., Voss, C., Schmidt, T., & Nicke, E. (2009). Design of a Counter Rotating Fan - An Aircraft Engine Technology to Reduce Noise and CO2-Emissions. ISABE 2009, 8-12.09.2009, Montreal, Canada.

[41] Goerke, D., Le Denmat, A.-L., Schmidt, T., Kocian, F., & Nicke, E. (2012). Aerodynamic and Mechanical Optimization of CF/PEEK Blades of a Counter Rotating Fan. Paper presented at the ASME Turbo Expo 2012: Turbine Technical Conference

[42] Backhaus, J., Aulich, M., Frey, C., Lengyel, T., & Voss, C. (2012). Gradient Enhanced Surrogate Models Based on Adjoint CFD Methods for the Design of a Counter Rotating Turbofan. Paper presented at the ASME Turbo Expo 2012: Turbine Technical.

[43] Aungier, R. H. (1995). Centrifugal Compressor Stage Preliminary Aerodynamic Design and Component Sizing. Paper presented at the ASME 1995 International Gas Turbine and Aeroengine Congress and Exposition

[44] Lüdtke, K. H. (2004). Process Centrifugal Compressors: Basics, Function, Operation, Design, Application: Springer.

[45] Whitfield, A. (1990). Preliminary Design and Performance Prediction Techniques for Centrifugal Compressors. Proceedings of the Institution of Mechanical Engineers, Part A: Journal of Power and Energy, 204(2), 131–144.

[46] Came, P. M. (1978). The Development, Application and Experimental Evaluation of a Design Procedure for Centrifugal Compressors. Proceedings of the Institution of Mechanical Engineers, 192(1), 49–67.

[47] Japikse D.(1996). Centrifugal Compressor Design and Performance: Concepts ETI.

[48] H. Cohen, G.F.C. Rogers, Paul Straznicky, H.I.H., Saravanamuttoo, Andrew Nix, (2017). Gas Turbine Theory. Edition 7, Pearson Education Limited,

[49] Aungier, R. H. (2003), Axial-Flow Compressors, New York Press,

[50] Cumpsty, N. A. (2004). Compressor aerodynamics. Malabar, Fla: Krieger Pub.

[51] Mikolajczak, A. A., Morris, A. L., & Johnson, B. V. (January 1, 1971). Comparison of Performance of Supersonic Blading in Cascade and in Compressor Rotors. ASME. J. Eng. Power. January 1971; 93(1): 42–48.

[52] Ge Han, Xingen Lu, Yanfeng Zhang, Shengfeng Zhao, Chengwu Yang & Junqiang Zhu, (2016). Study of Geometric Parameter Influence on Fishtail Pipe Diffuser Performance. Proceedings of the ASME Turbo Expo 2016: Seoul, South Korea.

[53] Bourgeois, J.A., Martinuzzi, R.J., Savory, E., Zhang, C. & Roberts, D.A. (2010). Assessment of Turbulence Model Predictions for an Aero-Engine Centrifugal Compressor. Journal of Turbomachinery, 133(1).

[54] Yin, S., Jin, D., Gui, X. & Zhu, F. (2010). Application and Comparison of SST Model in Numerical Simulation of the Axial Compressors. Journal of Thermal Science, 19(4), pp.300–309.

[55] ANSYS, (2020). ANSYS CFX-Modeling Guide. Ansys Inc, Canonsburg, PA, USA.

[56] Denton, J. D. (1997). Lessons from Rotor 37. Journal of Thermal Science, 6(1), 1–13.

[57] Ashrafi, F., Michaud, M., & Duc Vo, H. (2016). Delay of Rotating Stall in Compressors Using Plasma Actuators. Journal of Turbomachinery, 138(9).

APPENDIX A 3D BLADE DESIGN

This appendix describes the procedure for generating 3D blade geometry using ANSYS BladeGen, a turbomachinery geometry creation software, used in this research to generate the 3D geometry of the impeller, stator (vaned diffuser) and un-cambered axial rotor. The output of this software can be sent directly to ANSYS TurboGrid for meshing and then to ANSYS CFX for CFD simulations.

ANSYS BladeGen has two different modes for geometry generation. These modes are Angle/Thickness and the Pressure Side/Suction Side modes, with the former chosen for this project. For this mode, all the input parameters are listed below,

- hub and shroud gas path curve
- leading edge and trailing edge shape
- number of blades
- blade chord
- camber line angle distribution from leading edge to trailing edge (include LE and TE angles)
- angular position of the camber line distribution from leading edge to trailing edge
- thickness distribution from leading edge to trailing edge

The graphical user interface of this software is shown in Figure A-1 for the Angle/Thickness mode. (The case shown is for the un-cambered axial rotor.) The first two items, namely the curves for the hub, shroud, inlet, and outlet, shown in the upper left section of Figure A-1, could be generated using *Bezier Segment*, *Cubic Spline Segment, Polynomial Segment* or *Piecewise Linear Segment*. The location of points or control points for these curves could be chosen easily using Point Drag Control method.

The last four items in the list apply for each span location for which a blade profile is defined. The distributions of camber line angle and angular position of the camber line are shown in the lower left hand corner of Figure A-1 while the thickness distribution is shown in the lower right hind corner.

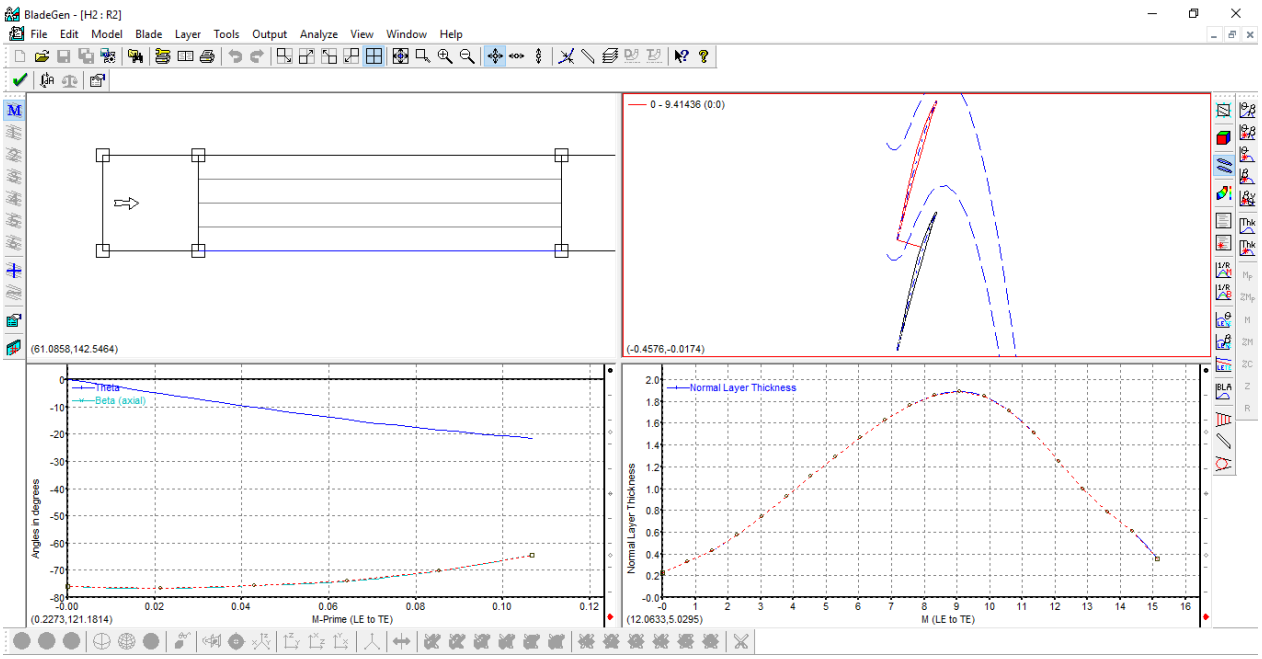

Figure A-1 User interface for ANSYS BladeGen

APPENDIX B MESH STUDY

This appendix presents the results of the mesh studies for the impeller, fishtail diffuser, vaneless diffuser axial rotor and stator (diffuser vane). The meshes for the blade rows (impeller, axial rotor and stator) are structured and generated using the ANSYS TurboGrid. The meshes for the Vaneless diffuser and fishtail diffuser are unstructured and generated with ICEM CFD. For each component, a table provides the number of elements and values of y+ for each mesh, with the mesh label "1x" being the chosen final mesh, followed by a plot of a performance parameter versus the number of elements.

B.1 Impeller

Table B-1 Data for impeller mesh study

	Type	0.25x	1x	4x
Impeller Mesh	Structured	180,269	719,246	2,826,573
Mean y+	-	2.95	0.72	0.39
Maximum y+	-	10.85	3.95	2.65

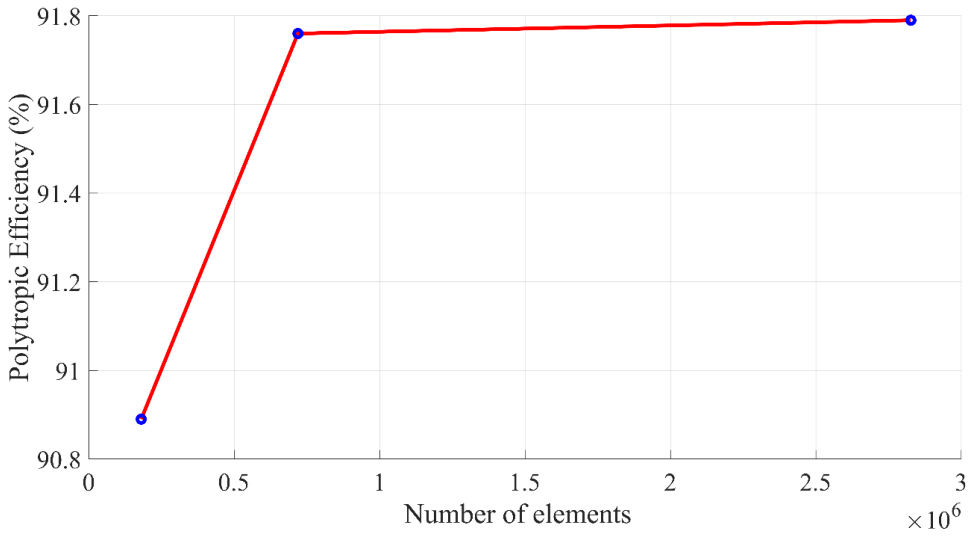

Figure B-1 Polytropic efficiency of impeller versus number of elements for impeller

B.2 Fishtail Diffuser

Table B-2 Data for fishtail diffuser mesh study

	Type	0.25x	1x	4x
Impeller Mesh	Structured	719,246	719,246	719,246
Fishtail Diffuser Mesh	Unstructured	325,288	1,301,150	5,204,600
Total	-	1,044,534	2,020,396	5,923,846
Mean y+	-	37.85	8.18	3.31
Maximum y+	-	67.01	14.52	10.29

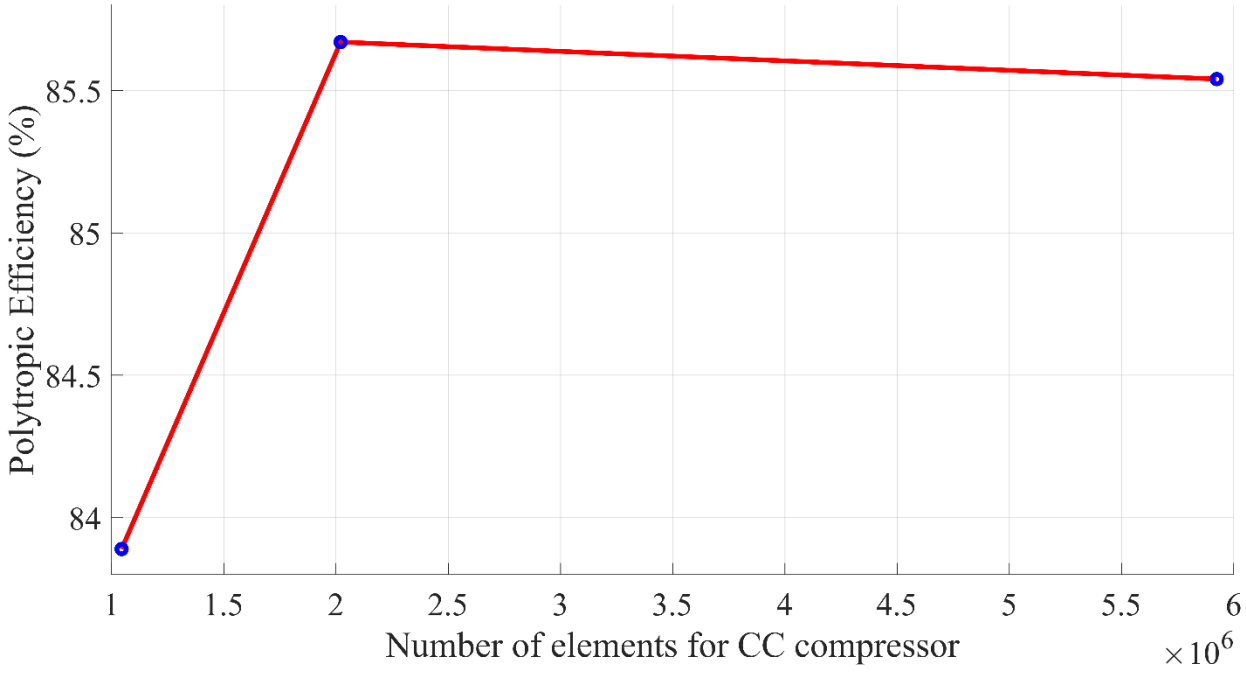

Figure B-2 Polytropic efficiency of fishtail diffuser versus total number of elements

B.3 Vaneless Diffuser

Table B-3 Data for vaneless diffuser mesh study

	Type	0.25x	1x	4x
Impeller Mesh	Structured	719,246	719,246	719,246
Vaneless Diffuser Mesh	Unstructured	129,856	519,422	2,077,688
Total	-	849,102	1,238,668	2,796,934
Mean y+	-	28.64	7.93	3.08
Maximum y+	-	53.42	12.36	10.08

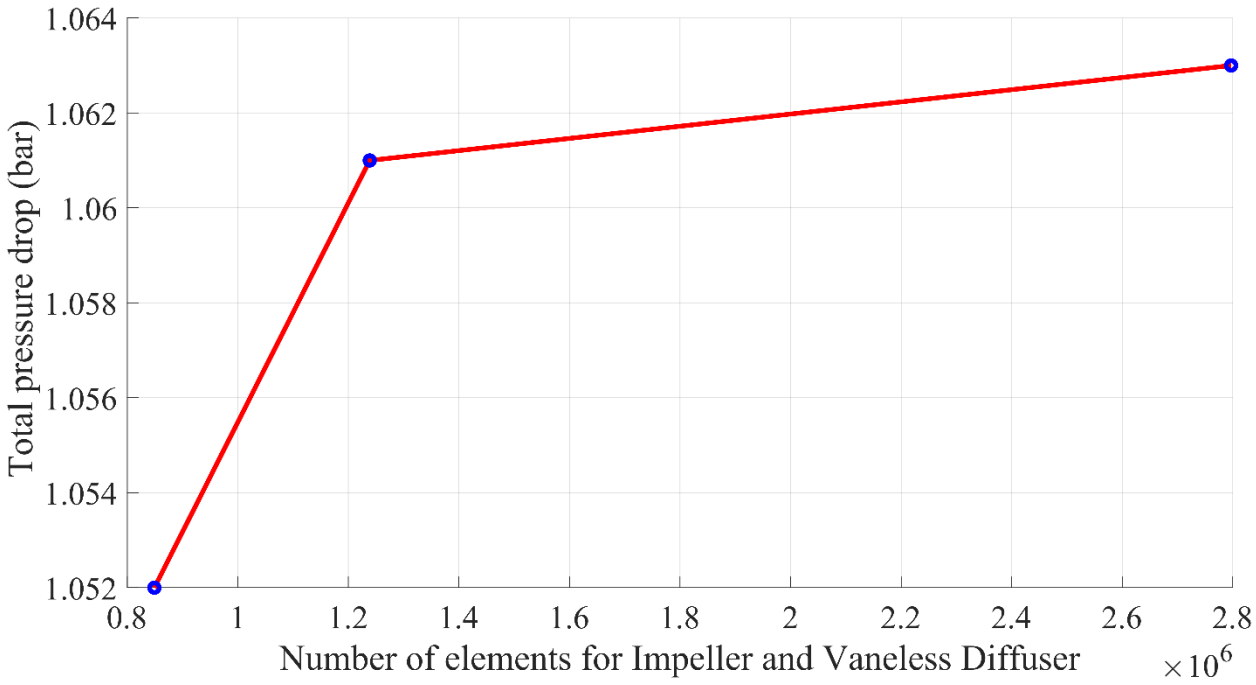

Figure B-3 Total pressure drop across vaneless diffuser versus total number of elements

B.4 Axial Rotor (Original Design)

Table B-4 Data for axial rotor (original design) mesh study

	Type	0.25x	1x	4x
Impeller Mesh	Structured	719,246	719,246	719,246
Vaneless diffuser Mesh	Unstructured	519,422	519,422	519,422
Axial Rotor (Original Design)	Structured	252,182	933,973	3,699,467
Total	-	1,490,850	2,172,641	4,938,135
Mean y+	-	29.64	4.67	1.74
Maximum y+	-	47.32	10.34	3.19

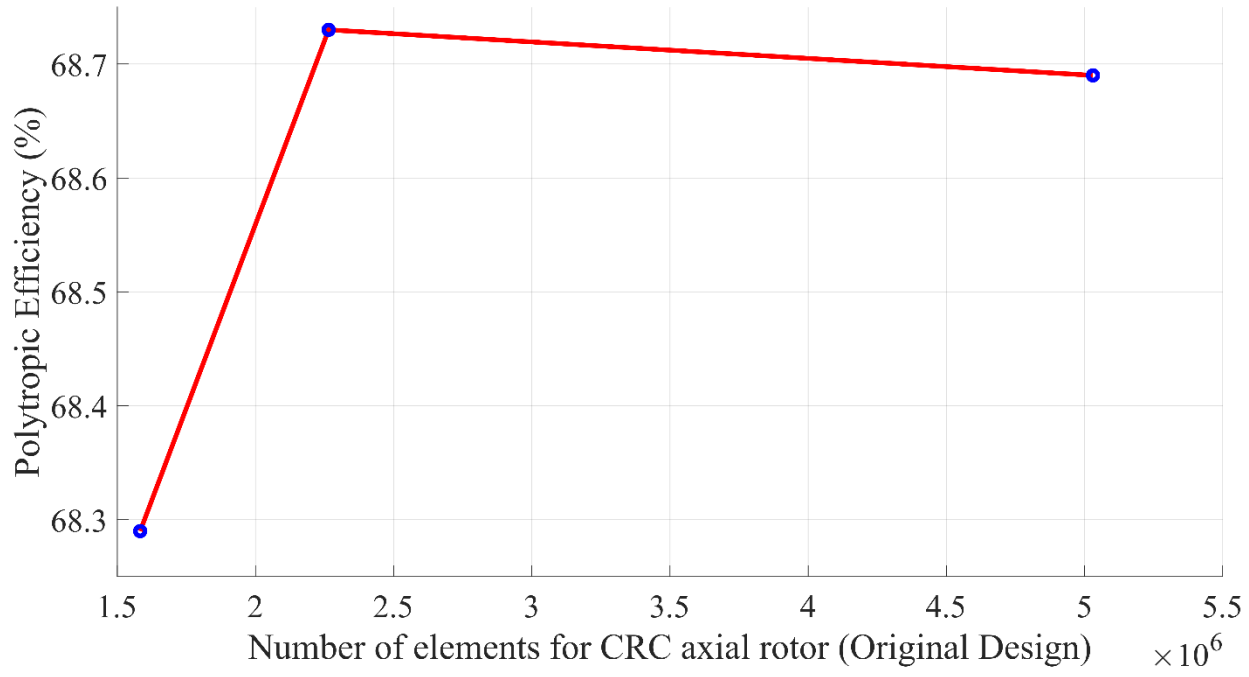

Figure B-4 Polytropic efficiency of axial rotor versus total number of elements

B.5 Vaned Diffuser

The mesh study for the vaned diffuser is carried out with CFD simulation of the impeller (with final impeller mesh) in combination with the vaned diffuser of varying mesh size. The reported parameter is the polytropic efficiency of the impeller-vaned diffuser combination.

Table B-5 Data for vaned diffuser mesh study

	Type	0.25x	1x	4x
Impeller Mesh	Structured	719,246	719,246	719,246
Vaned diffuser Mesh	Structured	177,073	708,292	2,833,168
Total	-	896,319	1,427,538	3,552,414
Mean y+	-	9.21	2.46	1.01
Maximum y+	-	23.94	7.79	3.84

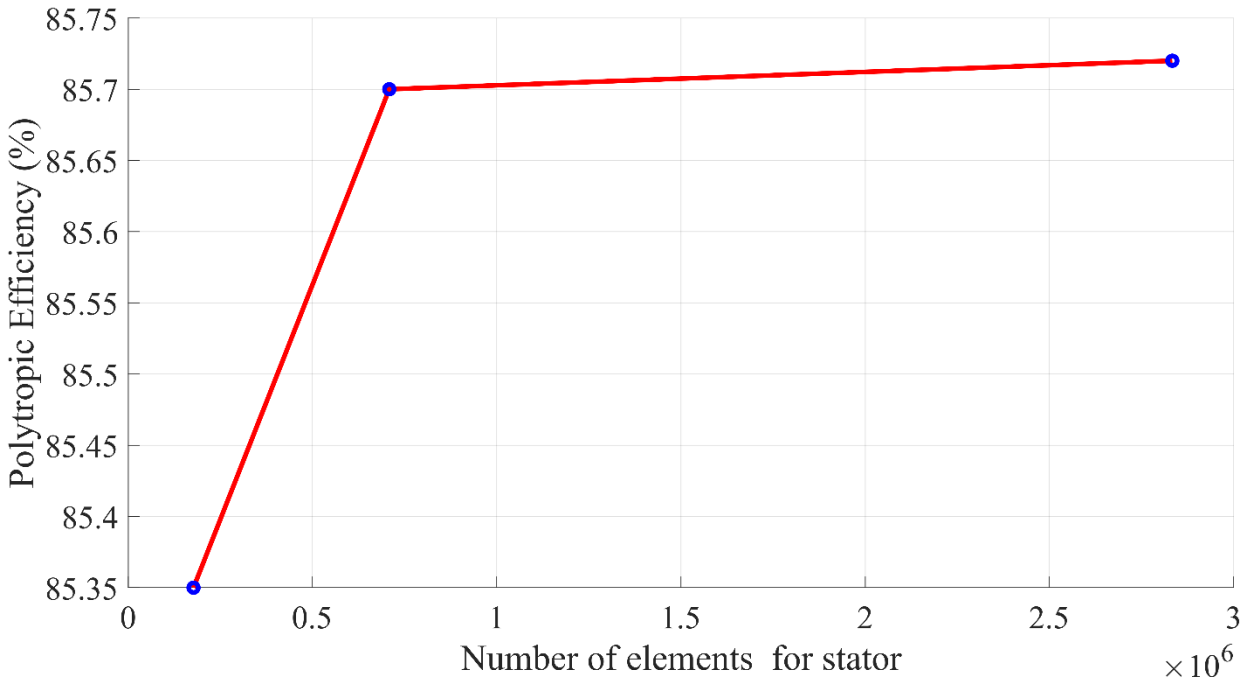

Figure B-5 Polytropic efficiency of impeller-vaned diffuser combination versus total number of elements in diffuser

B.6 Axial Rotor (Final Design)

Table B-6 Data for axial rotor mesh study

	Type	0.25x	1x	4x
Impeller Mesh	Structured	719,246	719,246	719,246
Vaned diffuser Mesh	Structured	708,292	708,292	708,292
Axial Rotor	Structured	248,315	1,026,344	4,058,828
Total	-	1,675,853	2,453,882	5,486,366
Mean y+	-	17.77	3.44	0.49
Maximum y+	-	31.96	8.79	1.84

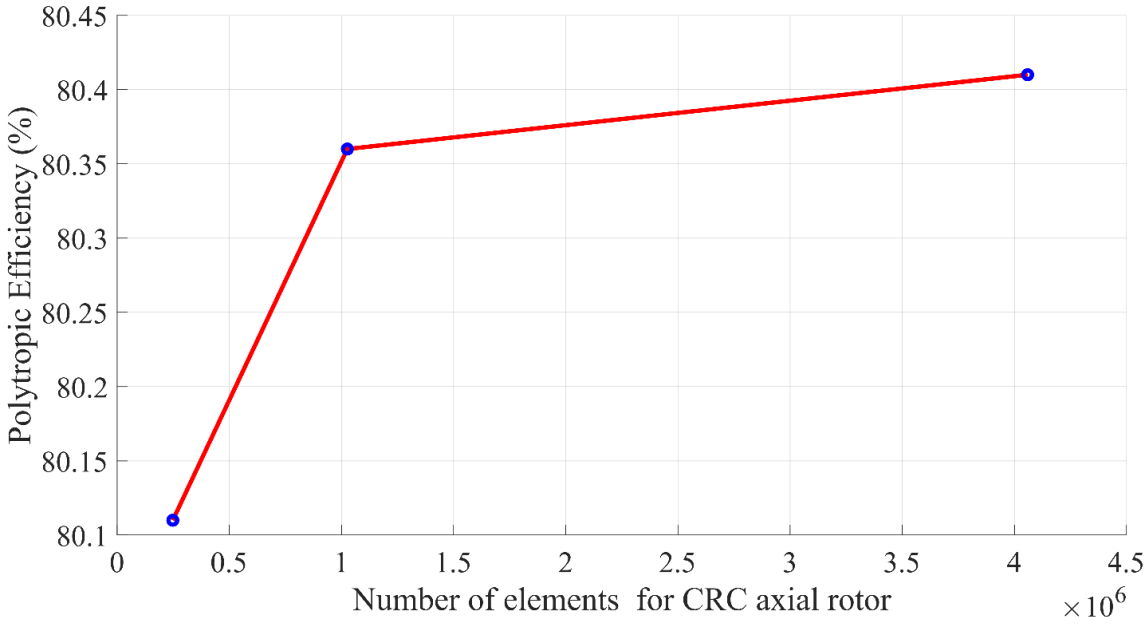

Figure B-6 Polytropic efficiency of CRC compressor versus total number of elements